Supported Silver Catalysts for Ethylene Epoxidation

J.E. van den Reijen

Supported Silver Catalysts for Ethylene Epoxidation

Gedragen zilver katalysatoren voor etheen epoxidatie

(met een samenvatting in het Nederlands)

Proefschrift

ter verkrijging van de graad van doctor aan de Universiteit Utrecht
op gezag van de rector magnificus, prof.dr. H.R.B.M. Kummeling,
ingevolge het besluit van het college voor promoties
in het openbaar te verdedigen op

woensdag 10 juni 2020 des middags te 2.30 uur

door

Jeroen Elias van den Reijen

geboren op 8 november 1987 te Raamsdonk

Promotoren:

Prof. dr. P.E. de Jongh

Prof. dr. ir. K.P. de Jong

Dit proefschrift werd (mede) mogelijk gemaakt met financiële steun van NWO Vici project 16.130.344

It is now safe to turn off your computer.

Windows 95 closing screen

Jeroen van den Reijen
Supported Silver Catalysts for Ethylene Epoxidation
ISBN: 978-94-6375-935-9

Cover designed by Jeroen van den Reijen
Printed by Ridderprint, www.ridderprint.nl

Contents

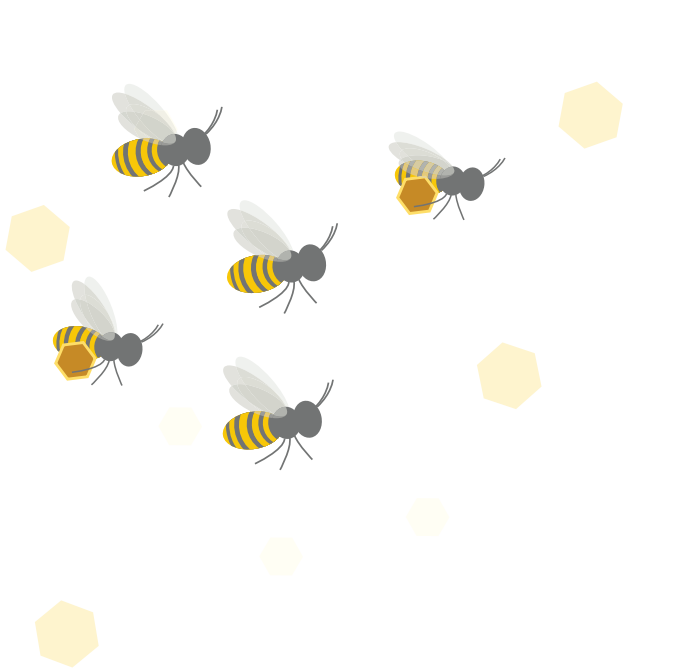

General Introduction

1.1 Supported metal catalysts

Almost all chemical production industries require the use of a catalyst in one or more steps of their processes. Even in the treatment of the waste of these industries, such as cleaning effluent gases, catalysts are required to meet the stringent environmental specifications.[1] With growing concern about emissions and the resulting stricter environmental laws, catalysis will continue to play a crucial role.[2–4] Heterogeneous catalysts are the work horses for most of these industrial processes and transition metals are often the active phase in these catalysts. In order to maximize the amount of available active metal surface, these metals are commonly distributed over support materials, such as metal oxides or carbon.[5,6] These supports facilitate the dispersion of the active phase, provides stability against sintering and provides mechanical strength.[7] The choice of the support material, the active metal *and* the structural requirements, such as support specific surface area and porosity, metal particle size etc., are determined by the chemical reaction the catalyst is applied to.[4]

Supported metal catalysts are commonly prepared by impregnation of the support material with an aqueous solution of a metal salt.[7–10] Porosity in the support material facilitates this as it increases the support surface area and increases the affinity to liquids due to capillary forces.[11,12] The impregnated material is dried to remove the solvent and immobilize the metal salt often preferably with a homogeneous distribution on the support surface. The dry catalyst precursor is heat treated to form the catalyst that can either be transported to the reactor or used directly. The heat treatment can be performed in oxidizing, reducing or inert atmospheres and often consists of a sequence of these, *e.g.* an oxidation in air to decompose the metal salt, followed by a reduction to obtain the active metal. A gentle oxidation is then often performed to form a protective oxide layer on the reduced metal in order to stabilize the catalyst during transportation through air.[7–9]

1.2 Coinage metals

Silver, copper and gold, sometimes called "the coinage metals", are known from prehistoric times. These metals were (and are) rare enough to be valuable, occur in metallic form in nature and are malleable and ductile (see table 1.1) and therefore suitable to be used in the first coins.[13,14] Due to their resistance to oxidation, the weight of coins made from these materials does not significantly change with time, making them the basis for a stable monetary system.[14] This system persisted for ages and even today a large part of the usage of the coinage metals are in coins and jewelry. For silver and copper about 10 % of the annual consumption in the United States is attributed to jewelry, while this is almost 60 % for gold.[15–17]

Another significant application of these metals is as a financial investment, which accounts for another 30 %. This application is a large driver for the high and fluctuating price of gold (€ 35 gram in 2017) compared to silver (€ 0.40 per gram).[18,19] The other reason for the large price differences between these metals is their relative abundance in the earth's crust, with silver at 70 ppb being 70 times more abundant than gold. Copper (50 ppm) is again 700 times more abundant than silver, albeit still much rarer than base metals such as iron (40000 ppm or 4 %) or aluminum (8 %).[20] Due to the relatively high availability copper is the most commonly used coinage metal, as several relevant chemical and physical properties such as conductivity and reduction potential are comparable, as can be seen in table 1.1. With a relatively low price of € 0.005 per gram copper finds a total annual apparent consumption of 2.5 million metric tons in applications such as construction, electronics and transportation, dwarfing the total apparent consumptions of gold

Table 1.1: Selection of metal properties of coinage metals and iron.

	Ionization Energy (eV)[22]			Reduction potential (V)	Conductivity (10^6 S m^{-1})[23]	Density (kg m^{-3})[23]	Melting temperature (°C)[24]	Young Modulus (GPa)[25]
	0	1+	2+					
Iron	7.90	16.20	30.65	-0.44	9.93	7850	1482-1593	210
Copper	7.73	20.29	36.84	+0.52	59.6	8940	1084	117
Silver	7.58	21.48	34.8	+0.80	63.0	10490	961	72
Gold	9.23	20.2	30.0	+1.83	45.2	19320	1063	74

(200 metric tons) and silver (5000 metric tons).[15–17,21]

Silver found a large application in photography, as well as uses in jewelry and electronics.[15] In the '80 and '90s half of the silver consumption has been in photography. In this case silver salts were applied, which when exposed to light, decompose forming a negative image depending on the exposure and intensity of the incoming light.[26] The use of silver in modern photography has decreased strongly due to digital photography and to improvements of photography techniques, greatly reducing the required thickness of the silver salt coating and the application of non-silver components.[26,27]

The light sensitive properties of silver salts are also apparent in medicine. Since the 17th century silver nitrate and 'colloidal silver' have been used in wound care, effectively disinfecting sores and ulcers.[28] A side-effect of this application is the blue-grey discoloration of the skin which is in extreme cases permanent. The use of silver in medicine has decreased significantly since the introduction of antibiotics and the overall improvement of diet and hygiene, but silver containing bandages are still being used in for example burn-wound care.[29,30] This is thought to be safe due to the low silver dosages, preventing the accumulation of silver in the body while still providing the benefits of the antibacterial and antiseptic properties.[31,32] However, the use of silver in medicine is considered controversial, in part because of the mechanism responsible for the beneficial properties of silver is still unknown.[28] More recently silver nanoparticles have been used for odor abatement for example in socks.[33,34]

The combination of scarcity, high value and inertness of these metals makes them unlikely candidates to be applied in catalysis. However, nanosizing of coinage metals makes them more reactive, and therefore susceptible to oxidation.[35–39] This has led to interesting catalytic properties, especially in selective oxidation catalysis.[40] As the noble character of the metal and therefore the degree of oxidation depends on the size of the metal particle, the reactivity can potentially be tuned by varying the particle size.[41,42]

1.3 Silver catalysts

Due to their interesting properties, coinage metals can be found in some catalytic applications, both in academia and industry. The oxidation of CO at low temperature by supported gold catalysts[35,43] and the selective oxidation by copper-exchanged zeolites are well-known academic examples of these.[44–46] Some modern uses of silver catalysis are photocatalysis[47–49], the selective hydrogenation of α,β-unsaturated aldehydes[50,51] and NO_x and ammonia abatement.[3,47,52] However, silver is also applied in two major industrial processes; the oxidative dehydrogenation of methanol to formaldehyde[53,54] and selective oxidation of ethylene.[55,56]

The industrial process of the oxidative dehydrogenation of methanol (Figure 1.1) over silver catalysts is performed at high temperatures (600 – 700 °C) yielding a high or complete conversion with selectivities around 90%.[54,56] Unfortunately, the catalyst only lasts several months to a year before it needs to be replaced.[57] The methanol-rich (36-45 % in air) gas feed in this reaction is converted to an aqueous solution of formaldehyde. Alternatively, this reaction is performed over iron, molybdenum or vanadium oxide catalysts.[54] This metal oxide process is better known as the Formox process, which produces higher formaldehyde yields at lower temperature (340 °C), but has a larger environmental footprint and a higher capital investment.[58] Together, these two processes account for 90 % of all formaldehyde produced worldwide,[54] where the silver based technology is preferred with 70 % of the plants using this technology.[58]

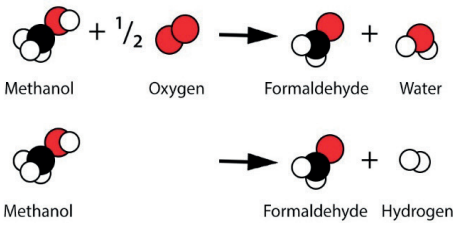

Figure 1.1: Oxidative dehydrogenation (top) and dehydrogenation (bottom) of methanol. Both reactions occur during the catalytic production of formaldehyde.

The largest commercial application of silver in catalysis is found in the production of ethylene oxide by the selective oxidation of ethylene; This is also the main reaction discussed in this thesis. This process has an annual worldwide production of $35 \cdot 10^6$ ton in 2017 with an annual growth of circa 4 %.[55,59,60] The desired product of this reaction is ethylene oxide (EO). Currently, silver is the only metal capable of performing the moderate oxidation of ethylene to the metastable ethylene oxide in a commercially viable way.[55]

The formation of ethylene oxide from ethylene and oxygen (r_1 in Figure 1.2) is exothermic (106.7 kJ mol_{C2H4}^{-1}) and the non-selective side reaction (full combustion, forming carbon dioxide and water, r_2 in Figure 1.2) even more so (1323 kJ mol^{-1}).[55] This poses the danger of a reaction runaway,[61] as EO selectivities decrease with increasing temperature.[62] Also the formation of explosive mixtures and auto-ignition of reactants and products poses safety concerns,[63,64] both around the reactor and downstream facilities.[64] Even at the consumer side, in plants where EO is used as a reactant or for sterilization, EO is considered highly dangerous. It has a maximum exposure limit of 1 ppm for an 8 hour time-weighted average, as it is acutely toxic and carcinogenic.[65,66]

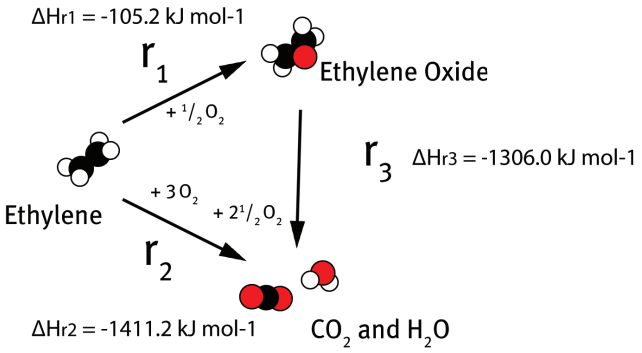

Figure 1.2: Reaction scheme for silver catalyzed selective oxidation of ethylene. r_1 represents the desired reaction pathway, the epoxidation of ethylene. Pathway r_2 represents the direct combustion of ethylene, and r_3 represents the combustion of ethylene oxide as a secondary reaction following r_1. Enthalpies of combustion at standard conditions for ethylene and ethylene oxide obtained from NIST chemistry webbook and enthalpy of partial oxidation of ethylene to ethylene oxide is derived from this data.

Ethylene oxide is a versatile commodity chemical due to its highly strained ring structure. This configuration makes the molecule highly reactive, enabling the formation of a wide range of products.[55,59,67] Ethanolamines, polyglycols and polyols are some of these products, while ethylene oxide itself is extensively used as a disinfectant and sterilizing agent.[55,63,68] However, by far the most important consumption of ethylene oxide is for its hydration to ethylene glycol. Ethylene glycol is the main component in antifreeze and a precursor for polyester and poly ethylene terephthalate (PET).[12] .

When ethylene oxide was first discovered in 1859, it was produced via an indirect chlorinating route. In this reaction a chlorinated intermediate was formed which was purified and separated,[69] and the intermediate was then converted to ethylene oxide using a caustic soda or lime.[67,70] This reaction required a stoichiometric amount of chlorine and produced chlorinated byproducts.[55,67,70] The direct silver catalyzed route was discovered by Lefort in 1931, and is the basis for the current industrial process.[55,71,72] This direct process is preferred over the chlorohydrin process for both economic and environmental reasons.[55,63]

1.4 Ethylene epoxidation

The industrial process based on the direct route discovered by Lefort involves the selective oxidation of ethylene (Figure 1.2). This reaction is catalyzed by α-alumina supported silver particles within a size range of 100 – 1000 nm.[55,72–74] To improve the catalytic performance, several promotors are added to the modern generation of catalysts. These promotors can be alkali metals, rhenium, sulfur, phosphorus and boron compounds.[72]

Chlorine components like vinyl chloride or ethane chloride are continuously added to the reactant feed and decompose on the silver surface. At the same time, the resulting chlorine is removed from the catalyst surface by unoxidized reactants.[67] The stripping and introduction of chlorine are in equilibrium, preventing poisoning of the surface due to chlorine accumulation. Chlorine and promoting compounds are primarily added to increase the selectivity towards ethylene oxide

or to increase the stability of the catalyst.[74–76] The activity of the catalyst is less important as high conversions decrease the ethylene oxide selectivity due to the secondary reaction (r_3 in Figure 1.2, the full oxidation of ethylene oxide).

The presence of chlorine on the surface suppresses the full oxidation of ethylene,[74,77,78] as the presence of chlorine on the catalyst surface prevents the formation of certain surface species responsible for the unselective pathway, leading to an increase in the intrinsic selectivity.[75] The competitive adsorption of chlorine on the silver surface indiscriminately suppresses oxygen adsorption on the silver surface and therefore decreases the overall activity by suppressing both the selective (r_1) and unselective (r_2) pathways.[47,77,79,80] A secondary effect of chlorine promotion leads to a suppression of the secondary, unselective reaction (r_3); the decomposition of ethylene oxide to form carbon dioxide and water.[79,81]

In a typical epoxidation reactor a feed containing oxygen, ethylene and ppm-levels of the chlorine moderator in an inert diluent gas is fed over the reactor at 200 – 280 °C at 15 bar.[55,72] The reactor is designed to have good control over the temperature as to prevent hot-spots.[82] The oxygen content is important to maintain an oxide overlayer on the silver, which is required to obtain high selectivities. However, the oxygen content is kept below 10 % per volume to prevent the formation of explosive mixtures. [55,72,83] When the oxygen content is below this value, the ethylene concentration can be maintained at a relatively high value of 30 – 40 vol% safely.[55,72,83] As selectivity decreases with conversion, the (ethylene) conversion is kept low to maintain a high yield. Commercially, a yield of 1 – 3 vol% EO is viable.[55] Modern industrial catalysts obtain selectivities toward ethylene oxide of 90 %[77,84] compared to about 50-70 % for early epoxidation catalysts.[85,86]

Besides (promoted) silver catalysts, also other catalytic systems are being investigated for this reaction.[87–90] High selectivities towards ethylene oxide are reported by Jankowiak and Barteau for CuAg bimetallic catalysts,[89,91] and later also for AgPd bimetallic catalysts.[87] Due to the bimetallic nature of these catalysts, the environment during reaction can greatly influence composition of the catalyst surface, as for example in the CuAg catalysts segregation of the metals occurs under reaction conditions.[92,93] Depending on the metal ratios and reaction conditions, alloying, but also promotion, additional metals can therefore be either beneficial or unfavorable for the catalytic performance of the silver catalyst.[88,92,93]

As silver is capable of selectively oxidizing ethylene, the simplest olefin, it seems straightforward that this system is also an interesting candidate for the epoxidation of other olefins. However, silver appears to be unable to selectively oxidize higher olefins in gas phase, due to activation of the β- hydrogen (one of the hydrogen atoms bound to the carbon atom situated next to a carbon atom involved in the double bond). [94–96] As ethylene contains only two carbon atoms, both part of the double bond, no β-hydrogen is present in this molecule. In the presence of an oxidation catalyst such as silver, the activation of β-hydrogen leads to full oxidation of the olefin, with ketones, aldehydes and alcohols produced as by-products.[95]

Small gold or silver particles supported on high surface area supports are selective in the epoxidation of for example propylene.[11,94] As these types of catalysts are predominated by different, and more reactive, active sites than the active sites thought to be responsible for the epoxidation of

ethylene,[97–99] this implies a different mechanism for the epoxidation of olefins with β-aliphatic hydrogen than for olefins without β-hydrogen.[94,95]

1.5 Reaction mechanisms and kinetics

A typical catalytic cycle for heterogeneous catalysts consists of three key-steps, starting with the adsorption of the reactants onto the surface (step 1), diffusion and reaction of these reactants on the catalyst surface (step 2) and desorption of the product(s) (step 3).[100] In this last step the active site is regenerated and available for a next catalytic cycle. This is known as a Langmuir-Hinselwood mechanism.[101–103] Alternatively, one of the reactants can adsorb onto the catalyst surface while a second reactant does not adsorb on the surface at all, but reacts with the adsorbed species directly from the gas phase. This Eley-Rideal mechanism is far less common than a Langmuir-Hinselwood mechanism.[102,103]

The silver catalyzed epoxidation of ethylene occurs *via* a third type of mechanism known as the Mars-van Krevelen mechanism.[84,104] In the Mars-van Krevelen mechanism the desorption of the product and the regeneration of an active site are de-coupled.[105,106] In ethylene epoxidation the active phase is a silver oxide surface layer which reacts with ethylene to form ethylene oxide, leaving an oxygen vacancy.[107] This vacancy can be reoxidized by oxygen from the gas phase to close the catalytic cycle. This means that the state of the catalyst is not only determined by the reaction itself, but also the catalyst pretreatment can play an important role on the performance of the catalyst, even after several hours time-on-stream.[79,108] This type of mechanism has the unique property that an oxidized catalyst can oxidize ethylene in absence of gas phase oxidants.[109] These three types of reaction mechanisms act as a way of categorizing the reaction pathways and a method for describing their kinetics, but the true and exact reaction mechanism of a catalytic reaction can be a variation of one of these types or a combination thereof.

Although silver catalyzed ethylene oxidation is a mature and industrially widely applied reaction, no consensus about the exact reaction mechanism exists.[55,84,110,111] This is due to the complicated state of the catalyst surface and uncertainty about the nature of the active site under reaction conditions.[79,97,112,113] Different oxide species coexist and appear to be active in the reaction.[74,84,91,114,115] Already in 1970 Kilty and Sachtler discussed the existence of two different types of oxygen adsorbed on the silver surface of the catalyst; molecularly and atomically adsorbed oxygen, *i.e.* a chemisorbed oxygen molecule or oxygen atom.[116] They proposed an Eley-Rideal type mechanism in which ethylene reacts directly from the gas phase with one of the two different oxygen species, as ethylene did not adsorb on the active surface.[116] A reaction with the a oxygen molecule would then yield ethylene oxide and an oxygen atom: the second type of oxygen species. A reaction of six of these oxygen atoms with an ethylene molecule would yield carbon dioxide and water, as illustrated in Figure 1.3. Due to the orientation of adsorption of oxygen molecule, the most accessible oxygen is slightly more electrophilic and is therefore suggested to be responsible for activating the double bond, while the more nucleophilic oxygen atom was to be responsible for the full oxidation of ethylene.

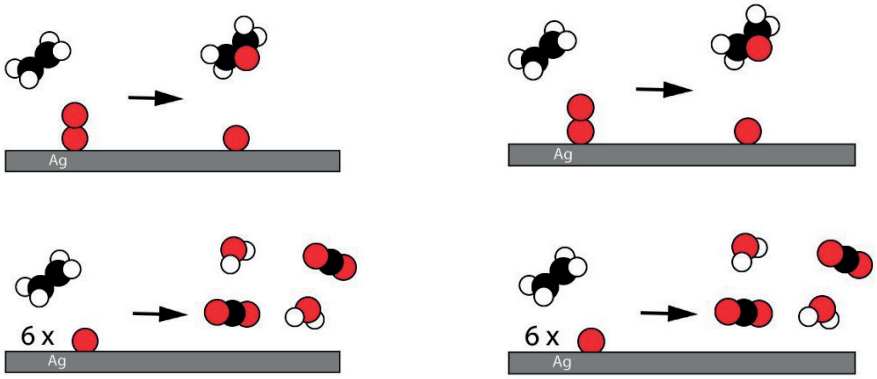

Figure 1.3: Eley-Rideal reaction mechanism proposed by Kilty and Sachtler in which for every six ethylene oxide molecules formed, one ethylene molecule is fully oxidized. This mechanism has been proven inadequate due to experimental selectivities exceeding the theoretical maximum implied in this mechanism.

In the mechanism of Kilty and Sachtler it is assumed that molecular adsorbed oxygen will only produce the epoxide and an atomically adsorbed oxygen. On the other hand, atomically adsorbed oxygen will never lead to ethylene oxide and is responsible for the unselective reaction as six of these atomically adsorbed oxygen species would react with a single ethylene molecule and lead to full combustion.[116,117] Due to these assumptions, the selectivity in this mechanism can not exceed a theoretical selectivity of $^{6}/_{7}$ or 85.7 %. However, as newer promoted catalysts achieved selectivities exceeding this maximum, this mechanism could not be the only mechanism for ethylene epoxidation.[62,116,117]

Grant and Lambert showed that the pretreatment of the catalyst plays a large role in the catalytic performance.[118,119] As ethylene does not, or only weakly, adsorbs on an oxygen free silver surface, the surface needs to be slightly oxidized. A pretreatment of the catalyst is performed to obtain the specific oxidized surface required for an active and selective operation.[63,120,121] The oxygen partial pressure during this treatment greatly influences the amounts of the different oxygen species present on the surface, in turn influencing the activity and selectivity of the catalyst.[118] This led to the discovery that atomically adsorbed oxygen can also catalyze the selective reaction path when subsurface oxygen is present.[119] This subsurface oxygen is crucial for the catalyst activity, and influences largely the selectivity to EO.[114] Grant and Lambert postulated an alternative mechanism for the oxidation of ethylene in which molecular adsorbed oxygen was not the species responsible for the selective reaction pathway, but merely a spectator species. [119] They proposed that atomic oxygen, stabilized by subsurface oxygen, was involved in both the selective and unselective pathways.[119]

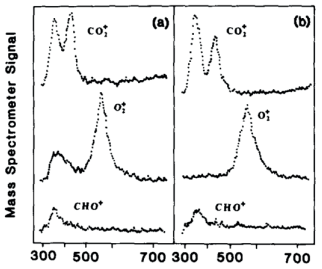

FIG. 2. Multimass TPR spectra for C_2H_4 oxidation on active Ag(111). (a) In the presence of dioxygen. (b) Without dioxygen. Other conditions as for Fig. 1.

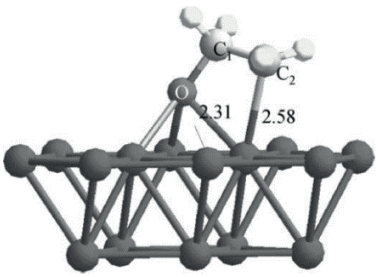

Figure 1.4: TPD of Grant and Lambert, showing both molecular and atomic oxygen species in the middle trace line at 380 and 580 K respectively. In the bottom trace line the desorption of a combination of ethylene oxide and acetaldehyde is shown. The presence of the these species both in the presence and absence of the 380 K $O_{2,ads}$ peak shows that the presence of molecular oxygen was not required for the oxidation of ethylene.[119] *This leads to the designation of molecular oxygen as a spectator species (left). Structure of the surface intermediate upon activated adsorption of ethylene oxide.*[122,123] *This species is described as an oxametallacycle and believed to be the selective intermediate in the OMC mechanism (right).*[92,123–126]

In an alternative mechanism, known as the oxametallacycle (OMC) mechanism, a so called oxametallacycle ethylene adsorbs on a metal-oxygen bridging site, creating a ring structure containing ethylene, an adsorbed oxygen atom and a silver surface atom.[62] In this mechanism, molecular oxygen does not directly take part in the reaction, and oxygen atoms are part of the active site. Only atomic oxygen onto which ethylene adsorbs in a specific conformation acts as the active site of the selective reaction, other conformations are either unreactive or unselective.[111,127] As the ethylene does not adsorbs directly onto the active site, but first diffuses over the catalyst surface, it follows Langmuir-Hinselwood kinetics[81,125] as well as Mars-Van Krevelen as the regeneration of the active site, consisting of an accessible silver atom next to an adsorbed oxygen atom, is not directly part of the catalytic cycle.

The OMC mechanism was initially proposed based on computational results, but OMC species have also been detected on single crystal model catalysts.[124,128,129] Once an OMC surface species is formed, it can desorb as ethylene oxide or acetaldehyde.[129] The latter is known to be formed during this reaction, but is readily fully oxidized under reaction conditions and therefore rarely observed.[55] However, the OMC mechanism cannot explain the increase in selectivity with increasing oxygen coverage which is observed by Akella and Lee in 1984 as it requires the presence of bare silver atoms to form the required surface species.[84,117,130,131]

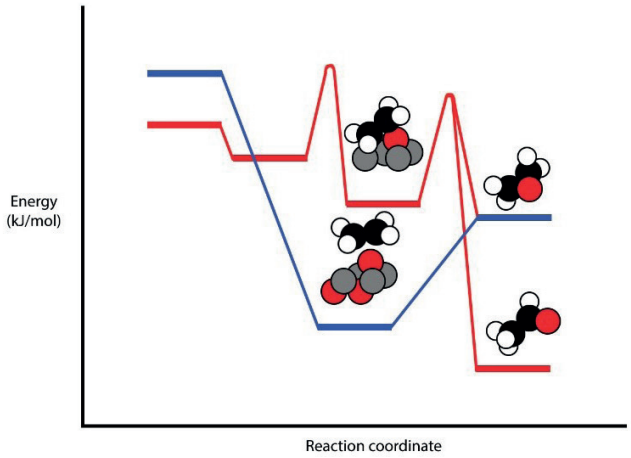

Figure 1.5: Potential energy diagram showing the competitive OMC (red) and Eley-Rideal (blue) reaction mechanisms proposed by the group of van Santen. (adapted from Ozbek et al.)[81] *Note that the Eley-Rideal mechanism only yields ethylene oxide, while the OMC mechanism can yield both ethylene oxide and the undesired acetaldehyde.*[129]

Van Santen *et al.* described an Eley-Rideal type mechanism in competition with the OMC mechanism which can explain the observed oxygen dependency.[84] In this mechanism a 100% selective reaction pathway occurs when gaseous ethylene reacts with an adsorbed oxygen atom on the silver surface. Only when vacancies in the oxygen overlayer are created by the desorbing ethylene oxide, another ethylene molecule can adsorb to form a potentially unselective OMC structure.[129] The competitive adsorption of oxygen and ethylene leads to a dependence of the selectivity on the oxygen partial pressure.[84]

Note that the atomic oxygen in the Eley-Rideal mechanism always leads to ethylene oxide, while in the mechanism proposed by Kilty and Sachtler the same species was stated to always lead to full combustion.[116] While the Eley-Rideal model predicts the performance of the process quite well, no full consensus on the true mechanism of the epoxidation of ethylene has been achieved yet.[84,113,126]

Table 1.2: Summary active and selective species in the proposed mechanisms discussed in this paragraph. Color coded for clarity; however, this is a simplification and does not represent the specific nature attributed to the active sites in the proposed mechanisms.

	Involved in selective reaction pathway	Involved in unselective reaction pathway	Spectator species
Kilty-Sachtler	Molecular oxygen	Atomic oxygen	Not applicable
Grant-Lambert	Atomic oxygen on subsurface oxygen	Atomic oxygen on subsurface oxygen	Molecular oxygen
OMC	Oxometallacycle	Atomic oxygen on subsurface oxygen	Molecular oxygen
Eley-Rideal	Atomic oxygen on subsurface oxygen	Oxometallacycle	Molecular oxygen

1.6 Particle size dependence

A well-defined catalyst and control over the reaction conditions is very important to obtain reproducible results.[73,132] An important parameter that can influence the performance of an epoxidation catalyst is the average silver particle size and size distribution.[132,133] Silver particles of 50 – 70 nm or larger are significantly more active than smaller silver particles.[113,132–135] This particle size effect is attributed to the requirement of specific active sites, which do not occur on small silver particles.[115,133,136]

Particle size dependent reactions are relatively common in catalysis, as van Santen and Che and Bennet have attempted to put these into three categories.[99,137] For the first category, the activity of the catalyst correlates negatively with the particle size, for the second positively, and the last represents catalysts with a structure independent activity, which is of course not a true particle size effect.

In Figure 1.5 the surface-specific reaction rate is shown, in number of molecules converted per moles of metal surface atoms per unit time, also known as the turn-over frequency (TOF). The first category is shown in blue; in this case the relative activity of the active site increases with decreasing particle size pointing to a high activity of atoms with a reduced average coordination number. This category represents reactions for which the rate-limiting reaction step occurs on 'single' surface atoms enhanced by low coordination numbers of these atoms.[137]

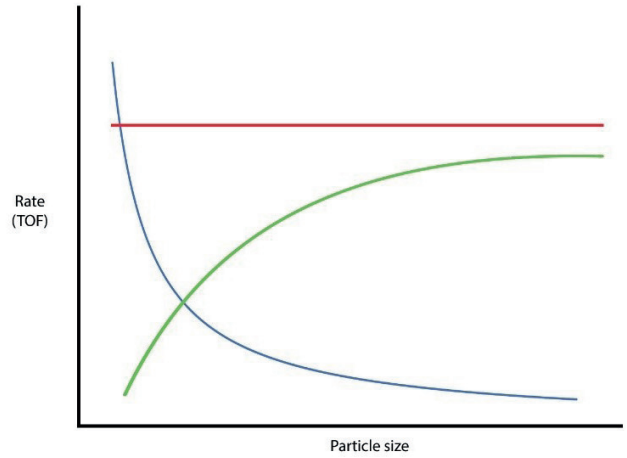

Figure 1.6: Examples of three different categories of particle size effects on the catalyst activity proposed by van Che and Bennet.[99]

The case of a surface-structure independent reaction, shown in red in Figure 1.6, occurs when the rate limiting step is not related to the structure of the active site. In a structure independent reaction, an increase in the activity of individual metal atoms does not lead to an increased activity of the overall reaction due to smaller particles adsorbing reactants and products more strongly.[135,138–141] Such a structure independent reaction is often the reverse reaction of the relation shown in blue, *i.e.* decreasing reaction rate with increasing particle size. An example of a structure independent reaction is the addition of hydrogen to an adsorbed hydrocarbon rather than the desorption of the product.[137,142] Van Santen relates this reversibility to a Bronsted-Evans-Polanski

relationship, in which the activation energy of a reaction is proportional to the difference in enthalpy in the reaction, with the slope being dependent on the position of the transition state along the reaction coordinate. When the forward reaction is highly dependent on the difference in enthalpy, then the transition state highly resembles the product, and consequently that for the reverse reaction the opposite is true. For the reverse reaction the activation energy is therefore almost independent on the difference in enthalpy, *i.e.* independent on the reactivity of the surface species and structure independent. Note that for this to be true the nature of the active site must be the same on both small and large particles.

Often the surface-specific rate increases with particle size, such as is the case for ethylene epoxidation, but also Fischer-Tropsch synthesis over cobalt[139,143] or the oxidation of propylene over supported gold catalysts.[138,144]. The cause for this effect involves an active site consisting of a cluster or ensemble of atoms. On smaller particles, the surface of the particle is highly curved, excluding the occurrence of certain configurations of surface atoms.[99,145–148] On these smaller particles the surface structure is also more distorted compared to larger particles.[149–152] In this case, the real catalyst surface under reaction conditions deviates more from the theoretical description of the surface, such as Wulff constructions.[150,153] If the required active site is such an ensemble, the reaction can only occur on larger particles that can accommodate these active sites.[135,138]

The structure dependencies described by van Santen and Che do not exhaustively describe the causes for the particle size effects observed in catalytic reactions. Alternative causes for particle size dependent catalytic reactions exist. For example, in the Au/TS-1 catalyzed epoxidation of propylene, the active site consists of a gold atom on the perimeter of the metal particle where a reactant adsorbs in contact with the support and the metal. The rate therefore scales with the circumference of the metal particle as opposed to the particle size.[154,155]

In Fischer-Tropsch synthesis much lower TOF for particles smaller than 4 – 6 nm depending on the metal are observed.[36,138,151,156] Above this size, the activity per surface atom remains (nearly) constant.[135,138,139] The resulting TOF therefore increases with particle size up until the critical particle size, after which it remains constant. [6] In the epoxidation of ethylene,[135,157] this critical particle size is about 50 – 70 nm. [135,157,158] The structure induced particle size dependencies typically have an upper limit of circa 10 nm for TOF to increase,[138,139,144] almost an order of magnitude smaller than the critical particle size observed in the epoxidation of ethylene.[113,132,133,135,157]

In the epoxidation of ethylene, the cause of the particle size dependency is probably not a structure dependent effect, but rather an electronic effect. Specifically, the degree of oxidation of the silver surface probably plays a role. The amount of corner and edge atoms responsible for specific ensembles of surface atoms does not change much for metal particle sizes above circa 10 nm, while the degree of oxidation does vary for larger particle sizes,[39,115,133] as small particles are readily fully oxidized and large particles can have oxidic surfaces while the bulk is metallic, or support surface oxides as overlayers on top of an oxide surface.[115] This in turn influences the activity of the catalyst, as the required subsurface oxygen described in paragraph 1.4 of this chapter does not exist with metallic or fully oxidized silver particles.[84,115,159]

1.7 Support effects

The role of the support in a heterogeneous catalyst is to enable the preparation of small metal particles and to limit their mobility and hence the deactivation by sintering.[160] Precious metal nanoparticles are distributed over high specific surface area supports to optimize the amount of active surface area available for catalysis.[161] Common support materials in heterogeneous catalysis are alumina, silica and carbon, as these materials are relatively inert and high surface area variants are available.[162] Amorphous silica is a favorite support for academic research due to its versatility;[163] crystalline silica or quartz is less used. For alumina mostly the γ-phase is used due to the high specific surface area of this polymorph.[162]

Table 1.3: Typical characteristics of a selection of silica and alumina support materials

		Specific surface area (m^2 g^{-1})	Density of surface hydroxyl species (OH nm^{-2})	Pore size range
Silica				
	Mesoporous	300 - 1000	2-3	micro- and mesoporous
	Fumed	50 - 500	~3[164]	micro- and mesoporous
	Quartz	0 - 5	< 2	non-porous
Alumina				
	γ-alumina	~200	5 - 15[165–169]	micro- and mesoporous
	α-alumina	0 - 10	1[170,171]	Non-porous

Sometimes the support does influence the catalyst activity, either by showing non-negligible catalytic activity itself,[172] by the formation of metal silicates with the active phase, or by strong metal support interaction.[157,173–176]

In the epoxidation of ethylene, the reactivity of the product EO is a problem. This molecule reacts with surface hydroxyl species of the support, making the support a co-catalyst in the secondary reaction (see Figure 1.2, reaction r_3).[130,177] The isomerization of ethylene oxide on the catalyst support leads to a decrease of selectivity with increasing support specific surface area. Likewise, the selectivity decreases with the ethylene oxide partial pressure, as ethylene oxide is the reactant in the secondary reaction.[55,62,85,132,177] The acetaldehyde formed over the support surface due to this secondary reaction is rarely observed under reaction conditions as it is rapidly oxidized over the silver surface.[73,87,91,95] Industrial ethylene epoxidation catalysts are supported on low surface area supports with a low density of surface species, such as α-alumina.[72,78,178–180] A major downside of these types of supports it that they can only accommodate a limited amount of silver on their surface and are difficult to shape.[8]

Early ethylene epoxidation catalysts were supported on quartz, but this was abandoned when high purity α-alumina became available.[181] α-alumina is the most stable polymorph of alumina with a dense structure[178] and a specific surface area below 10 m^2 g^{-1},[182,183] This material has a low density of surface groups, typically < 1 OH nm^{-2}.[183] Both the hydroxyl density and the low surface area of the support limit the total amount of surface groups.[184–186] The combination of these two characteristics minimizes the amount of available surface hydroxyl groups, preventing the occurrence of the secondary reaction, and hence maintaining a high selectivity towards ethylene oxide.[184–186]

1.8 Scope of this thesis

This work is part of an NWO-VICI project on the performance of supported copper, silver and gold catalysts, with a specific interest in their stability. The primary focus of this work is to investigate the preparation and catalytic performance of supported silver catalysts. The epoxidation of ethylene is studied, as this is the largest industrial reaction based on silver catalysts. Separating the contributions of different parameters influencing the catalytic performance is essential and it is therefore crucial to obtain a high level of control on relevant parameters during catalyst synthesis. For the same reason, the experiments in this thesis are done in the absence of promotors and/or moderators (such as chlorine). This may cause our results to differ from the observed effects in the presence of such compounds, but enables us to better separate the different contibutions of the investigated paramaters on catalyst performance. Primarily α-alumina supported catalysts are used, as these are industrially the most relevant. However, also silica supports are used to investigate the effect of the support on the catalytic performance.

Chapter 2 describes the synthesis of α-alumina supported silver catalysts with different particle sizes. By varying the heat treatment, the average silver particle size is tuned, while maintaining silver weight loading, support and silver precursor. This enables a direct comparison of catalysts with different average silver particle sizes. We investigate the particle size dependence of activity and selectivity for the selective oxidation of ethylene. This method for catalyst preparation is the basis to obtain sample sets in which only one of three key parameters is varied, being average silver particle size (Chapter 2), weight loading (Chapter 4) or support specific surface area (Chapter 5).

In **Chapter 3**, the synthesis of a high surface area, three dimensionally ordered macroporous α-alumina is described. A poly(methyl(methacrylate) colloidal crystal is used as a hard template to introduce porosity of the desired nature. The template material is impregnated multiple times to achieve a high degree of pore filling, resulting in increased yields of α-alumina and a better maintained morphology compared to reference materials obtained after treatment in air at high temperature (1150°C). When an additional heat treatment in inert atmosphere is applied before the heat treatment in air, a carbon film forms in order to stabilize the pore structure during this first heat treatment. The carbon film is removed in the following heat treatment in air.

In **Chapter 4** the thermal stability of α-alumina supported silver catalysts is discussed as this is a valuable tool to assess the deactivation rate for different catalysts. Firstly, particle growth of supported silver particles in oxidative and reductive atmospheres is discussed. Secondly, the effects of the initial average silver particle size, the surface characteristics of the different α-alumina support materials and the silver surface density on the rate of sintering of the active silver particles are compared. Thirdly, the effect of the morphology on stabilizing the silver against sintering is evaluated for large silver particles supported on an ordered macroporous α-alumina support with pore windows smaller than the particles. Lastly, the effect of a constant silver loading and particle size supported on α-alumina supports with different specific surface areas and morphologies is assessed. By assessing these parameters separately, the effects of the interparticle distances, surface characteristics, surface area and particle size on the thermal stability was deconvoluted for silver particles on different support materials.

Chapter 5 discusses the effect of the chemical nature and surface area of the support on the selectivity towards ethylene oxide. A macrokinetic model is constructed to describe the observed decrease in selectivity with increasing ethylene conversions over different catalysts. The effect of the ethylene oxide partial pressure and the amount of support hydroxyl species on the ethylene oxide selectivity are discussed in detail. The trends are then explained via the rate of secondary oxidation of ethylene oxide co-catalyzed by the hydroxyl species. Lastly, a catalyst supported on a high surface area, hydrophobic fumed silica support is tested in the epoxidation reaction and compared to a hydrophilic counterpart to validate our conclusions.

Chapter 6 gives a summary of the work described in this thesis, together with future perspectives.

Preparation and particle size effects of Ag/α-Al_2O_3 catalysts for ethylene epoxidation

This chapter is based on: Journal of Catalysis, 356 , pp. 65-74, 2017

2

Abstract

Currently, for the industrial ethylene epoxidation α-alumina supported silver catalysts are the only catalyst of choice. We demonstrate a novel method to produce these catalysts with different silver particle sizes, but without changing other key parameters that may affect the catalytic performance such as support specific surface area or metal precursor. α-Alumina was impregnated with a silver oxalate solution, and was subsequently dried and treated in different gas atmospheres and at different temperatures to tune the silver particle sizes in the range of 20–500 nm. Particles of 20 nm exhibited a lower turnover frequency than particles of 70 nm and larger, which exhibit a constant turnover frequency, in accordance with results in literature. However, the selectivity, when measured at constant conversion, was particle size independent. This is the first time that the effect of the particle size on the selectivity of ethylene epoxidation is reported at constant conversion. This was made possible by a new method of producing supported silver catalysts, which we expect that is also applicable for silver catalysts with other supports and for the preparation of other supported metal catalysts.

2.1 Introduction

In a profitable operation of a catalytic reaction minimizing material costs and loses is key. In supported metal catalysts the material costs are reduced by dispersing the relatively expensive metal over a support material. Small particle sizes can then be obtained and the amount of active surface per gram, or specific metal surface area can be maximized. However, due to particle size dependencies in catalysis, maximizing the specific metal surface area of a catalyst may not maximize the activity.[187] Similarly, the selectivity towards the desired product plays a large role in minimizing costs. Preventing side reactions reduces the loss of the reactant and when secondary reactions exist maximizing activity may be detrimental for the overall yield of the desired product.[188]

When the activity of a catalyst does not linearly depend on the metal specific surface area, this is can be referred to as a particle size dependent reaction.[187] Particle size effects are common in catalysis and well-known examples of reported particle size effects are the silver catalyzed epoxidation of ethylene, the gold catalyzed epoxidation of propylene and the Fischer-Tropsch reaction.[135,139,144,145] The cobalt catalyzed Fischer-Tropsch synthesis exhibit optimal particle sizes of 6-8 nm.[138,139] In this reactions, metal particles smaller than this optimal size exhibit significantly lower turnover frequencies (TOF) than larger particles, while larger metal particles exhibit particle size independent TOF's.[139] The CO activation requires an ensemble of surface atoms, which are unique to step-edge sites (B5-type sites), which in turn are rare on particles smaller than 10 nm.[141,146] In propylene epoxidation small particles (<2 nm) are highly active, but unselective, while large particles (>4 nm) are hardly active, leading to an optimal particle size of 2-4 nm.[144] The particle size effect in ethylene epoxidation follows a trend similar to the Fischer-Tropsch reaction, but it occurs at particle sizes an order of magnitude larger.[135,157]

Already in 1975 Wu and Harriot reported a decreasing surface-specific rate of both epoxidation and combustion with increasing particle size in the range of 3 – 50 nm.[189] In 1980, Verykios *et al.* observed a minimal specific rate of oxidation (mol m^{-2} s^{-1}) at a particle size of 50 – 70 nm. Both groups reported an increasing selectivity with particle size over the entire size range.[112] At the time, these results were controversial and their conclusions were disputed by Sajkowski and Boudart who claimed that the observed differences in specific reactions rates were too small to be significant and results to be influenced by contaminations. They expected the presence of contaminations to act as a poison due to unexpectedly low turnover rates reported by Verykios *et al.*[147]

Verykios *et al.* synthesized catalysts with small silver particles supported on materials with different specific surface area. They heat treated these catalysts at different temperatures for different calcination times to obtain sets of catalysts with different particle sizes. In a later paper from the same group, they synthesized catalysts with different weight loadings on a single support batch to obtain silver particles with different particle sizes. Using this method, they prevented contaminations that may be introduced by using different support materials and segregation of contaminations during the heat treatment.[132,135] In this second study, they obtained a maximum specific rate of epoxidation and combustion at silver particle sizes of about 40 – 50 nm, contradicting their earlier results.[132]

In this second paper, the selectivity to ethylene oxide increased slightly with particle size, which they attributed to differences in the rates of the secondary reactions for different particle sizes.

This influence of particle size and crystal facets on the selectivity of the reaction is still a subject of debate. Recently Christopher *et al.* argued, based on studies on spheres containing both Ag(100) and Ag(111) facets, and cubes and rods containing primarily Ag(100) facets, that Ag(100) surfaces preferentially lead to EO and Ag(111) surfaces lead to the formation of acetaldehyde.[113,189] In contrast, Campbell reported similar epoxidation rates on both crystal planes in 1985,[190] after initially supporting the claim of Christoper.[191]

However, a complication is that particle size effects on activity and selectivity are often obscured by measuring the selectivity at different conversions. Conversion levels (which depend on activity) have a large influence on the selectivity (as we will demonstrate later in this chapter) and hence a careful deconvolution of the two different factors parameters is necessary. Since the activity showed particle size dependence, the partial pressure of ethylene oxide differs per sample. When corrected for these secondary reactions, for example with a rate of EO oxidation obtained from experiments over bare supports, the true particle size dependency of the selectivity can be estimated, as was done by Lee *et al.*[132] They observed a decreasing selectivity toward ethylene oxide with particle size and believed that the actual particle size dependency to lie somewhere between the observed and the corrected trend.[132]

Since the late 90's, the particle size dependency of the activity has been largely accepted to exhibit a maximum activity per gram of silver at particle sizes of 50 - 70 nm for supported silver catalysts.[132,133,157] However, the cause of this effect was still under discussion. In 1997 the group of Bal'zhinimaev attributed the typical particle size dependence to different electronic states of the silver surfaces. With XPS they showed the formation of an anionic oxygen species on larger particles, while these species were not present on silver particles smaller than 50 nm.[115,136] These results showed a clear correlation with ^{109}Ag-NMR results and catalytic data for the epoxidation reaction over these catalysts[192] and correlates well with the observation of Akella and Lee in 1984 that correlates oxygen coverage with selectivity.[130]

On silver surfaces nucleophilic oxygen is believed to coexist with electrophilic oxygen species, and both are required for an active and selective epoxidation catalyst.[115,119,133,193] The former is required for ethylene adsorption, while the latter activates the ethylene double bond and is inserted to form EO.[194,133] These species were identified as subsurface oxygen and adsorbed oxygen species on silver oxide surfaces.[110,159] This observation fits the alternative reaction pathway proposed by Grant and Lambert in 1985.[119] In 2011 Özbek *et al.* proposed that in the absence of oxygen vacancies the reaction occurs via a selective, direct reaction (Eley–Rideal) pathway, while the reaction occurs via an OMC pathway when oxygen vacancies are present. This reaction explains the competitive formation of acetaldehyde and EO based on the oxygen species present.[195]

Not many studies address the effects of particle size on selectivity and most available literature report an increase in selectivity with particle size.[133,135,157] However, in the academic literature the selectivity is generally reported at a constant temperature and hence at widely varying conversions. To our knowledge, only the paper of Lee *et al.* tried to correct for the inevitable artifacts introduced by this way of reporting.[196] Their method to correct for the secondary reactions, by subtracting an ethylene oxide oxidation rate obtained over bare supports, illustrates clearly how difficult it is to extract the intrinsic particle size dependency of the catalytic performance for this type of catalysts.

As was shown by the work of Verykios *et al.* discussed earlier, intrinsic particle size effects are often obscured by the fact that other parameters change as well.[74,132,135,196] Reported methods for obtaining different particle sizes involve changing the metal precursor, the support material and/or the weight loading.[132,135,138,196,197] Therefore, studying the performance of a set of catalysts having different particle sizes, but obtained from the same precursor on the same support and maintaining a constant metal loading, is highly desired. In this chapter we describe a synthesis method for α-alumina supported silver catalysts with different particle sizes. Building on previous knowledge,[156,198,199] we use different gas atmospheres and temperatures during heat treatment of the catalyst precursor to tune the particle size, while the support type, support surface area and metal loading are kept constant. Precursor decomposition in hydrogen atmosphere yielded significantly smaller particles than heating in air or nitrogen atmosphere. Different gas atmospheres combined with heat treatments at different temperatures and times, yielded a range of different particle sizes. The obtained catalysts were tested in the ethylene epoxidation reaction to investigate the intrinsic effects of the particle size on activity and selectivity.

2.2 Methods

2.2.1 Silver precursor

Silver oxalate was used as the silver precursor for the impregnation of the alumina support. To synthesize the silver oxalate, 2.00 g silver nitrate (≥99.0%, Sigma Aldrich) was dissolved in 20 mL milliQ water and added to oxalic acid solution at 60 °C. The latter solution was obtained by dissolving 1.48 g oxalic acid dihydrate (99%, Sigma Aldrich) (2:1 molar ratio) in 40 mL milliQ water at 60 °C.[200–202] Silver oxalate started to precipitate immediately, and was obtained after centrifugation and three times washing with milliQ water and once with ethanol. The white powder was dried overnight at 60 °C under static air.

2.2.2 Catalyst preparation

Extrudates of α-alumina (surface area 8 $m^2\ g^{-1}$; pore volume 0.4 mL g^{-1}, AL4196E, BASF) were crushed to roughly 400 μm grain size (500 ± 150 μm). 5.0 g of α-alumina support grains was dried overnight at 120 °C in static air before impregnation. The dry powder was impregnated with 1.24 g dry silver oxalate dissolved in 2.0 mL of 0.73 g/g milliQ ethylene diamine(en)/water (1:4:16 mol ratio $Ag_2C_2O_4$: en : H_2O) mixture and subsequently dried in static air at 60 °C.[77,78,158] To favor a homogeneous distribution of silver over the support, the powder was mixed during drying.[203] After drying for 5, 10 and 30 min the powder was mixed manually before leaving the powder overnight to dry.

The impregnated alumina ($[Ag(en)_2]_2C_2O_4/\alpha\text{-}Al_2O_3$) was heated using different conditions, typically 150 mg in a U-shaped flow reactor at atmospheric pressure. After thermal treatment the catalysts were again crushed, and sieved to a 38-90 μm sieve fraction. The resulting catalysts consisted of 15 wt% silver on α-alumina and are denominated as $AgAl_2O_3$_atm_flow. The gas atmosphere during the temperature treatment is represented in atm, given in volume percentages in nitrogen and the flow in mL min-1. The heating rate, final temperature and dwell time during calcination are 5 °C min-1, 215 in °C and 2 hours except for the catalyst denoted as $AgAl_2O_3$_350_100%N2_0, which was heated to 350 °C with 1 °C min-1, and kept at this temperature for 24 hours. An overview of all catalysts discussed in this chapter is listed in Table 2.1.

Table 2.1: Overview of the Ag/a-Al_2O_3 catalyst samples were labeled as $AgAl_2O_3$_ atm_flow

Reducing atmosphere	Inert atmosphere	Oxidizing atmosphere
$AgAl_2O_3$_100%H2_0	$AgAl_2O_3$_100%N2_0	$AgAl_2O_3$_100%O2_0
$AgAl_2O_3$_100%H2_10	$AgAl_2O_3$_100%N2_10	$AgAl_2O_3$_100%O2_10
$AgAl_2O_3$_100%H2_25	$AgAl_2O_3$_100%N2_25	$AgAl_2O_3$_100%O2_25
$AgAl_2O_3$_100%H2_50	$AgAl_2O_3$_100%N2_50	$AgAl_2O_3$_100%O2_50
$AgAl_2O_3$_100%H2_100	$AgAl_2O_3$_100%N2_100	$AgAl_2O_3$_100%O2_100
$AgAl_2O_3$_50%H2_0	-	$AgAl_2O_3$_50%O2_0
$AgAl_2O_3$_50%H2_10	-	$AgAl_2O_3$_50%O2_10
$AgAl_2O_3$_50%H2_50	-	$AgAl_2O_3$_50%O2_50
$AgAl_2O_3$_50%H2_100	-	$AgAl_2O_3$_50%O2_100
$AgAl_2O_3$_20%H2_50	-	$AgAl_2O_3$_20%O2_50
$AgAl_2O_3$_8.5%H2_0	-	$AgAl_2O_3$_8.5%O2__0
$AgAl_2O_3$_8.5%H2_10	-	$AgAl_2O_3$_8.5%O2_10
$AgAl_2O_3$_8.5%H2_25	-	$AgAl_2O_3$_8.5%O2_25
$AgAl_2O_3$_8.5%H2_50	-	$AgAl_2O_3$_8.5%O2_50
$AgAl_2O_3$_8.5%H2_100	-	$AgAl_2O_3$_8.5%O2_100
-	$AgAl_2O_3$_350_100%N2_0*	-

**Heated with 1 °C min^{-1} to 350 °C, and kept at this temperature for 24 hours is static nitrogen*

2.2.3 Characterization

The crystalline phases were analyzed with X-Ray Diffraction (XRD) using a Bruker D8 Advance diffractometer equipped with a Co Kα source (λ = 0.1789 nm) in the angle range from 20° to 90° in 2θ and a characterization procedure in the DIFFRAC Eva software (Bruker AXS). This analysis primarily served to verify the formation of silver oxalate and silver metal respectively.

Elemental analysis was performed with induced coupled plasma-optical emission spectrometry (ICP-OES) and X-ray fluorescence (XRF), using a ThermoFischer Scientific ICP-OES and a Thermo ARL 9400 sequential XRF at Department of Earth Sciences (Utrecht University) respectively. The weight loss during heat treatment was measured using thermal gravimetric analysis (TGA) performed in a Perkin Elmer Pyris 1 TGA under a 10 mL min^{-1} flow of oxygen or hydrogen in 45 mL min^{-1} argon or a flow of 55 mL min^{-1} pure argon. For these experiments the temperature was increased from 50 °C to 250 °C with a heating ramp of 1 °C min^{-1}. The decomposition products were analyzed using a Pfeiffer Vacuum OmniStar mass spectrometer.

The size and spatial distribution of the obtained silver particles were measured using transmission electron microscopy (TEM) and scanning electron microscopy (SEM). The images were obtained using a FEI Tecnai-12 transmission electron microscope and a FEI XL30 SFEG scanning electron microscope respectively. The obtained images were processed using iTEM Soft Imaging System software.[204] UV/VIS spectra of the supported silver catalysts were obtained using a Varian CARY 500 Scan UV-Vis-NIR spectrophotometer with an integrating sphere detector. In a typical analysis, 30 mg of 15wt% Ag/α-Al_2O_3 catalyst was diluted with 600 mg pristine α-Al_2O_3 (1 m^2 g^{-1},

-100 mesh, Sigma Aldrich) and ground to a fine powder before taking a spectrum in the 200-750 nm range. A background measurement of pristine α-Al_2O_3 was performed and subtracted from the obtained spectra. A simplified model of the catalyst was simulated using FDTD Solutions 8.0 software package (Lumerical) to compute UV/Vis spectra. Simulations consisted of a single silver particle in an environment of 0, 10, 20, 25, 33.33, 50, 75 and 100% of α-alumina in air at 300 K. The silver particle size was varied between 10 and 140 nm with steps of 10 nm. A three-dimensional non-uniform mesh with a grid size of 0.5 nm was used for the silver particle and its direct surroundings. The localized surface plasmon resonance was calculated in the 200 – 800 nm range from a total field scattered field source. The simulation was run until converged below 1e-05. The data was fitted with a second order polynomial surface (R^2 = 0.9995). The model was in good agreement with the work from Mock *et al.* for spherical silver particles.[205]

2.2.4 Catalytic testing

Catalytic tests were performed with metal particle sizes ranging from 20 to 500 nm obtained. As a reference a Cs-promoted commercial catalyst containing 18 wt% Ag on α-Al_2O_3[206], was measured under the same reaction conditions. Typically, 150 mg of a 38-90 μm sieve fraction of the material was loaded between two layers of quartz wool in a quartz reactor with a 4 mm internal diameter. The sample was heated to 180 °C in a flow of 15 mL min^{-1} of 8.5% oxygen and 30% ethylene in helium, corresponding to a gas hourly space velocity of 6000 mL g_{cat}^{-1} h^{-1}. After one hour the temperature was increased stepwise to 270 °C followed by 1 hour at 190 and 180 °C respectively (1 hour at 180°C, 1 hour at 190°C, 1 hour at 200 °C, 1 hour at 215°C, 1 hour at 230, 2 hours at 250 °C, 3 hours at 260 °C, 3 hours at 270 °C, 1 hour at 190 °C and 1 hour at 180°C).[77] . The outlet gases of the reaction were analyzed every 30 min by an online Compact GC (Interscience) equipped with a Porabond Q column and a Molsieve 5A column in two separate channels, both with a thermal conductivity detector (TCD) Conversion data were calculated from data retrieved at 190 and 200 °C after steady state was reached. Selectivity data were obtained at an ethylene conversion of 2.8%.

2.3 Results and Discussion

2.3.1 Particle size analysis

Typical images of Ag/α-Al_2O_3 catalysts, obtained using electron microscopy, are shown in Figure 2.1. The micrographs show the samples treated in 50 mL min^{-1} flow of 100% H_2, 100% N_2 and 100% O_2 respectively. In the bright-field TEM micrograph of the hydrogen treated sample in the left frame, the alumina support can be seen in dark grey spots and has a particle size of several hundreds of nanometers. Silver particles are visible as smaller and darker spots, with sizes up to 100 nm. Examples are indicated with circles. In the SEM micrographs of samples obtained after treatment in nitrogen and oxygen displayed in the frames in the middle and on the right, the alumina support surface is visible as light grey rounded particles. The silver particles are bright white spots, isotropic in shape, and not strongly facetted. The silver particle size distributions, shown in the lower frames, are significantly different for different heat treatment conditions. Note the presence of particles larger than 150 nm in the sample treated in oxygen containing atmosphere. The particle size distributions in Figure 2.1 are typical for this type of catalysts.[207]

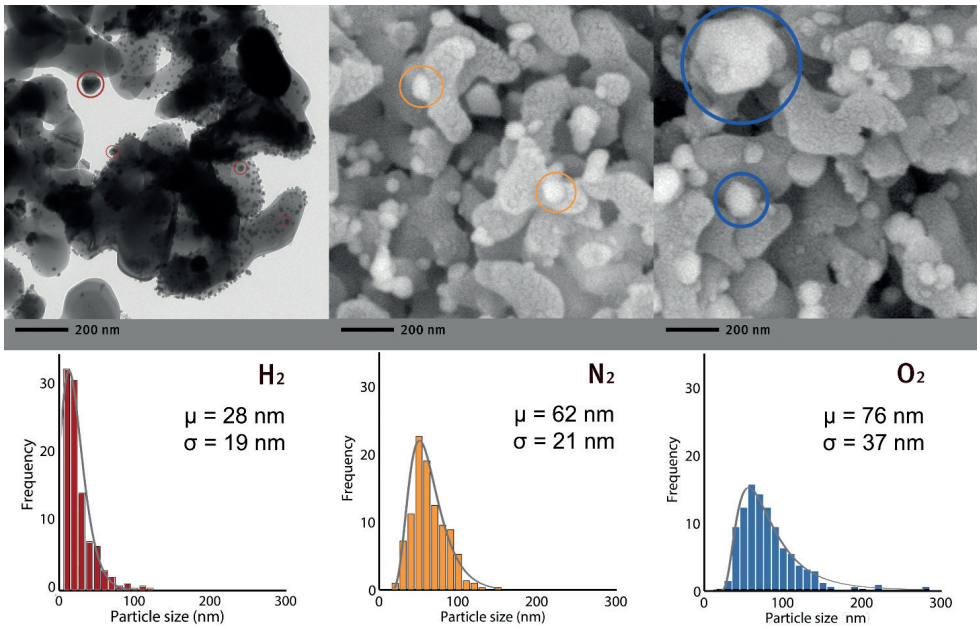

Figure 2.1: TEM and SEM images of Ag/α-alumina with a range of particle sizes. From left to right: $AgAl_2O_3$_100%H2_50 *(TEM),* $AgAl_2O_3$_100%N2_50 *(SEM) and* $AgAl_2O_3$_100%O2_50 *(SEM).*

As it is challenging to obtain results on a statistically relevant amount of sample using electron microscopy, we explored UV/Vis spectroscopy as a bulk analysis technique for validation. In Figure 2.2 the UV/Vis spectra of selected catalysts can be found, with the peak maxima of the SPR peak in the obtained UV/Vis spectra indicated with a black dot. The spectra exhibit a broad peak in the 300 – 750 nm range corresponding to the surface plasmon resonance (SPR) of the silver particles on the catalyst surface. The position of the peak depends on the silver particle size and shape and on the dielectric constant of the direct surroundings of the silver particles. When the particles are assumed to be spherical, a SPR peak with a maximum in the 380 – 500 nm range is expected, shifting to longer wavelengths for larger particles.[127,205] Average silver particle sizes above about 100 nm correspond to grey samples.

The peak maximum shifts to longer wavelengths when going from samples obtained from heat treatment in reducing gas atmospheres to samples obtained in oxidizing gas atmospheres. The intensity of the SPR peak decreases with increasing particle size and the peak position becomes more difficult to determine.[47,48] This is in accordance with computational predictions of the UV/Vis spectra of spherical silver particles of different sizes on a alumina support performed by us and with literature.[208,209]

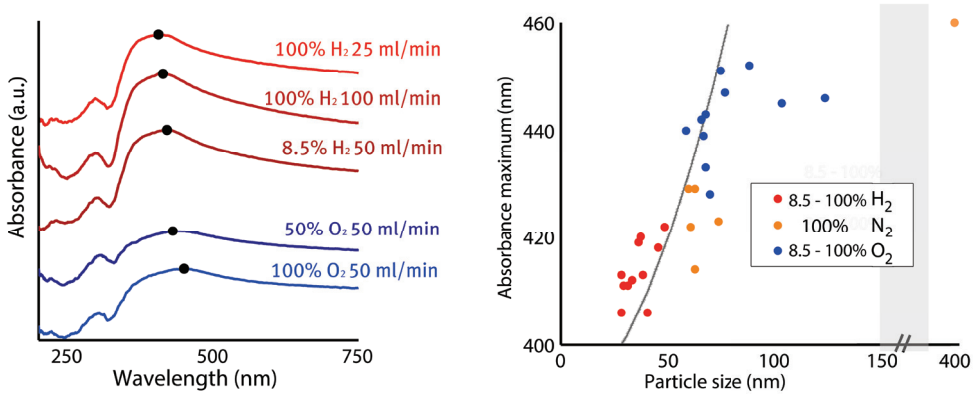

Figure 2.2: UV/Vis spectra of Ag/α-alumina with a range of particle sizes. Displayed spectra obtained from (from top to bottom) $AgAl_2O_3$_100%H2_25, $AgAl_2O_3$_100%H2_100, $AgAl_2O_3$_8.5%H2_50, $AgAl_2O_3$_50%O2_50, *and* $AgAl_2O_3$_100%O2_50. *The spectra are offset for clarity (left). Surface plasmon resonance peak position as determined by UV/Vis compared to the particle size of silver particles on α-alumina as determined by electron microscopy. Theoretical SPR peak position obtained from simulations of silver particles in a 60% air, 40% α-alumina environment obtained with Lumerical software package is indicated by grey line. Catalyst* $AgAl_2O_3$_350_100%N2_0 *with large silver particle size added as a reference (right).*

The surface plasmon peak maximum as obtained from DR UV/Vis and the average particle size from SEM are summarized in Table 2.2, while in the right frame of Figure 2.2 the SPR peak position of differently heat-treated samples is plotted against the surface averaged particle size obtained by electron microscopy. The dotted line is obtained from computational results of the SPR peak maximum for different silver particle sizes. The resulting peak maximum can only be used to predict an average silver particle size, as only a single silver particle is simulated for each size. The effects of particle and size distributions are therefore not taken into account. Catalysts with the smallest silver particle sizes, like the samples obtained by heat treatment in hydrogen, show intense and sharp SPR peaks in the UV/Vis spectra with maxima at relatively low wavelengths. Catalysts with a larger average particle size in SEM, like the samples treated in oxygen containing atmosphere show a much broader peak with a SPR peak maxima at higher wavelengths. UV/Vis spectra with SPR peaks up until circa 440 nm, or silver particle sizes of circa 75 nm, are intense enough for a proper estimation of the average silver particle size. For larger particle sizes the values obtained using electron microscopy start to deviate strongly from the value from UV/Vis due to the low absorption coefficient of these large silver particles. A reference catalyst with a surface averaged particle size of 500 nm was analyzed; this catalyst is denoted as *AgAl2O3_350_100%N2_0*. The reference catalysts exhibited a weak surface plasmon resonance at 460 nm. This confirmed that it is possible to estimate the silver particle size for catalysts with average silver particles up to 75 nm.

Table 2.2: Average silver particle size of all synthesized catalysts as determined with SEM and DR UV/Vis.

Gas composition	Particle size									
	0 mL min^{-1}		10 mL min^{-1}		25 mL min^{-1}		50 mL min^{-1}		100 mL min^{-1}	
	SEM (nm)	SPR (nm)	SEM (nm)	SPR (nm)	SEM (nm)	SPR (nm)	SEM (nm)	SPR (nm)	SEM (nm)	SPR (nm)
100% H_2	36	419	31	411	28	406	28	413	20	413
50% H_2	n.d.	414	n.d.	412	n.d.	n.d.	n.d.	427	n.d.	422
20% H_2	n.d.	n.d.	n.d.	n.d.	29	411	n.d.	n.d.	n.d.	n.d.
8.5% H_2	40	406	45	418	33	412	48	422	37	420
100% N_2	73	423	62	414	60	422	62	429	59	429
8.5% O_2	65	442	58	440	69	428	67	443	66	439
20% O_2	n.d.	n.d.	n.d.	n.d.	74	451	n.d.	n.d.	n.d.	n.d.
50% O_2	n.d.	n.d.	n.d.	418	n.d.	n.d.	n.d.	435	n.d.	458
100% O_2	123	446	67	433	103	445	76	447	88	452

n.d. Particle size not determined with the specified method.

2.3.2 Effect of gas flow during precursor decomposition

An overview of the surface averaged particle size of samples treated under different gas atmospheres and gas flows are given in Figure 2.3. Particle sizes obtained both from electron microscopy techniques as well as from UV/Vis are included. The average particle size clearly increases going from more reducing to more oxidizing atmospheres. When the heat treatment is performed in static conditions, the final silver particle size is slightly higher than for catalysts treated in a gas flow. A linear fit excluding the data from catalysts obtained under static conditions is added as dashed line as a guide for the eye.

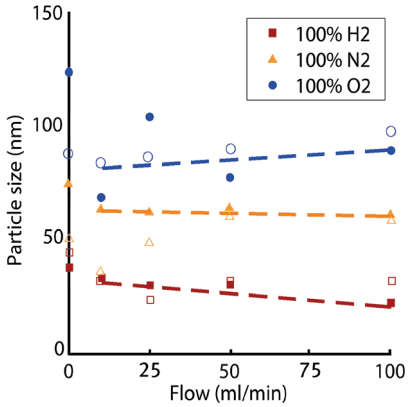

Figure 2.3: Particle size of silver particles on a-alumina as determined by electron microscopy (closed symbols) and UV/Vis (open symbols) after heat treatment in different gas atmospheres (hydrogen or oxygen in nitrogen) with different flow rates over 150 mg of sample. Dashed lines added as a guide for the eye.

The trends observed in Figure 2.3 show a pronounced effect of gas atmosphere during heat treatment, while in general, the effect of flow is less prominent. The slightly higher average silver particle size in catalysts obtained in static conditions is attributed to the poor removal of decomposition products, while at intermediate or high flows this removal is facilitated. Overall, the method of heat treatment in different atmospheres is successful in producing catalysts with a

broad range of silver particle sizes. A small amount of hydrogen, exemplified by 8.5% hydrogen in nitrogen, already results in very small particles, while the size of the silver particles increasing with increasing oxygen partial pressure, as can be seen in Table 2.2.

2.3.3 Decomposition of silver precursor

In Figure 2.4 the weight loss during heating of the $[Ag(en)_2]_2C_2O_4$/α-alumina catalyst precursor in different gas atmospheres is plotted. Prior to analysis the sample was dried to remove water and ethylene diamine. This resulted in the formation of $Ag_2C_2O_4$/α-Al_2O_3 which should exhibit a weight loss of 5.8 % when decomposed fully into Ag/α-Al_2O_3 and CO_2. The total weight loss observed in the thermographic analysis (TGA) is 4.8 %, which agrees within the error of the measurement with the expected weight loss. In the derivative of the TGA (DTG) a sharp peak can be seen, which represents decomposition of the complex, with a small shoulder at higher temperatures. Between 150 and 200 °C an additional decomposition peak is visible in all three cases. The onset decomposition temperature is slightly higher for inert and oxidizing atmospheres (for the main decomposition peak at 73 °C for H_2 versus 84 and 86 °C for argon and air respectively). At 250 °C a sharp weight loss of 0.4 % is observed in the measurement in oxidizing atmosphere, while no such decomposition step is visible in inert or reducing atmospheres. The final weight is referenced to the sample measured in inert atmosphere, as the samples after heat treatment all resulted in 15 wt% Ag/α-alumina.

The fact that the initial weight of some samples exceeds 100% at the start of the measurement is attributed to the residual water content of the sample and not fully complete removal of ethylene diamine prior to analysis. Mass spectrometry analysis predominately shows the formation of CO_2. Less than 0.3 at% of the decomposition products are N-containing compounds from ethylene diamine decomposition, and less than 2 at% water. XRD patterns of the catalyst at different stages of decomposition only showed silver oxalate and silver.

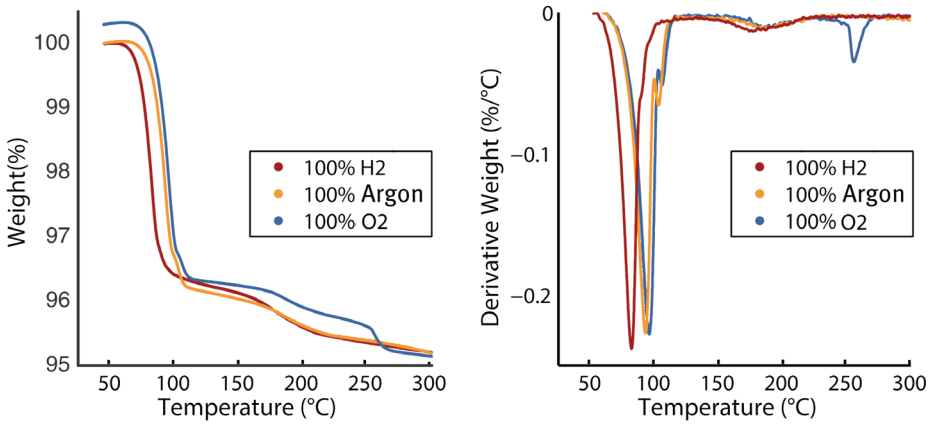

Figure 2.4: TGA (left) and DTG (right) of $[Ag(en)_2]_2C_2O_4$/α-Al_2O_3 in hydrogen (red), argon (orange) and oxygen (blue) with a flow of 10 mL min^{-1} in a background flow of 20 mL min^{-1} inert. Samples dried in situ in inert gas flow at 70 °C before analysis.

The additional minor weight loss around 170 °C in all three gas atmospheres can be attributed to the formation of a passivation layer around the oxalate during the main decomposition step,

retarding full decomposition. This behavior of silver oxalate during decomposition was also observed by MacDonald in 1936 and Leiga in 1966 in their research on the decomposition of bulk silver oxalate.[210,211] The ratio of the different weight loss steps depends on the crystal shape and size and hence varies with the preparation method of the silver oxalate and the measurement conditions.[201,212]

The results of TGA-MS and XRD show that the decomposition steps are primarily caused by a one-step decomposition of $Ag_2C_2O_4$, drying of the samples before the measurement removed most of the ethylene diamine and water. No major contributions of decomposition of ethylene diamine (en) or evaporation of water were observed in the MS results and no formation of intermediate products was observed in the XRD during decomposition.
The slight shift of weight loss toward lower temperatures during the decomposition in hydrogen is probably caused by its high thermal conductivity rather than by an intrinsically different decomposition mechanism. The decomposition step in at 250 °C in oxidative atmosphere could be caused by the formation of silver oxide during decomposition at lower temperatures, which decomposes around 250 °C. Part of the silver oxalate could have been converted to amorphous Ag_2O, which would not be directly visible in XRD. When all the oxalate would undergo formation of silver oxide and subsequent decomposition to metallic silver a weight loss of 1.05 % above 200 °C is expected, while a weight loss of 0.25 % is observed. The formation of a small amount of silver oxide most likely explains the larger silver particle sizes obtained in oxidizing atmosphere, as silver oxide is known to be mobile on the support surface.[213]

2.3.4 Temperature dependence of catalytic performance

A typical temperature program and resulting ethylene conversion and selectivity to ethylene oxide are displayed in Figure 2.5 for catalyst *$AgAl_2O_3$_100%O2_25*. The spikes at the start of each temperature dwell are caused by an overshoot of the temperature controller, causing similar spikes in conversion and selectivity as is visible in the top left frame. The conversion (orange line) increases steadily with temperature, while the selectivity (blue line) decreases with temperature. In the right frame, the conversion at different temperatures from three catalysts over a range of particle sizes is displayed. The drawn lines represent the fitting with an Arrhenius-type equation. The ethylene conversion levels off at 12%. This is due to the depletion of oxygen from the gas stream. Small amounts of CO and acetaldehyde were observed at conversions exceeding 12%. At lower conversions, carbon dioxide and water were the only side products observed. Catalytic key parameters, turnover frequency and selectivity, are calculated from data obtained at conversions below 5%. The absence of external and internal transport limitations at these conditions was established by using the Mears and Weisz-Prater criteria.[214]

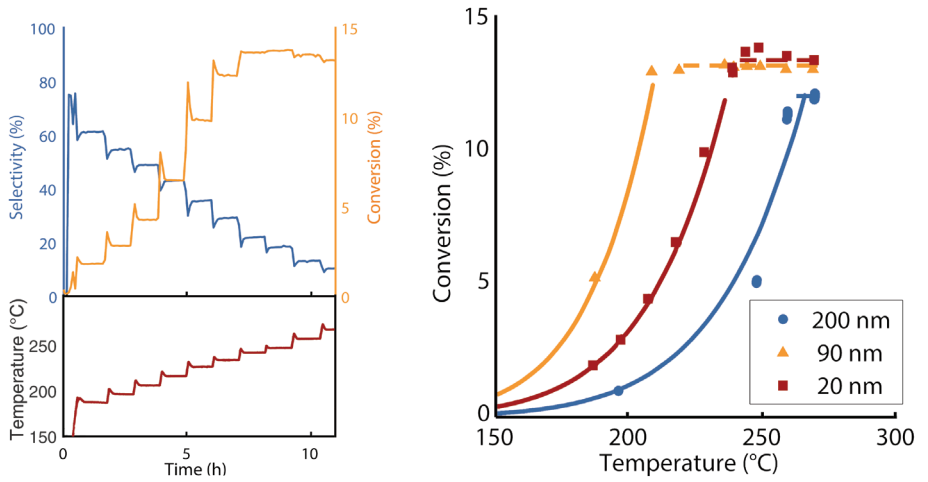

Figure 2.5: Conversion of ethylene (orange) and selectivity towards ethylene oxide (blue) of $AgAl_2O_3$_100%O2_25 *(top left frame), with corresponding reactor temperature (bottom left frame). Conversion data of three selected catalysts plotted against temperature fitted with an Arrhenius equation (right frame). Data obtained at atmospheric pressure in a temperature range of 180 – 270 °C with 8.5%* O_2 *and 30% ethylene flow in helium and a GHSV of 6.000* hr^{-1}.

The silver time yield (STY) of silver catalysts with different particle sizes, defined as the amount of moles ethylene converted per gram of silver per second, can be found in Figure 2.6. The STY of small particles is relatively low and reaches a maximum at a particle size of about 60 nm. Above this size, the STY scales inversely with particle size. The right frame shows the activity per exposed silver surface, better known as the turnover frequency or TOF, which is low for small particles and increases with particle size up to about 60 nm.

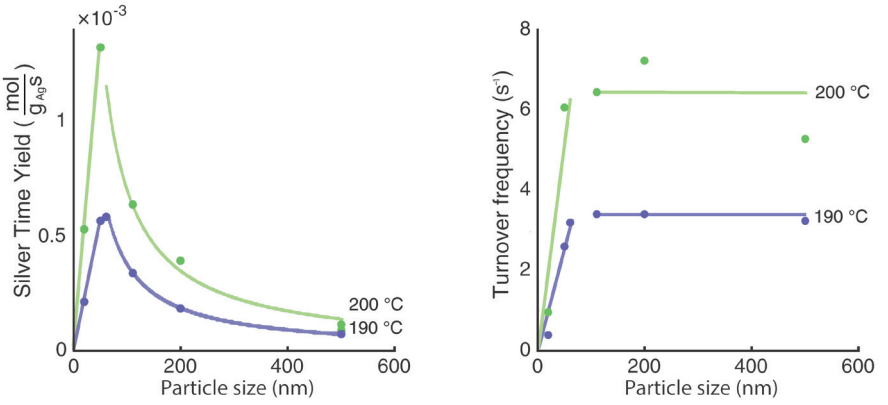

Figure 2.6: Silver Time Yield of Ag/a-Al_2O_3 *catalysts with different average Ag particle sizes (left frame) and turnover frequency as a function of average Ag particle size for ethylene epoxidation of Ag/α-*Al_2O_3 *catalysts (right frame). In both frames lines are added to guide the eye. Catalytic data obtained at atmospheric pressure with 8.5%* O_2 *and 30% ethylene flow in helium and a GHSV of 6.000* hr^{-1} *at 190 and 200°C and conversions ranging from 0 – 4.5%.*

The observed decline in STY for larger particles is expected due to a decline in exposed active sites per gram of silver with increasing particle size. The low activity for small particles points to an intrinsic particle size effect. The overall trend in activity is in good agreement with literature where a similar sharp decline in turn over frequency at particle sizes below 60 nm was reported.[55,60,135,158] The observed turnover frequencies agree with those observed in academic as well as patent literature.[72,190]

2.3.5 Particle size dependence of selectivity

The selectivity to ethylene oxide as a function of temperature is displayed in the left frame of Figure 2.7 for catalysts with surface averaged particle sizes of 20, 90 and 200 nm. The selectivity decreases linearly with temperature until a certain temperature, after which the decline becomes less pronounced. The steep decline of selectivity with temperature is due to the fact that the selectivity strongly decreases with increasing conversion levels, as will be discussed later. The inflection point in the selectivity corresponds to the temperature at which the conversion flattens off due to oxygen depletion as discussed above. The selectivity of the sample containing 90 nm silver particles decreases with temperature more sharply than the samples containing 20 or 200 nm silver particles. In the right frame in Figure 2.7, the selectivity at 190 °C as a function of particle size is shown.[135,158] The particle size dependency at constant temperature corresponds to the trends reported in literature, showing a slight apparent *(vide infra)* increase in selectivity with particle size.

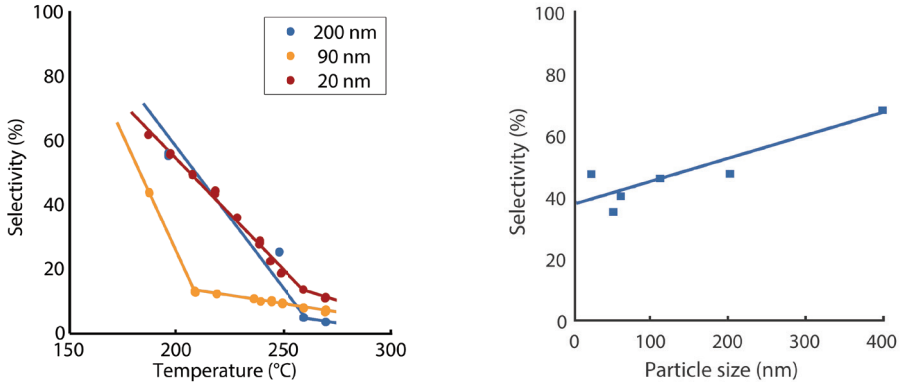

Figure 2.7: Selectivity to ethylene oxide as a function of temperature (left) and particle size (right) at 190 °C for ethylene oxidation of $Ag/\alpha\text{-}Al_2O_3$ catalysts. Catalytic data obtained at atmospheric pressure with 8.5% O_2 and 30% ethylene flow in helium and a GHSV of 6.000 hr^{-1} with conversions ranging from 0 to 4.5%.

In contrast, the selectivity at a constant conversion of 2.8 % plotted in the left frame of Figure 2.8 shows no significant particle size dependency. In the right frame, the selectivity over the entire conversion range is plotted against the conversion. Different temperatures have been used to obtain the same conversion for catalysts with different particle sizes, the selectivity of all catalysts falls on the same line. It should be noted that this method of varying temperature could introduce differences in selectivity, due to different activation energies of the selective and unselective reaction pathways.

The decrease in selectivity in the left frame of Figure 2.7 is caused by an increased rate of the secondary reaction, subsequentially oxidation of ethylene oxide. This is due to an increased conversion with temperature, increasing the partial pressure of the primary reactant of this secondary reaction, ethylene oxide. The overall selectivity of the reaction is reduced due to this effect. This also plays a key role in the right frame of this figure. In this frame, the selectivity is reported at constant temperature, but at different conversion. The conversion-dependence of the selectivity introduces a systematic error in the particle size effect.

In the left frame of Figure 2.8 the selectivity at constant conversion is reported, both at constant GHSV (open symbols) and at constant temperature (closed symbols). For both cases no apparent particle size dependency can be observed. This shows that the selectivity is primarily conversion-dependent, instead of particle size dependence.

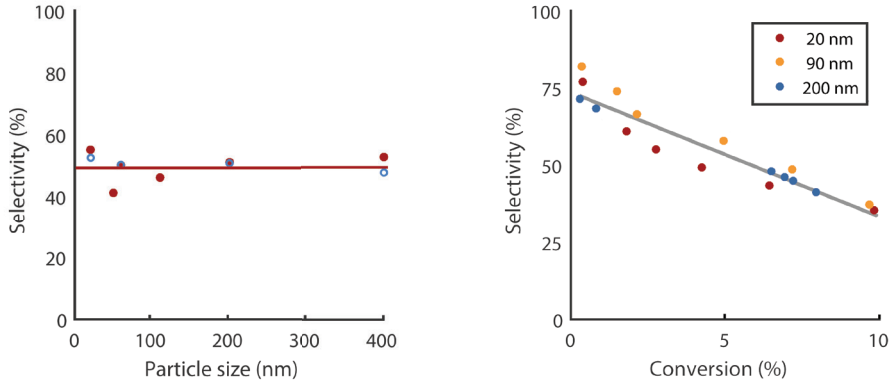

Figure 2.8: Selectivity as a function of particle size for ethylene epoxidation of $Ag/\alpha\text{-}Al_2O_3$ catalysts at constant conversion (2.8%, left frame). Data corresponding to the open symbols is obtained at constant temperature and conversion, while closed symbols are obtained at constant GHSV and conversion. Selectivity versus conversion of silver catalyzed epoxidation (right). Catalysts with different particle size show that selectivity is conversion dependent, while all three catalysts follow the same trendline.

The selectivity data at constant conversion suggest that the selectivity is either particle size independent or only slightly particle size dependent. Both the data points measured at different temperatures and at constant temperature show a similar trend. This is attributed to a small influence of temperature on the overall selectivity, in correspondence with the small difference between the activation energy of ethylene epoxidation and full oxidation.[97,212] While the particle size independent selectivity does not agree with previous results reported in literature, these studies were either performed at constant temperature, which obscures the selectivity with the temperature dependence of conversion, or by using model catalysts consisting of Ag single crystal planes.[111,137]

Although we clearly show a strong particle size dependence (for particle sizes below 60 nm) of the intrinsic activity, the selectivity is not significantly affected by particle size in this range. The understanding of this particle size dependence is therefore not straightforward. It might be expected that the occurrence of certain crystal planes, such as the silver (100) crystal plane,

depends on particle size, but there is no consensus in literature that this should have a strong influence on the intrinsic activity for ethylene epoxidation, and one might expect that if this would be an important factor, also the selectivity would be expected to be size dependent.[111,113]

Rather it seems likely that oxygen plays a decisive role. As posed by several authors, the nature of the sites that bind and activate ethylene critically depends on the presence and nature of oxygen on the silver surface.[110,115,119,133,134,136,193,195] The size dependent activity depicted in Figure 2.6 is caused by a very low occurrence of active sites on small silver particles. Generally it has been posed that sites related to "nucleophilic" or "ionic" oxygen are rare for silver particles up to sizes of 30-50 nm.[115,118,119,133,136,193] However, the fact that we do not observe, in the same particle size region, a dependence of the selectivity on particle size, implies that the concentration of these active ethylene binding sites does not determine the selectivity of the reaction. In other words, it determines the activation of the ethylene molecule, but not its fate, while apparently there are no alternative binding sites on the silver that lead to conversion. Dedicated measurements on the dependence of the occurrence of the different oxygen containing sites as a function of Ag particle size and correlating them to activity and selectivity observed could shed further light on this phenomenon.

2.4 Conclusion

A study of the synthesis of supported silver catalysts by decomposition of silver oxalate showed that different silver particle sizes can be obtained without changing the weight loading or the catalyst precursor, by using different gas atmospheres. The obtained particle sizes were in a range of 20 – 500 nm, with hydrogen gas treatment yielding 20 nm silver particles. While the catalysts have different average silver particle sizes, the support and metal loading are identical. The clear surface plasmon resonance absorption by small silver particles observed in UV/Vis correlates with particle sizes from electron microscopy techniques (SEM and TEM) and can therefore be used as a fast and statistically relevant analysis technique for the silver particle size.

The effect of the particle size on the ethylene epoxidation activity is in good agreement with literature. This shows the validity of our synthesis method. We additionally show that the selectivity is strongly dependent on conversion. This means that reporting the selectivity at a constant temperature, as is commonly done in relevant literature, introduces major artifacts. When the selectivity is reported at constant conversion, no clear particle size dependence of selectivity was observed, in contrast to most literature reports. While different silver crystal planes may have different selectivities to ethylene oxide as indicated by surface science experiments,[111,113,195] the particle size independence of the selectivity shows that this does not play an important role in more industrially relevant model catalysts, like the ones studied here.

2.5 Acknowledgements

This research was funded by NWO Vici project no. 16.130.344. Jan-Willem de Rijk is aknowledged for the DSC measurements, Carlo Buijs and Marlies Coolen-Kuppens for their help on the epoxidation setup, Helen de Waard (Geochemistry, Utrecht University) for the ICP analysis and Lisette Pompe for the TEM measurements. The European Research Council, EU FP7 ERC Advanced Grant no. 338846 is thanked for funding of the TEM measurement time.

Preparation of ordered macroporous α-alumina

This chapter is based on: Materialia, 4, pp. 423-430, 2018.

3

Abstract

Ordered porous materials are highly relevant as support material in catalysis, but also for applications in fields such as adsorption and chromatography. Strategies such as soft and hard templating are now routinely applied to prepare for instance ordered mesoporous silica. In other cases, most notably when several polymorphic phase transformations are involved, achieving high quality ordered oxides is challenging. We present a strategy for the preparation of ordered macroporous α-alumina with a high degree of pore order. The preparation is based on impregnation of ordered polymeric spheres with an alumina precursor. Most notably it involves a first heating step in inert atmosphere, leading to conversion of the polymeric template into carbon, effectively delaying the phase transitions and stabilizing the pore structure up to high temperatures. A subsequent heat treatment in oxidative atmosphere then removes the carbon and ordered marcoporous α-alumina is obtained with circa 200 nm cages interconnected by windows of circa 100 nm, and a specific surface area of circa 25 $m^2 g^{-1}$. Our method led to a strong preservation of the long-range order of the pore structure, as not only evidenced by electron microscopy, but also quantified by spectroscopy. High surface area α-alumina is of particular interest as a catalyst support, but the preparation method might also be extended to other ordered macroporous oxides that are difficult to prepare due to phase transitions such as TiO_2.

3.1 Introduction

Typical industrial catalysts in the epoxidation of ethylene consist on silver supported on low surface area, non-porous support material, such as those described in chapter 2. However, most other types of industrially relevant support materials have a high surface area due to the presence of intrinsic porosity.[7]

Several important porous materials, such as zeolites and clays, occur naturally. However, a great step forward was the synthesis of new classes of porous materials in the laboratory. This started in the 1940s with synthetic zeolites, which are now used on a wide scale as catalysts, softeners and adsorbents.[215] Zeolites are prepared by using small ions or molecules as templates during hydrothermal growth, and hence the pore sizes are typically in the microporous (< 2 nm) regime.[215] Another breakthrough was the first synthesis of ordered mesoporous (2 – 50 nm) silica (MCM-41), as reported in 1992.[216] In this case, the mesoporous silica was formed around a template of micelles, consisting of long hydrocarbon chain surfactants or block copolymers.[216–218] The mesoporous materials do not consist of crystalline silica, but do have a very well defined pore ordering, and a very narrow pore size distribution. Some examples of applications of ordered mesoporous materials are chromatography, drug delivery and catalysis.[219–222] These ordered mesoporous systems also served as model systems to advance fundamental understanding, allowing advanced characterization and to systematically investigate the influence of parameters on catalyst synthesis and performance.[223–226]

Using these soft templating methods, the pore size is limited by the size of the organic templates or their micelles, which goes up to roughly 10 nm, with a further extension to circa 30 nm by micelle swelling.[218,227,228] Porous materials with larger pore sizes, such as pores in the macroporous regime (> 50 nm), can be synthesized by using techniques such as foaming, emulsion templating or flame spray pyrolysis,[225,229–231] but in these cases the pore size distribution is usually wide and pore ordering is absent or poorly controlled. Sometimes ordered macroporous materials are desired, such as in the epoxidation of ethylene, where the pores need to be large enough to facilitate active silver particles. In this case, hard templates need to be used.[232,233] Velev *et al.* were the first to report on the preparation of three dimensionally ordered macroporous (3DOM) silica.[234] Polymer spheres self-assembled into a so called "colloidal crystal" were used as a sacrificial template, whereupon silica was grown in the voids of these colloidal crystals, followed by template removal. This method proved to work also for other three dimensional ordered macroporous materials, such as ZnO, Fe_2O_3 and Cr_2O_3.[235–239]

While 3DOM silica is relatively easily synthesized, the synthesis of ordered porous metal oxide phases that need a high temperature to be formed is challenging.[240] α-alumina, the typical support material used in ethylene epoxidation,[78,84,241] is notoriously difficult compound to synthesize as a porous material, as illustrated for instance by Sadakane *et al.* who prepared a range of ordered materials, but failed to form ordered porous α-alumina.[242] α-alumina is the most stable alumina phase at high temperatures and can be formed from other alumina polymorphs above 1100 °C. In principle, due to its chemical and thermal inertness, α-alumina is very attractive as a catalyst support, and indeed the support of choice for catalysts used in large industrial processes such as ethylene epoxidation over a supported silver catalyst. However, in catalysis, large specific support surface areas (preferably >10 $m^2\ g^{-1}$) are often crucial, while this is extremely difficult to achieve with α-alumina. Commercial α-alumina exhibits typically a specific surface area of only about 1 m^2

g^{-1}, with 8 m^2 g^{-1} being the highest specific surface area reported.[177,178,243] The material goes through several crystal phase transitions to form α-alumina from alumina precursors or other alumina polymorphs, which leads to a severe loss in specific surface area.[7,170,244]

Alternative preparation methods for the preparation of high surface α-alumina have been explored. In patent literature, a method is reported involving incorporation of a carbon template in γ-alumina followed by two thermal treatments, first in inert atmosphere to obtain α-alumina and a second treatment in oxidizing atmosphere to remove the carbon.[178] Similar methods were used by Martin-Ruiz *et al.*, Pérez *et al.* and Furlan *et al.*, in which alumina was formed in the presence of a polymer.[245–247] Using these methods, α-alumina with a specific surface area up to 70 m^2 g^{-1} was produced,[178] but without a well-defined pore size or structure. As far as we are aware, the only successful synthesis of ordered macroporous α-alumina has been reported by Sokolov *et al.*, who used self-assembled poly(methyl methacrylate) (PMMA) spheres as a sacrificial template.[248] Such a polymeric template cannot withstand high temperatures in air, but nevertheless ordered macroporous α-alumina was formed at higher temperatures (1150 °C), as apparently enough of the template remained during the heating to offer some stabilization of the structure during the phase transitions.

Inspired by these results, we designed a new strategy to prepare high surface area ordered macroporous α-alumina with a very high-quality pore structure. We used self-assembled PMMA sphere crystals to start with as templates in-situ into a protective carbon coating, followed by the formation of alumina in the presence of this protective carbon at higher temperatures but still in inert atmosphere. Subsequently, in a separate oxidative treatment step, the carbon coating was removed and full conversion to α-alumina took place. This strategy allows the formation of high quality ordered macroporous α-alumina material with specific surface areas of 25 m^2 g^{-1}, as is evidenced in this chapter using detailed electron microscopy and reflectance spectroscopy. In chapter 4, we build on this material to show the effect of the support morphology and surface area of the support on the stability of supported silver particles, and in chapter 5, to show the effect this and other support materials have on the selectivity during the selective oxidation of ethylene.

3.2 Experimental section

3.2.1 Synthesis Polymeric template

Poly(methyl methacrylate) (PMMA) spheres were synthesized by using the surfactant free emulsion polymerization of methyl methacrylate (MMA, 99%, ≤30 ppm 4-methoxyphenol inhibitor, Sigma-Aldrich) in water. Following the procedure of Zhou *et al.* and Schroden *et al.*, 100 mL MMA and 400 mL demineralized water in a 1 L round bottom flask were stirred by an overhead stirrer at 450 rpm.[249,250] The emulsion was heated to 70 °C and nitrogen was bubbled through the emulsion for at least 30 minutes to remove dissolved oxygen from the dispersion and to deactivate the inhibitor. Thereafter, 69 mg potassium persulfate (KPS, initiator) was added, resulting in a 0.5 mM concentration. The emulsion was left to react for 3 hours at 70 °C after which a white dispersion had formed.

The dispersion was allowed to cool down to room temperature and was filtered to remove larger chunks of polymer. The filtrate was centrifuged for 1 hour at 3000 rpm during which a white solid precipitated. The clear supernatant was decanted, and the obtained white powder was left to dry for several days at room temperature in air after which it was crushed into a powder.

3.2.2 Ordered macroporous alumina

Three dimensionally ordered macroporous (3DOM) α-alumina was obtained by impregnation of the polymeric template with an alumina precursor.[249,251] In a typical synthesis, 1.5 g template powder was placed in a Buchner funnel and drop-wise approximately 3 mL solution of 1 M aluminum nitrate nonahydrate in demineralized water/methanol (1:1 volume ratio) was added to completely wet the template. After 2 minutes of soaking, a dynamic vacuum was applied for 20 minutes to remove excess solvent. Subsequently, the dry powder was wetted with 3 mL ammonia (28-30%)/ methanol (1:1 volume ratio) to form aluminum hydroxide in the pores of the template. Again, the material was dried via vacuum suction for 20 minutes. In order to obtain sufficient filling of the pores, these steps were performed one, three or four times before drying the powder overnight at room temperature in air.[249,251] Note that to maximize the pore filling, each impregnation consisted out of two different steps; firstly, an impregnation with an $Al(NO_3)_3 \cdot 9H_2O$ solution and secondly a washing with an ammonia solution to form $Al(OH)_3$.

The once and four times impregnated template materials were calcined in a flow of air of at least 0.5 L min^{-1} (GHWV = 20 L $g_{template}^{-1}$ hr^{-1}), heated with a 5 °C min^{-1} heating ramp to 1150 °C and kept at this temperature for 6 hours, in similar fashion to established procedures.[248,249,251] The resulting samples were labeled 3DOM_1_air and 3DOM_4_air, indicating the amount of impregnation steps and the gas atmosphere respectively (Table 3.1). 1.5 g of dry, three times impregnated material was heated under a nitrogen flow with a 5 °C min^{-1} heating ramp to 1150 °C and kept at this temperature for 6 hours. The resulting material was black, or dark blue/green and a second heat treatment in a flow of air with the same flow and temperature program was applied after which a pristine white powder was obtained. The resulting sample was labeled 3DOM_3_N2_air. For temperature studies, the impregnated material was heated separately in air or in nitrogen flow to 200 °C, 400 °C, 600 °C, 800 °C, 1000 °C and 1150 °C. As reference material, bulk aluminum hydroxide was prepared by mixing an equal amount of the above described aluminum nitrate and ammonia-methanol solutions without template present. This material was heated in air flow to 200 °C, 400 °C, 600 °C, 800 °C, 1000 °C and 1150 °C.

Table 3.1: Overview of the synthesis parameters for 3DOM alumina samples.

Sample	Heat treatment(s)	Number of impregnation steps
3DOM_1_air	Air	1
3DOM_4 _air	Air	4
3DOM_3_N2_air	Nitrogen and air	3

3.2.3 Characterization

The polymer template and 3DOM powders were analyzed using Scanning Electron Microscopy (SEM) with a FEI XL30 FEG operated at 15 kV, and FEI Helios G3 UC operated at 2 kV. The micrographs were processed using iTEM Soft Imaging System software.[204]

Diffuse-Reflectance UV/Vis spectra of the PMMA powder and the 3DOM materials were obtained using a Varian CARY 500 Scan UV/Vis-NIR spectrophotometer with an integrating sphere detector. In a typical analysis of the 3DOM materials, 30 mg of analyte was diluted with 600 mg pristine α-Al_2O_3 (1 m^2 g^{-1}, 100 mesh, Sigma-Aldrich) and ground into a fine powder before taking a spectrum of the 1000 – 200 nm range. A background measurement of pristine α-Al_2O_3

was taken which was automatically subtracted from the obtained spectrum. Crystal phase analysis was performed with X-Ray Diffraction (XRD) on a Bruker D8 Phaser diffractometer equipped with a Co Kα source (λ = 0.1789 nm) using an angle range from 20° to 90° in 2θ and comparing XRD diffractograms with the PDF-4+ 2016 database. Crystallite sizes were estimated using the Scherrer equation.[252,253]

Nitrogen physisorption isotherms were measured at -196 °C on a Micromeritics TriStar 3000 apparatus. The specific surface area of the support was calculated using the BET equation ($0.05 < p/p^0 < 0.25$). Mercury porosimetry was performed using a Micromeritics AutoPore IV 9500 in the Chemical Reactor Engineering group at the Eindhoven University of Technology. Pore volume data were calculated over the range 0.0007 – 227.5270 MPa, assuming a contact angle between the support materials and the mercury of 130° and mercury surface tension and density of 485 dynes cm^{-1} and 13.5335 g cm^{-3}, respectively.

3.3 Results and discussions

3.3.1 Polymer template

In Figure 3.1, a Scanning Electron Microscopy (SEM) image of the polymeric template after centrifugation and drying is shown. In the inset, a histogram of the sphere diameter is added. The average sphere size is 400 ± 24 nm. The monodispersity of the particle sizes can be seen from the histogram and from visual inspection of the image. The deposition of the spheres was relatively slow, allowing the formation of a hexagonally ordered structure (a "crystal") as a close packing minimizes the energy of the system.

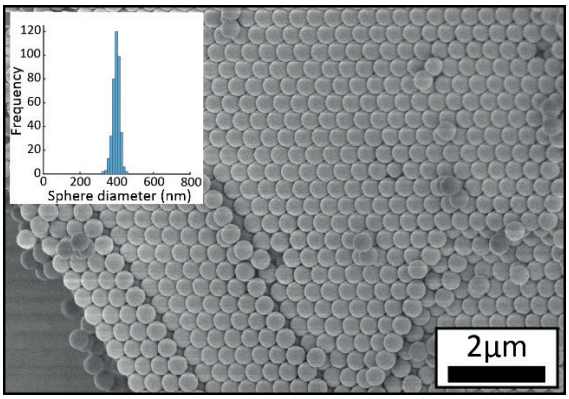

Figure 3.1: SEM image of PMMA spheres ordered in a colloidal crystal after centrifugation with histogram of the particle size distribution in the inset. Average particle size was 400 ± 20 nm respectively.

Diffuse-reflectance (DR) UV/Vis spectroscopy showed that the closed packed ordering of the polymer spheres is not only present at the surface, but also at the center of the colloidal crystal particles. In the DR UV/Vis spectrum (Figure 3.2), three peaks are visible. Assuming a closed packed ordering of the polymer spheres, the two most intense peaks at 895 and 450 nm are assigned to second and first order diffraction of the nearest neighbor spheres in a close packed structure ((222) and (111) crystal planes), while the least intense peak (780 nm) corresponds to the second order next nearest neighbor diffraction (200). By assuming a closed packed crystal structure, an average sphere diameter of 404 ± 20 nm was calculated, which is in agreement with the particle size measured with SEM and dynamic light scattering.

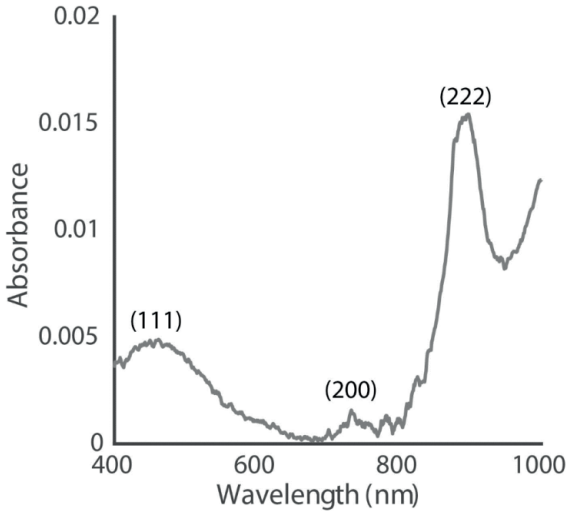

Figure 3.2: DR UV/Vis spectrum of the template with peaks corresponding to 400 nm PMMA spheres in a colloidal crystal. Peak positions at 450, 780 and 900 nm correspond to (111), (200) and (222) plane reflections of the PMMA spheres, respectively.

3.3.2 The formation of macroporous α-alumina

InThe polymeric template was used to synthesize macroporous α-alumina. However, upon decomposition of aluminum hydroxide at 400 °C, first γ-alumina is expected to form, while α-alumina should be formed above 1100 °C.[7,254] When bulk alumina hydroxide without any template is heat treated in a similar procedure, we indeed observe the formation of both phases at the expected temperatures.

Upon heat treatment of the impregnated template in air, the aluminum hydroxide in the voids of the template decomposes and the template is burned off. To understand the effect of the confinement of the hydroxide on the phase transitions, we first evaluated the crystalline phases of alumina in the voids of the template using X-Ray Diffraction (XRD). In the left frame of Figure 3.3, the diffractograms of the composite treated in air at different temperatures are shown. At the bottom of the frame, the diffractogram of the impregnated template before heating is shown, displaying two broad diffraction peaks attributed to the PMMA polymer.[255] With increasing temperature, both the aluminum hydroxide and the polymer peaks disappear and at 600 °C, no diffraction peaks are visible. Broad peaks from γ-alumina appear at 800 °C.[245,256] The broad diffraction peaks indicate that the material consists of relatively small crystallites with sizes of 5 ± 1 nm. These peaks disappear in favor of peaks that are attributed to crystalline α-alumina, which sharpen upon heating to 1150 °C.

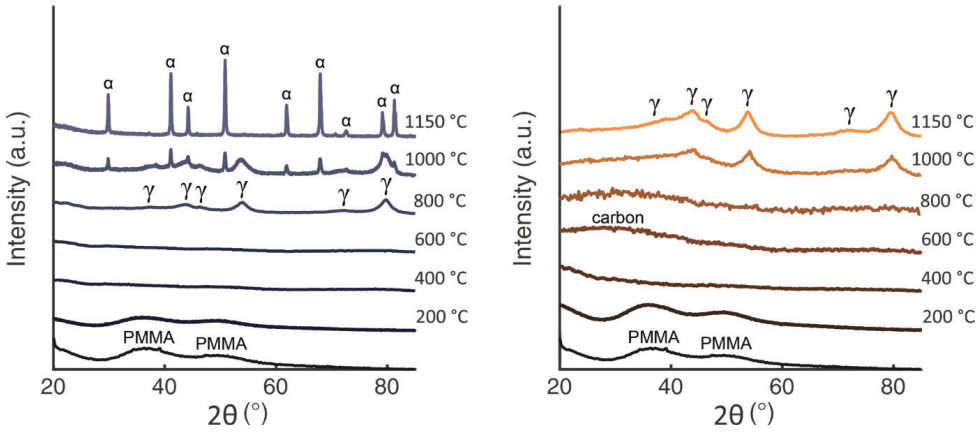

Figure 3.3: Stacked diffractograms of the impregnated template before treatment (bottom line in both frames) and treated at different temperatures in air (left) and under nitrogen flow (right). After the material was treated at 800 °C in air, γ-alumina was formed, converting into α-alumina at higher temperatures. Under inert atmosphere, the formation of γ-alumina was delayed to even much higher temperatures and no α-alumina was yet formed at 1150 °C.

The disappearance of the broad diffraction peaks attributed to the polymeric material at 200 – 400 °C is in accordance with TGA-MS of the material (not shown), showing that in this temperature range, the template is burned off. The presence of γ-alumina at 800 °C and α-alumina above 1000 °C is in accordance with the alumina phase diagram.[257,258] However, compared to the bulk material, the conversion of confined aluminum hydroxide in the voids of the template into γ-alumina is delayed by 400 °C. We believe that this delay is caused by residual template material present at least up to 600 °C.

In the right frame of Figure 3.3, the diffractograms of the impregnated template heat treated under nitrogen flow are shown. The diffractogram of the composite heated to 200 °C is very similar to the diffractogram taken before heat treatment. By heating the composite in nitrogen flow, the decomposition of the polymeric template is delayed compared to when the composite is heat treated in air. When the composite is treated to 400 °C, these broad peaks have disappeared and after heating to 600 °C, another broad peak is visible at 30° 2Θ. This peak was not observed in the material treated in air and is attributed to a carbon material, formed due to pyrolysis of the polymer template. The broad peak is still present in the composite heated at 800 °C, and next to this peak, no other peaks are visible.

The appearance of γ-alumina is delayed to 1000 °C and this phase is still present after heat treatment at 1150 °C. Even after prolonged heating (6 h) at 1150 °C, no crystalline α-alumina was observed. We postulate that the delay in phase transitions is caused by the presence of the formed carbon. Causing a delay in a phase transition is only possible when the carbon and alumina are in close contact. This ensures that carbon can act as a protective layer to stabilize the pore structure even at 1150 °C. The pyrolysis of the template material into a protective carbon coating is supported by the black color observed after the heat treatment in nitrogen flow at 1150 °C. Since at this temperature no α-alumina was formed, carbon free 3DOM γ-alumina with a high-quality pore structure can be obtained by simply burning off the carbon at 900 °C in an oxidizing

atmosphere (route 2 in Figure 3.4). Alternatively, the carbon-coated γ-alumina can be used as a ceramic with altered dielectric properties.[259] Next to the ordered macropores, also some pores in the range of 30 – 90 μm were present in the obtained γ-alumina. The surface area of this material was 85 ± 10 m^2 g^{-1}. By increasing the temperature of the second heat treatment in oxidizing atmosphere to 1150 °C, 3DOM α-alumina was formed (route 3 in Figure 3.4). Although the carbon was burned off before the transformation of γ-alumina to α-alumina, the pore structure was well preserved in the α-alumina, better than in the case of treating impregnated template material in oxidizing atmosphere directly (route 1 in Figure 3.4), as will be discussed in more detail below.

By increasing the amount of impregnation steps, the yield of the ordered macroporous material was increased. The synthesis of the reference material (3DOM_1_air) yielded 20 ± 1 mg $g_{template}^{-1}$, which corresponds to circa 2% of the total pore volume of the template material being filled. The yields for 3DOM_4_air and 3DOM_3_N_2_air were 40 and 30 mg $g_{template}^{-1}$, respectively, and are hence significantly higher. Increasing the number of impregnation steps clearly increases the yield of this procedure, but cannot lead to full pore filling with alumina, as the volume of the precursor ($Al(NO_3)_3 \cdot 9H_2O$) is much higher than the volume of its decomposition product, $Al(OH)_3$, and the final alumina phase. When taking this decrease in volume into account, the maximum achievable yield (assuming 100% pore filling using a single impregnation with $Al(NO_3)_3 \cdot 9H_2O$) is 63 mg $g_{template}^{-1}$. After 4 impregnation steps, we reached 60% of this theoretical value.

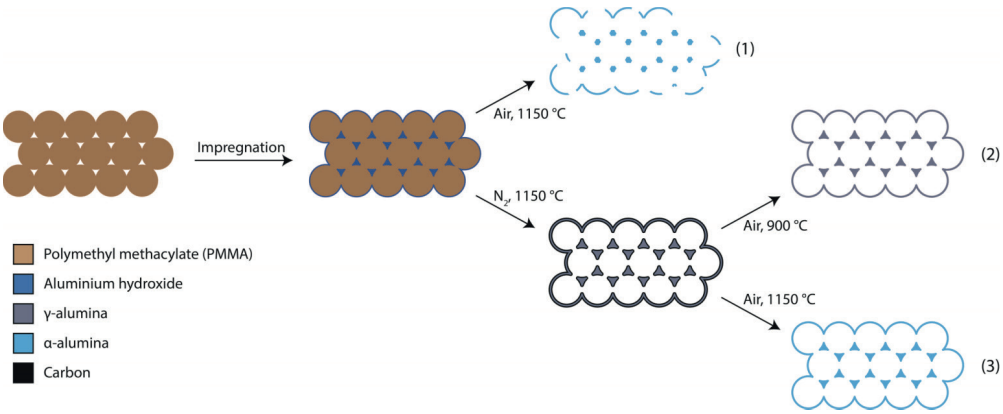

Figure 3.4: Schematic representation of the synthesis procedures of 3DOM α-alumina by reference procedure (1) and the procedures described in this chapter for 3DOM γ-alumina (2) and 3DOM α-alumina (3).

3.3.3 Quality of the pore structure

A crucial part of our strategy for improving the quality of the ordering and pore structure is by stabilizing the morphology by pyrolysis of the template material into a protective carbon coating. Next to that, we investigated the effect of increasing the amount of impregnation steps on the quality of the pore structure. Several techniques were applied to investigate the effect of our strategy on the quality of the prepared macroporous α-alumina. Nitrogen physisorption and mercury intrusion measurements on 3DOM_3_N_2_air showed a specific surface area of 25 ± 10 m^2 g^{-1}, originating from macropores, while micro- and mesopores are absent. This is a very high specific surface area for α-alumina materials and in good agreement with the theoretical expected

value of 14 $m^2 g^{-1}$ for the hexagonal ordered macroporous structure.

This hexagonal structure is shown in Figure 3.5, with SEM images of *3DOM_1_air*, *3DOM_4_air* and *3DOM_3_N_2_air*. The frames in the left column give an overview of the material, while the middle and the right frames show images taken at higher magnifications. We tried to show both the best (middle column) and the worst parts (right column) of the samples. In the left frame on the top row, long-range ordering in the *3DOM_1_air* sample is visible in the overview image. However, the material in this frame consists of sheets of alumina instead of the expected cage-structure, as can be better observed at higher magnifications (right frame). In the middle frame, a higher magnification of another section of the material does show the expected morphology, but this morphology co-exists with the sheets visible in the overview and at higher magnification in the right frame. These observations suggest that the sheets originate from the cage structure, which deformed during phase transitions at high temperature as also observed in the original paper by Sokolov *et al.*[248]

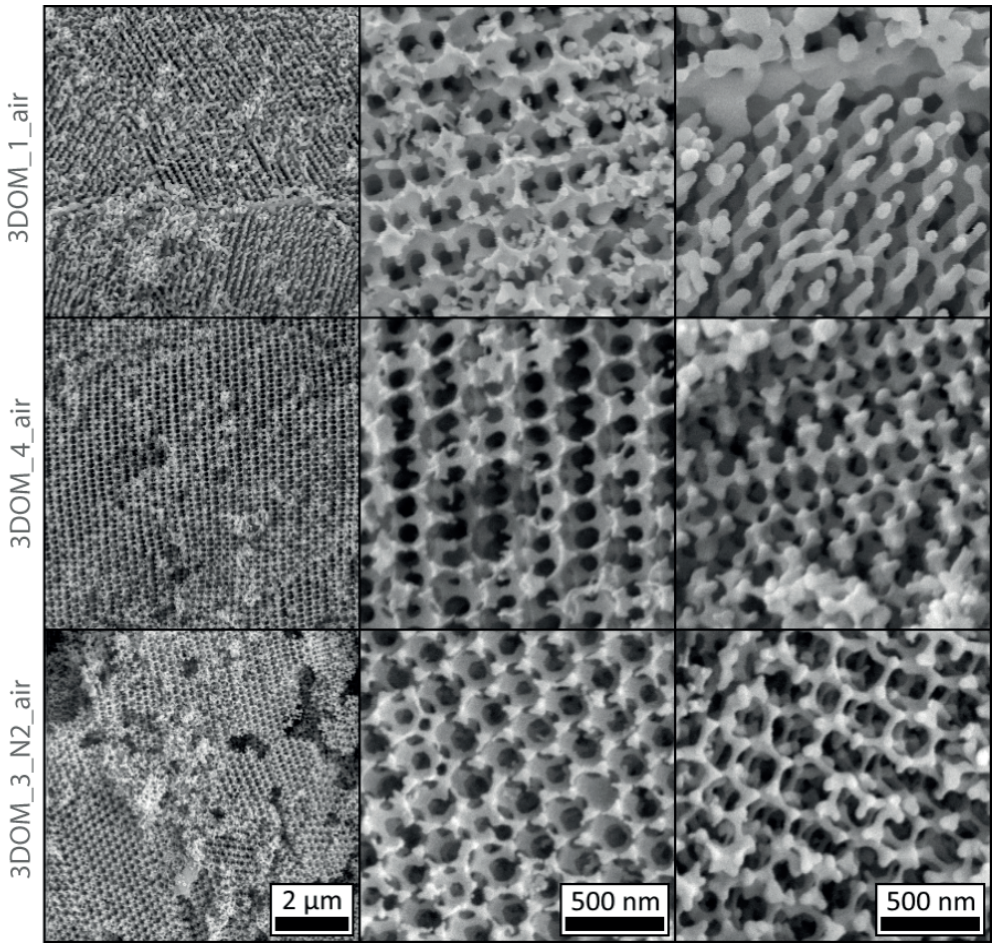

Figure 3.5: SEM images of macroporous a-alumina 3DOM_1_air *(top),* 3DOM_4_air *(middle) and* 3DOM_3_N2_air *(bottom). In* 3DOM_3_N2_air, *pores of 220 ± 15 nm are connected by windows of*

circa 105 ± 5 nm, resulting in a cage structured material. For 3DOM_4_air and 3DOM_1_air, cage structure is not as good preserved, as alumina migrated from the walls of the cages to form pillars.

In the middle row of frames, 3DOM_4_air is displayed. The left frame shows the desired hexagonal cage-structure, although in the middle frame of this row, the cage structure appears to be slightly split, forming an intermediate morphology between the sheets observed in the 3DOM_1_air sample and the desired cage morphology. In the right frame, no sheets are visible, but also no fully formed cages are observed. The material resembles a stick-and-node structure, with some absent sticks on the surface of the material, similar to observations from Rudisill *et al.*[240] In the bottom row, showing the sample prepared by the two-step approach, the cage structure of *3DOM_3_N_2_air* is visible throughout the sample (left frame) and a clear hexagonal ordering is visible at higher magnifications (middle frame). Even for those parts of the material in which the morphology is least preserved, the cages of the material are enclosed by a well-defined stick-and-node structure, and the cage structure is overall preserved.

From SEM it appears that increasing the amount of impregnation steps increases the quality pore structure of the final macroporous α-alumina in comparison to the *3DOM_1_air* sample. In the images in Figure 3.5, the loss of the desired cage structure in these samples seems to result from the transport of the alumina from the thin to the thicker sections of the cage morphology, resulting in a loss of the cage morphology.[240,248,260–262] This transport towards the thicker parts of the structure is driven by the minimization of the surface area. A comparable loss of pore structure was observed for other microporous matrials.[240,260] In the worst case, this transport results in some cages no longer having a wall separating them, or in the formation of α-alumina sheets.

When following our new strategy, the ordered macroporous structure is supported by the protective carbon coating, such as in *3DOM_3_N_2_air*, and the resulting material retains the cage structure and the pore structure is far better than if this carbon coating had not been formed. While the morphology is maintained to a higher degree, the different preparation routes do not have a significant influence on the pore's sizes. An average pore size of circa 220 ± 15 nm was measured. The windows and walls are respectively 105 ± 5 nm and 35 ± 5 nm. The pore sizes are significantly smaller in the resulting macroporous material than the size of the polymer template (400 nm spheres). For all three samples, the reduction of the pore size is similar as they are derived from the same template material. Additional SEM, focused ion beam (FIB)-SEM and transmission electron microscopy (TEM) images in which the pore structure at larger scale and the pore structure on the inside of the particle are visualized in Figure 3.6.

Figure 3.6 shows a scanning electron microscopy (SEM) image of a typical ordered macroporous α-alumina particle (*3DOM_3_N2_air*), in which the pore structure ordering at a large scale is visible. Due to the large pores of macroporous material, the grain size of the particles is too thick for transmission electron microscopy (TEM), while SEM does not provide insight in the porosity throughout the particle. By using microtomography and focused ion beam (FIB)-SEM (Nova-NanoLab600), the pore structure throughout the particle was visualized in the bottom right frame. This frame shows a SEM image after a focused ion beam was used to etch away the surface of a *3DOM_3_N2_air* particle, exposing porosity within the particle, throughout the particle. The bottom right frame displays a microtomography of a 400 nm thick slice of a *3DOM_3_N2_air* particle. This thickness was chosen to be able to visualize two stacks of unit

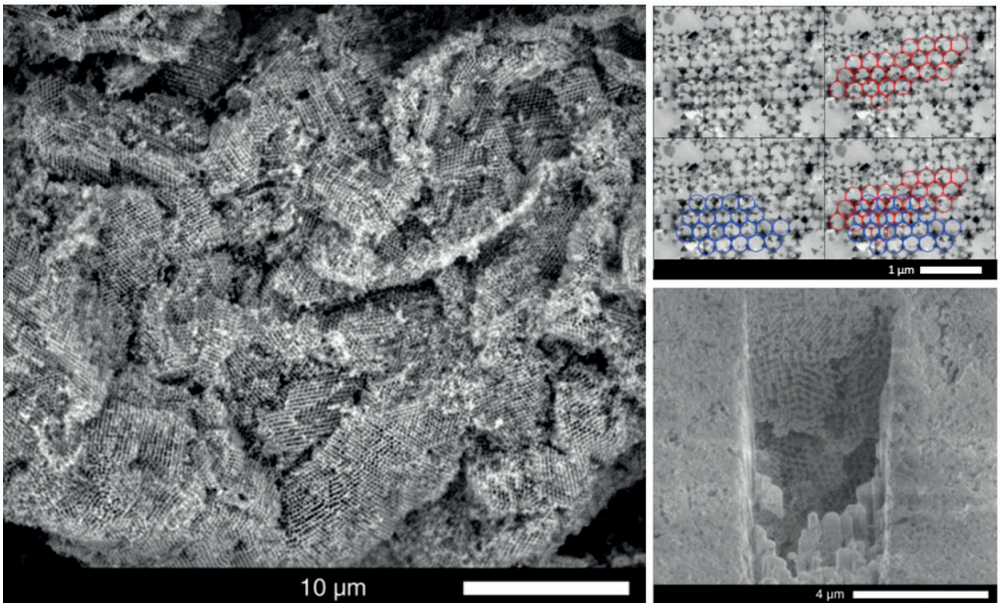

Figure 3.6: SEM image of a typical 3DOM_3_N2_air *particle showing macroporosity extended over the entire particle surface, obtained after heat treatment in nitrogen flow and subsequent heat treatment in air flow (left). TEM micrograph of microtomed* 3DOM_3_N2_air *with a sample thickness of 400 nm obtained from the center of an a-alumina particle. Red and blue circles added to indicate two layers of unit cells (top right). FIB-SEM of* 3DOM_3_N2_air *in which 7.5 µm of the alumina top layer was removed using a focused ion beam. The pore structure is visible throughout the particle (bottom right).*

cells in a single slice. To guide the eye, the slice is shown with a number of cages in a crystal plane denoted by red and blue circles, respectively.

While electron microscopy can illustrate the degree of ordering and how well the desired morphology is maintained, a reliable and statistically relevant method is required to validate these results. Ordering in the macroporous material results in peaks in DR UV/Vis spectra.[231,249,259,263,264] The position of these reflectance peaks reflects the size of the unit cell, the morphology of the ordered structure and the average refractive index of the sample. The latter is determined by the relative amounts of the material (volume fraction), in this case α-alumina, and the liquid or gas in the pores of the structure. The dependencies can be expressed in the Bragg equation. In this equation, the interplanar distance is represented by d_{hkl}, the peak position as λ, the diffraction order as m and the average refractive index as $n_{material,avg}$. The width and intensity of peak is determined by the quality of the ordered structure.

$$D = \frac{m\lambda}{2d_{hkl}n_{material,avg}} \qquad (3.1)$$

In Figure 3.7, the DR UV/Vis spectra of the three 3DOM α-alumina's (*3DOM_1_air*, *3DOM_4_air* and *3DOM_3_N2_air*) are shown. Results from the samples measured in air are shown in the left frame. The positions of the reflectance peaks in this frame in are similar for all three samples. The reflectance peaks of 3DOM_1_air and 3DOM_4_air spectra do not differ visibly, both exhibiting a shallow peak at 500 nm. The spectrum of *3DOM_3_N_2_air* exhibits a sharp

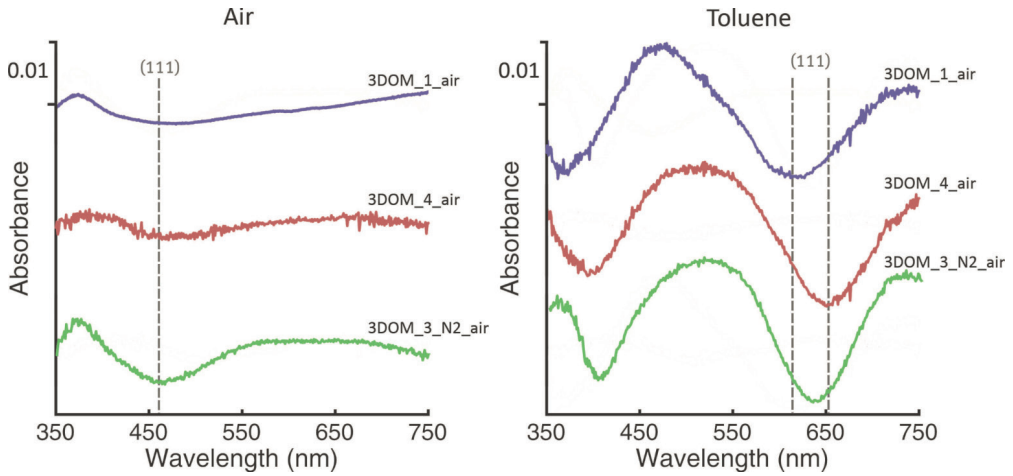

Figure 3.7: Stacked DR UV/Vis spectra of macroporous a-alumina 3DOM_1_air (top, purple), 3DOM_4_air (middle, red) and 3DOM_3_N2_air (bottom, green) in air (left) and toluene (right). A redshift of the reflection minima is observed in toluene due to a change in refractive index.

peak at the same position.

To allow for a better distinction between the spectra of the three samples, especially between the *3DOM_1_air* and *3DOM_4_air* samples, the DR UV/Vis spectra of these samples were also measured after filling the pores with toluene (right frame of Figure 3.7). When the spectrum is measured in toluene, the reflectance peaks are more intense and redshifted, due to the higher density of toluene compared to air and the larger refractive index, respectively. The (111) reflection peaks that were visible when the measurements were performed in air (left frame) are shifted to 600 – 650 nm while additional peaks for (220) reflections appear at 350 – 400 nm, due to this redshift. The redshift in *3DOM_1_air* is less than the shift in the two other materials and similarly, the reflectance peaks of *3DOM_1_air* are clearly less sharp and less intense than the peaks from both *3DOM_4_air* (red) and *3DOM_3_N$_2$_air* (green).

As shown by Blanford *et al.*, from the red shift of the refractive peak, a number of material characteristics can be derived, which together with the full width at half maximum (FWHM) describe the quality of the morphology of the material.[264] These characteristics are summarized for the three 3DOM α-alumina's in Table 3.2. Using the position of the d_{111} reflectance peak in air (n = 1), butanol (n = 1.3991) and toluene (n = 1.4941), the interplanar distance (d_{111}) and the volume fraction of alumina (φ) can be calculated using the linearized Bragg equation (Equation 3.2), while the cage size (D) can in turn be derived from the interplanar distance.[264] In this equation, the d_{hkl} peak position (λ), diffraction order (m), volume fraction solid material (φ) and refractive index of the solid wall (n) are represented. The refractive index of the wall is assumed to be 1.7682, equal to the refractive index of bulk α-alumina.[265]

$$\lambda = \frac{2d_{hkl}}{m}\varphi n_{wall} + \frac{2d_{hkl}}{m}(1-\varphi)n_{solvent} \qquad (3.2)$$

No significant increase in the volume fraction and the cage sizes was observed with increasing

impregnation steps (Table 3.2). Taking into account that with SEM the pore size was measured, but with using DR UV/Vis the calculated size includes the wall thickness (of 35 ± 5 nm), the sizes measured with the different techniques are in good agreement.

Table 3.2: Material characteristics for 3DOM support materials, derived from DR UV/Vis in solvents (air, butanol and toluene) and Equation 3.2.

Sample	3DOM_1_air	3DOM_4 _air	3DOM_3_N2_air[a)]
Volume fraction of alumina, φ	0.18 ± 0.02	0.14 ± 0.01	0.16 ± 0.02
Interplanar spacing, d_{111} [nm]	206	208	211
Calculated cage (+wall) size, D [nm][b)]	252	255	259
FWHM in toluene [cm^{-1}]	3433	2700	2286

[a)] 3DOM_3_N2_air measured in air, butanol, methanol and toluene; [b)] Assuming closed packed arrangement of the pores

Most importantly, the full width at half maximum (FWHM) of the refractive peak is a measure for the degree of ordering of the porosity in the material. A sharp peak is indicative of a better ordered material. The decrease in FWHM with both the amount of impregnation steps and the additional protective carbon coating is striking. This decrease shows that both adjustments result in better ordering compared to the *3DOM_1_air* reference material. The FWHM for *3DOM_3_N_2_air* is even similar to the FWHM of ordered macroporous γ-alumina in methanol described in literature.[264] Hence this suggests that with our new two-step approach α-alumina can be made with a similarly high quality as the γ-alumina of Blanford *et al*, despite the extra phase transformation step.

Having a very high surface area α-alumina support is of particular interest in catalysis, as it is notoriously difficult to obtain such high surface areas by known methods. High surface areas serve to better stabilize the active supported metal particles, even more so if the pore structure is cagelike.[256,266] The preparation strategy proposed in this chapter could be relevant also for other ordered macroporous materials that are difficult to prepare due to phase transitions, such as TiO_2.[160,267]

3.4 Conclusion

We demonstrate a method for the synthesis of high quality, high surface area ordered macroporous α-alumina, based on impregnation with aluminum hydroxide of an ordered polymer template. Multiple impregnating steps contribute to a high degree of pore filling with aluminum hydroxide, increasing the yield of the synthesis and minimizing the loss of ordering. We employed a specific heat treatment in inert atmosphere to convert the polymeric template into a protective carbon coating. Close contact of the protective carbon coating with the alumina surface caused a delay of the alumina phase transitions to higher temperatures and helped to preserve the pore structure. By a final heat treatment in air, the carbon was removed, and high quality ordered macroporous α-alumina with a specific surface area of circa 25 $m^2 g^{-1}$ was obtained. The high quality of the pore structure was evidenced by electron microscopy and quantified by spectroscopic analysis. This material is used to assess the effects of support characteristics on the stability of supported metal particles (chapter 4) and on the selectivity during catalysis (chapter 5).

3.5 Acknowledgments
This research was funded by NWO Vici project 16.130.344. Peter Lipman of Chemical Reactor Engineering, Eindhoven University of Technology is aknowledged for performing mercury intrusion experiments, Marjan Versluijs-Helder and Jochem Wijten of Utrecht University for performing SEM analysis and Mies van Steenbergen of Pharmaceutics, Utrecht University for performing TGA and DLS analysis.

Thermal stability of α-alumina supported silver particles

effects of gas atmosphere and support morphology

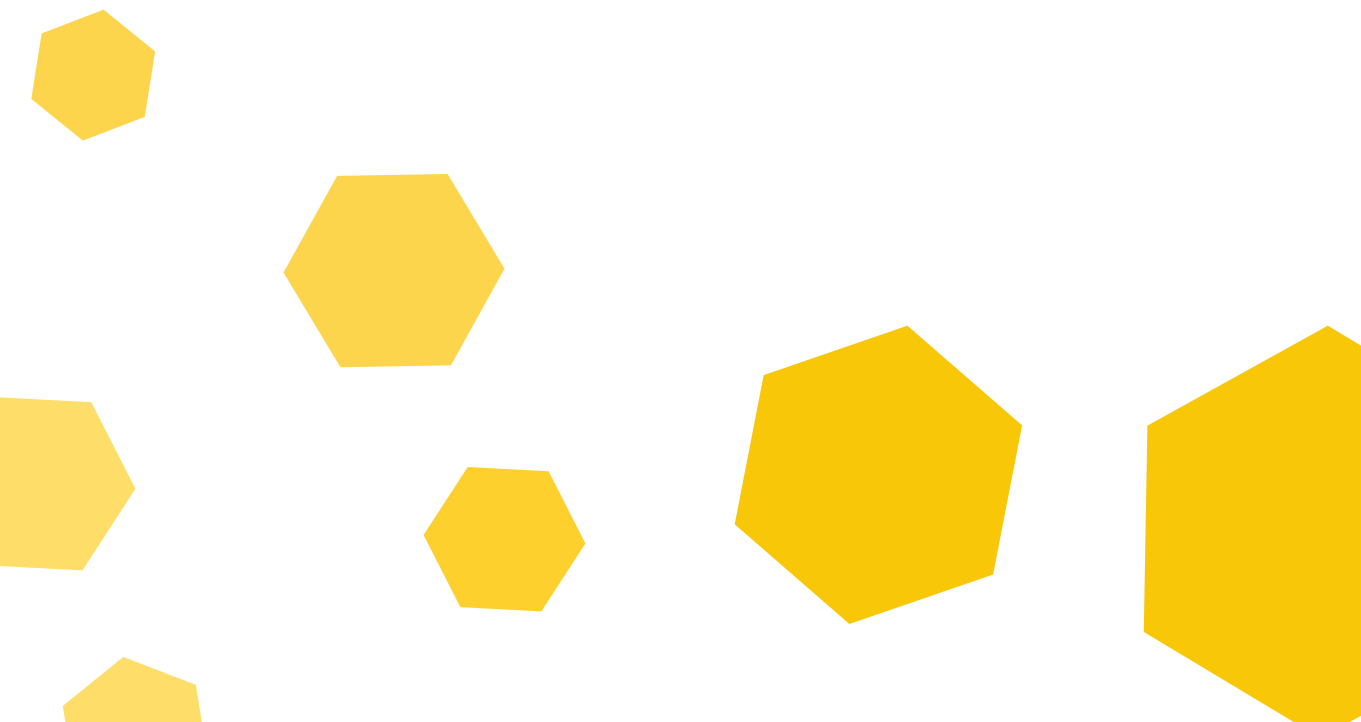

4

Abstract

Stability is an important design parameter for supported silver catalysts, such as those used in ethylene epoxidation, for which silver particle growth is often an important deactivation mechanism. The stability of supported silver particles against growth under reaction conditions was assessed by studying the thermal stability of these samples *i.e.* looking at the particle growth at elevated temperatures. In this chapter, the thermal stability of silver particles in the range of 20 to 135 nm supported on α-alumina with different specific surface areas was investigated in a temperature range from room temperature to 400 °C, and in different atmospheres. Pronounced particle growth was not observed in hydrogen atmosphere, but only in oxygen. This means that oxidized silver species play a key role. No influence of the nature of the support surface or the support morphology was observed, but growth was strongly enhanced by shorter interparticle distances. This is in agreement with either slow diffusion of cationic silver species over the support, or spreading of the metallic silver particles induced by partial oxidation. It is likely that the latter mechanism dominates at low temperatures and short interparticle distances. Importantly, high surface area (3DOM) α-alumina was shown to be an effective support material in preventing particle growth at higher temperatures. Catalysts made with these support materials could be interesting candidates for ethylene epoxidation catalysts with high stability.

4.1 Introduction

4.1.1 Deactivation mechanisms

While according to the definition of a catalyst it is not consumed during the reaction, under reaction conditions the catalytic activity often slowly decreases. The metal particles distributed over the support material are inherently thermodynamically unstable[104] and prone to changes.[160,268–270] Common deactivation mechanisms in catalysis are poisoning, coking or fouling, leaching, attrition, and metal particle growth.[104,160] Poisoning of the catalyst can occur when contaminants are present in the feed or form as byproducts from the reaction. These species strongly bound to the surface of the catalyst, preventing reactants from adsorbing on the active site. These contaminants cannot be removed under reaction conditions and often not even ex-situ.[160,269]

Fouling is the physical deposition of contaminating species onto the catalyst in general; coking is fouling of a catalyst with carbonous material specifically.[160] Coking occurs primarily in dehydrogenation or carbon-coupling reactions, such as naphtha reforming or MTO and Fischer-Tropsch synthesis. In these reactions, unsaturated hydrocarbon chains and/or aromatics are formed, which can undergo subsequent polymerization resulting in carbonous material. This material could remain on the surface of the catalyst, as this carbonous residue does not evaporate or dissolve in the fluid (the fluid medium can be either be liquid or gas depending on the reaction[104]). This coke then blocks the catalyst surface.[104,160,269,270] As opposed to poisoning, coke is not chemisorbed on the catalyst and is therefore relatively easily removed by regeneration of the catalyst.[104,160] Regeneration of a coked catalyst is often done by burning off the carbonous material in an oxidative treatment.[269]

Deactivation by means of metal leaching can also occur during reaction, for example when the feed contains components which stabilize metal atoms through the formation of metal carbonyls or halides, which more easily dissolve or evaporate, like in nickel catalyzed CO methanation.[268,271]Attrition is the mechanical degradation of the catalyst, mainly due to its weight when packed into an industrially sized reactor of high velocities such as in fluid bed reactors. Attrition can play a large role in catalyst deactivation as heterogeneous catalyst bodies are designed to have a high surface area. While this benefits the catalyst performance, this is at the cost of mechanical stability.[161,272] The porous catalyst bodies at the bottom of a packed bed do not have sufficient strength to carry the dynamic load and are slowly ground down to rounded or even powdered material.[10,67,104,160] This leads to a loss of performance, for example, due to reduced accessibility of the active site and/or, increased pressure drop over the reactor.

Deactivation due to metal particle growth occurs *via* the loss of available surface of the active metal when the average particle size increases. Since the reaction occurs at this surface, the loss of active metal surface area usually causes a decrease in activity. In the epoxidation of ethylene, the reaction relevant to this thesis, a combination of deactivation mechanisms is relevant. As the ethylene feed typically originates from petroleum feedstock, the catalyst may undergo poisoning from sulfur-containing species or fouling from other contaminants.[55] In the oxidative atmosphere, coke is readily removed[269,273] and the only side-products formed are acetaldehyde, carbon dioxide, and water, of which acetaldehyde is readily oxidized.[125,129,274,275] Attrition is expected to be less prevalent due to the strong, non-porous support material applied in industrial catalysts.[55,265] Leaching of silver is also expected to be negligible, as silver and silver oxides are not volatile,[56] but redistribution or loss of promotors is expected to significantly influence both the activity

and selectivity of the catalyst.[276] However, in ethylene epoxidation, the increase of the average silver particle size is believed to be an important contribution to deactivation.[112,273,277] Deactivation due to silver particle growth is facilitated by its low melting point, causing mobility at modest temperature[161,202,256,278] further enhanced in the presence of reactants.[112,279–281]

4.1.2 Thermal stability

One mechanism through which average particle growth can occur is particle diffusion and coalescence (PDC). In this mechanism, entire metal particles become mobile and upon two particles meeting, they coalesce to form a single larger particle.[112,279–281] A one-dimensional schematic representation of this mechanism is shown in Figure 4.1A. The driving force for coalescence is the decrease in the overall surface-to-volume ratio and hence decrease the surface energy. For this mechanism, the interparticle distance plays a very important role as the rate of diffusion for these particles is relatively low.[36,282,283] Increasing the interparticle distance by a uniform distribution of the metal particles over support and/or applying a low loading are efficient strategies to reduce the rate of catalyst deactivation through particle diffusion and coalescence.

Alternatively, instead of complete particles, the mobile species can be a metal atom or metal ion stabilized in the form of a complex. These species readily diffuse over the surface of the support material and decompose upon meeting a metal particle. This causes a net diffusion of metal atoms from one particle to another, with large particles growing at the expense of smaller particles.[199,279,284] Such a process is shown in Figure 4.1B (the mobile species are not shown). This mechanism is commonly referred to as Ostwald ripening (OR), which can occur over the catalyst surface or *via* the fluid (gas or liquid). Trapping or encapsulating the active metal within the support material limits the diffusion of the metal particles, as has been shown for copper nanoparticles in mesocellular foam and in nanoreactors.[285–288]

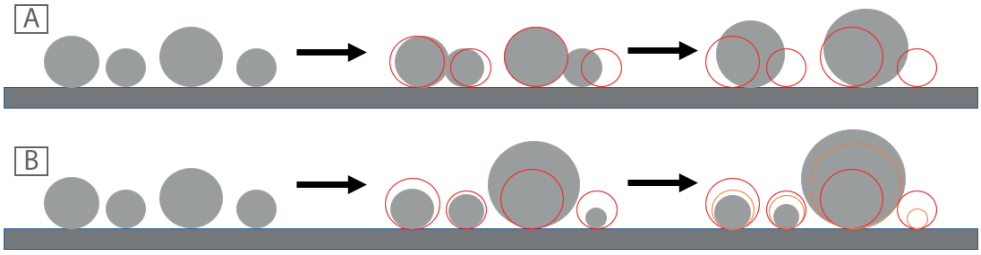

Figure 4.1: Schematic representation of particle size diffusion and coalescence (A) and Ostwald ripening (B). Metal particles are depicted as grey circles that grow via *either mechanism into larger particles; the initial size and position of the metal particles are outline in red.*

In Ostwald ripening, the growth of the average metal particle size is driven by the difference in surface energy contribution between small and large particles. Small particles are less stable than large particles.[279,284] For this reason, the width of the particle size distribution plays a significant role in this mechanism,[281,282,289] such as Pompe *et al.* have recently shown for silica-supported copper catalysts. In their work, a narrow metal particle size distribution led to significantly less particle growth than a wide particle size distribution.[285] At the same time, the interparticle distance, the average distance between metal particles on the support surface, did not significantly influence the growth rate in Ostwald ripening.[224,290] The mobility of the diffusing species may depend on several factors, such as the support material, the strength and abundance of surface species (*e.g.* hydroxyl

groups on oxidic supports[291] or a range of functional groups on carbon supports[161,173]). If the rate-limiting step is the formation or decomposition of the mobile species, and the diffusion is fast (as in the example above mentioned above for Cu nanoparticles), the concentration of mobile species can be considered in dynamic equilibrium (mean-field approximation). However, a dependence on interparticle distance is expected if the diffusion is rate limiting. As the metal particles themselves are not the mobile species in this case, methods that decrease the mobility of the metal particles, such as trapping the metal particles in the support, should not influence the particle growth.

In the case of Ostwald ripening, the support primarily influences the growth rate due to differences in activation energy for the formation and mobility of complexed cations[285,292,293] Masoud *et al.* showed that gold species are more stable against particle growth on titania than on silica or alumina and more stable in hydrogen atmosphere than in oxygen atmosphere.[293] This showed that an oxidizing gas atmosphere is required to create the mobile species. The gold nanoparticles can be assumed to be mostly metallic under both conditions,[11] and therefore no significant difference in growth rate is to be expected in a PDC mechanism. In an OR mechanism, the stability of the diffusing species will be dependent on the gas atmosphere. Under oxidizing conditions, cationic species are formed that are stabilized by surface and/or gas-phase species.[185,294] Under reducing atmosphere no cationic species are formed, and metallic species are less readily stabilized and these are therefore less likely formed.[282] The difference in stability of these reducing and oxidizing atmospheres will influence the formation and/or decomposition rates and is therefore expected to influence the rate of particle growth.

The support influences the growth rate because the diffusing species are more stable on for example titania than on silica, reducing the activation energy for formation, but perhaps also changing the diffusion rate of these same species. Since the formation of these species is related to the rate-limiting step, while the diffusion rate is not, the overall deactivation is facilitated. While in this example the decreased diffusion did not lead to a decreased growth rate, van den Berg *et al.* showed that the particle growth can be decreased by hampering diffusion even when Ostwald ripening is the dominant particle growth mechanism.[291] They showed that when diffusion is significantly reduced, this step can be made the rate-limiting step.

Relevant temperatures for these sintering mechanisms for metal particles of only a few nanometers are the Tamman and Hüttig temperatures,[160,244,295] respectively 0.43 and 0.3 times the absolute melting temperature of the relevant metal.[296] As a rule of thumb, approximately around the Hüttig temperature, atomic species start to form and diffuse over the surface of the metal nanoparticles, while the Tamman temperature relates to the point at which nanoparticles as a whole, with a sizes of a few nanometers or larger become mobile. In general particle growth through Ostwald ripening is expected to start at any temperature where mobile species are formed in appreciable concentration, while the particle diffusion mechanism becomes apparent at the temperature where entire the metal particles become mobile. Both Ostwald ripening, and particle diffusion and coalescence lead to a decrease in the available active metal surface for catalysis and can occur simultaneously.[284,285]

The standard procedure in industry to correct for the gradual loss of activity (due to any deactivation mechanism) is to gradually increase the reaction temperature. This is done to

maintain the product yield and not disrupt downstream processes although often at the expense of selectivity.[72,273,297] It is therefore important to understand the thermal deactivation, primarily sintering of metal particles. Deactivation due to sintering has been investigated *via* ex-situ thermal deactivation studies.[202,278,293,296] In these studies, the conditions (for instance temperature) at which particle growth was observed did differ significantly from those during the actual reaction. Under reaction conditions, the concentration of potentially complexing ligands is different than in ex-situ experiments, as well as effective coverages at the metal catalyst surface. However, obtaining insight *via* ex-situ experiments into the trends in particle growth and the influence of the most important parameters is relevant.

4.1.3 Ethylene epoxidation

Silver is the sole metal commercially used as a catalyst for the partial oxidation of ethylene to ethylene oxide. It is a mild oxidation catalyst, capable of selectively oxidizing the ethylene into ethylene oxide, instead of fully oxidizing ethylene to carbon dioxide and water.[125] The silver catalyst exhibits particle size effects, small particles have a low surface-specific activity, which increases with particle size up to a size of circa 60 nm. Silver particles larger than this critical size have a constant turn over frequency, as discussed more extensively in Chapter 2.[132,133] Van Hoof *et al.* even reported increasing turn-over frequencies with increasing silver particle size.[298] For this reason, particle sizes in the range of 100 – 1000 nm are common in industrial catalysts.[77,78] Low surface area support materials, such as α-alumina, are favored over high surface area support materials containing micro- and mesopores, since unwanted silver particles below 50 nm could form inside these micro- and mesopores, and more importantly due to the detrimental role of the support on the selectivity of the catalyst, such as shown in Chapter 5.

The three-dimensionally ordered macroporous (3DOM) α-alumina described in Chapter 3 is an interesting support for the ethylene epoxidation catalyst and several other catalysts.[179,243,248,299] Its macroporosity and unique morphology compared to commercial α-alumina materials facilitate large silver particles and allows us to study in more detail the influence of support morphology. The role of this macroporosity, and potentially other material characteristics in which 3DOM may differ from commercial α-alumina, on the thermal stability of the supported silver particles is reported in this chapter. We are interested in comparing catalysts supported on 3DOM α-alumina support to catalysts on supports with lower surface area (1 and 8 $m^2 g^{-1}$ will be used), such as the ones used in the epoxidation reaction.[55,77,78]

For the thermal stability of supported particles in these types of catalysts, six different parameters are believed to play a relevant role.[104,224,278,283,300–305] First, the effect of the gas atmosphere, either oxidizing or reducing.[278,293,301] Second, the initial metal particle size[300] and third, the width of the particle size distribution.[281,282,284,289] Fourth, the interparticle distance of the metal particles dispersed over the support.[224,278,283] Fifth, the characteristics of the support surface can be crucial for particle mobility.[112,303,304] This can be due to differences in (surface) composition,[304] crystal phase (of the termination layer)[299] or surface curvature.[305] Sixth, the support morphology, which is known to be able to confine mobile species when the particle growth occurs *via* particle diffusion and coalescence, but not when Ostwald ripening is the primary mechanism.[104,224,302] We attempt to separate the contribution of different effects by looking at the individual parameters.

In this chapter, we describe the effect of support specific surface area and morphology on

the stability of supported silver particles. The relevant supports in this chapter are a standard non-porous support material, a (relatively) high surface area, non-porous support material and a very high surface area support material containing ordered macropores (3DOM). The growth of the silver particles was followed during heating as a function of the gas atmosphere, the initial silver particle size, average interparticle distance and support. The effects of the width of the particle size distribution were not investigated, as we did not have a reliable means to independently control the width of the particle distribution. To exclude the effect of the promotor on the stability of the metal particles, the promotor species were omitted from the experiments described in this chapter.

4.2 Methods

4.2.1 Support materials

Polymethylmethacrylate (PMMA) template material for the synthesis of 3DOM α-alumina was obtained using the procedure described in chapter 3.[306] Specifically, this template was obtained by using the surfactant-free emulsion polymerization of methyl methacrylate (MMA, 99%, up to 30 ppm 4-methoxy phenol inhibitor, Sigma-Aldrich) in water. The monomer, 100 mL MMA, and 400 mL demineralized water in a 1 L round bottom flask were stirred using an overhead stirrer with 450 rpm at room temperature.[249,250] The emulsion was heated to 70 °C and nitrogen were bubbled through the dispersion for at least 30 minutes to remove dissolved oxygen from the dispersion and to deactivate the inhibitor. Thereafter, 69 mg potassium persulfate (KPS, initiator) was added, resulting in a 0.5 mM concentration. The emulsion was left to react for 3 hours at 70 °C after which a white dispersion had formed.

The dispersion was allowed to cool down to room temperature and was filtered to remove larger chunks of polymer. The filtrate was centrifuged for 1 hour at 3000 rpm during which a white solid precipitated. The clear supernatant was decanted and the obtained white powder was left to dry for several days at room temperature in air after which it was crushed into a powder.

Three dimensional ordered macroporous (3DOM) materials were obtained by an impregnation of the dry PMMA colloidal crystal powder as a template material.[249,251,306] Of the template powder, 1.5 g was placed in a Buchner funnel and drop-wise and approximately 3 mL solution of 1 M aluminum nitrate nonahydrate in demineralized water/methanol (1:1 volume ratio) was added to completely wet the template. After 2 minutes of soaking, the excess solution was removed by applying vacuum for 20 minutes to obtain a dry powder. Subsequently, the powder was wetted with ammonia (28-30%)/methanol (1:1 volume ratio) to form aluminum hydroxide in the pores of the template. The excess solution was removed via vacuum suction and the powder was dried for 20 minutes under dynamic vacuum at room temperature. To obtain complete filling of the pores, these steps were performed a total of three times before drying the powder overnight at room temperature.[249,251] The dried powder was heat-treated at 1150 °C under a nitrogen flow of at least 0.5 L min^{-1} for 6 hours after a 5 °C min^{-1} heating ramp. A second heat treatment in a flow of air of at least 0.5 L min^{-1} at 1150 °C for 6 hours after a 5 °C min^{-1} heating ramp was used to obtain α-alumina and remove pyrolyzed PMMA.[249,251]

4.2.2 Silver deposition

The support material described above was loaded with silver particles by incipient wetness impregnation. Next to the self-prepared α-alumina (3DOM_3_N2_air and 3DOM_1_air),

commercial α-alumina from BASF (8 $m^2 g^{-1}$, Al-4196E) and Sigma-Aldrich (1 $m^2 g^{-1}$, 100 mesh) were used as support materials after they were crushed and sieved to a 38 - 90 μm sieve fraction. The silver precursor, silver oxalate, was freshly prepared following a similar procedure as described by Pourmortazavi *et al.*[200] An aqueous solution of oxalate dihydrate (99.5%, Merck) and an aqueous solution of silver nitrate (99+%, Sigma-Aldrich) were mixed in a molar ratio of 1:2. Silver oxalate precipitated, was washed three times with water, and dried in an oven in static air at 60 °C overnight. The precursor solution was prepared by dissolving this silver oxalate in a mixture of ethylenediamine (*en*, 99%, Sigma-Aldrich) and H_2O (ratio: H_2O/*en* = 0.73 vol%). Before the impregnation, the support materials were dried for 2 hours under dynamic vacuum at circa 150 °C. The impregnated materials were dried overnight at 60°C in static air and heated with 5 °C/min under hydrogen, oxygen or inert gas atmosphere and kept for 2 hours at temperatures ranging from 215 to 300 °C. The gas atmosphere and treatment temperature were chosen to result in the desired average silver particle size, based on work described in chapter 2.[212] Two 3DOM supported samples were crushed under 230 MPa in a press to crush the 3DOM structure while maintaining the support specific surface area. The loss of ordered structure was confirmed by SEM and TEM (Image is not shown).

*Table 4.1: Silver containing samples prepared using different support materials and silver loadings. The silver particle size is tuned by varying the heat treatment procedure. The samples are named AgNP*SSA_wt%_dp *or Ag3DOM*_wt%_dp *with* SSA *being the specific surface area,* wt% *the nominal solver weight loading and silver particle size (*dp) is *the surface averaged particle size.* NP *or* 3DOM *relates to either non-porous or 3DOM support such as discussed in chapter 3. Distinction between two different batches AgNP8_15_40 is made by a suffix* a *or* b. *The suffix* crushed *is applied for the 3DOM based support that is crushed to destroy the cage structure.*

	Support		Silver		
Sample	Surface area (m^2/g)	Structure	Silver loading (wt%)	Silver particle size (nm)	PDI*
AgNP1_1_45	1	Non-porous	1	45	0.1
AgNP1_15_60	1	Non-porous	15	60	0.06
AgNP1_15_100	1	Non-porous	15	100	0.05
AgNP8_5_45	8	Non-porous	5	45	0.06
AgNP8_15_20	8	Non-porous	15	20	0.20
AgNP8_15_40_a	8	Non-porous	15	40	0.05
AgNP8_15_40_b	8	Non-porous	15	40	0.05
AgNP8_15_60	8	Non-porous	15	60	0.7
Ag3DOM_15_45	20	3DOM	15	45	-
Ag3DOM_15_60	20	3DOM	15	60	-
Ag3DOM_15_60_crushed	20	Crushed	15	60	-
Ag3DOM_31_135	20	3DOM	31	135	-
Ag3DOM_31_135_crushed	20	Crushed	31	135	-
Ag3DOM_15_100	20	3DOM	15	100	-

* *PDI is the abbreviation for polydispersity index, a measure for the particle size distribution; the squared ratio between the standard deviation in the particle size distribution and the average particle size.*

4.2.3 Structural characterization

The size of the colloids in the PMMA suspension was analyzed using dynamic light scattering (DLS) on an ALV/CGS3 system obtaining the average hydrodynamic volume of the PMMA spheres. The morphology of drop-casted PMMA latex, colloid crystal powder, and 3DOM powders was analyzed using scanning electron microscopy (SEM) with a FEI XL30 FEG SEM. The micrographs were processed using iTEM Soft Imaging System software.[204]

Diffuse-Reflectance UV/Vis spectra of the PMMA colloidal crystal powder, 3DOM materials, and the supported silver samples were obtained using a Varian CARY 500 Scan UV/Vis-NIR spectrophotometer with an integrating sphere detector. In a typical analysis of the 3DOM materials and the supported silver samples, 30 mg of analyte was diluted with 600 mg pristine α-Al_2O_3 (1 m^2 g^{-1}, 100 mesh, Sigma-Aldrich) and ground into a fine powder before taking a spectrum of the 200 – 1000 nm range. A background measurement of pristine α-Al_2O_3 was performed, and the background spectrum was subtracted from the experimental spectra.

Crystal phase analysis was performed by X-Ray Diffraction (XRD) on a Bruker D8 Phaser diffractometer equipped with a Co K_α source (λ = 0.1789 nm) using an angle range from 20° to 90° in 2θ and comparing XRD diffractograms with the PDF-4+ 2016 database.

The weight loss during heat treatment was analyzed using thermal gravimetric analysis (TGA) performed in a Perkin Elmer Pyris 1 TGA under a 10 mL min^{-1} flow of 20% oxygen in nitrogen. For these experiments, the temperature was increased from 50 °C to 500 °C with a heating ramp of 5 °C min^{-1}. The decomposition products were analyzed using a Pfeiffer Vacuum OmniStar mass spectrometer.

Nitrogen physisorption isotherms were measured at −196 °C on a Micromeritics TriStar 3000 apparatus. The specific surface area of the support was calculated using the BET equation ($0.05 < p/p^0 < 0.25$). Mercury porosimetry was performed using Micromeritics AutoPore IV 9500 at Eindhoven University of Technology in the Chemical Reactor Engineering group. Pore volume data were calculated over the range 0.0007 – 227.5270 MPa. The contact angle between the support materials and the mercury was assumed to be 130° and the values for the mercury surface tension and density were set to 485 dynes/cm and 13.5335 g/cm^3, respectively.

4.2.4 Thermal stability measurements

Ex-situ thermal stability measurements were performed by heating 10 to 50 mg of supported silver catalyst in a U-shaped reactor in a 20 vol% hydrogen or oxygen in nitrogen atmosphere at 1 bar with a gas hourly space velocity of 60,000 hr^{-1}. The sample was heated from room temperature to 100, 200, 300 or 400 °C with a 5 °C min^{-1} heating ramp. Immediately after reaching this temperature, the sample was removed from the oven and allowed to cool down in the respective gas atmosphere. The average silver particle sizes before and after heat treatment were determined using DR UV/Vis spectroscopy and SEM.

4.3 Results and discussion

4.3.1 Alumina supports

The samples discussed in this chapter were supported on three different types of support materials. The commercial support materials are distinguished by their specific surface area of

1 $m^2 g^{-1}$ (Frames 4.2A and 4.2D) and 8 $m^2 g^{-1}$ (Frames 4.2B and 4.2E). Porous 3DOM α-alumina has a higher surface area of approximately 20 m^2g^{-1} and is shown (Frames 4.2C and 4.2F). A 'fourth' type of samples was obtained from crushing the pore structure of 3DOM support of silver containing samples and is not shown. The top row of Figure 4.2 shows the SEM images of these materials, while the bottom row of frames shows the corresponding XRD diffractograms.

In the top left image (A), large chunks are visible with smaller crystallites that decorate the surface, but the bulk of the material is present in the large particles. The large particles have flat surfaces and relatively sharp edges, indicative of large crystallites. The size of the particles exceeds several micrometers. In the middle image (B), the 8 m^2/g support exhibits more spherical and rounded features of a size of approximately 100 to 500 nm which are interconnected. In the right frame (C), regular features that are arranged in a hexagonal lattice are observed. This repeating feature is a cage with interconnecting windows to the nearby cages as described in Chapter 3.

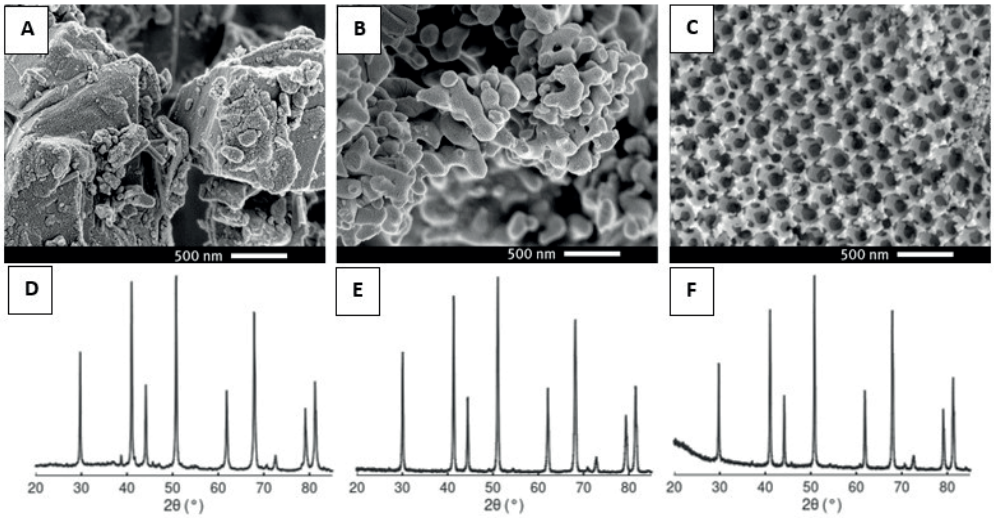

Figure 4.2: SEM images of 1 $m^2 g^{-1}$, 8 $m^2 g^{-1}$ (A, B and C respectively) and 3DOM α-alumina support materials with the corresponding XRD diffractograms shown below them (D, E and F).

For all three types of support material, the XRD diffractograms show sharp peaks that are representative of α-alumina. The narrow peaks in all three diffractograms indicate a high degree of crystallinity and large crystallite sizes, beyond the range in which the Scherrer's equation could be reliably used the determine the average crystallite size.[307] The width of the peaks in the diffractograms is therefore primarily determined by the instrumental broadening. The base-line in the XRD of the non-porous supports (Frame 4.2D and 4.2E) is flat, indicating the absence of amorphous components. In the diffractogram of the 3DOM support the baseline at low degrees 2θ is elevated. While such a baseline feature could be indicative of the presence of amorphous materials, in this case, the feature is an artifact caused by the sample holder. This is verified by blank measurements of the holder and measurements with different holders. This artifact is only visible in this sample as the synthesis yield was low, and hence there is not enough material to completely fill the holder. Besides this artifact, the baseline of the diffractogram in Frame 2F does not differ significantly from Frames 4.2D and 4.2E.

4.3.2 Silver deposition

The support materials were impregnated with a solution of a silver salt, subsequently, the samples were dried and the silver salt was decomposed by heat treatment. The size of the resulting silver particles was tuned by varying the gas atmosphere and temperature in the heat treatment step. This procedure is more extensively discussed in Chapter 2.[212] While the combination of high silver loading and low specific surface area supports typically leads to relatively large silver particles, their size was varied to a certain extent: when the heat treatment was performed in hydrogen atmosphere the resulting particles were much smaller than when the treatment was performed in oxidative atmosphere. Similarly, low-temperature treatment yielded smaller particles than high-temperature treatment. By a combination of these strategies, similar average silver particle sizes were obtained on all three supports without changing the silver weight loading, as can be seen in Table 4.1. For example, for catalysts with a weight loading of 15 wt% silver supported on 8 m^2 g^{-1} α-alumina, the particle size on different samples could be tuned in a range of 20 to 60 nm.

In Frame 4.3A the UV/Vis spectrum of *AgNP1_1_45* is shown as an example of a typical UV/Vis spectrum for supported silver particles large enough to exhibit surface plasmon resonance.[39,208,209] The spectrum was baseline corrected by subtracting the UV/Vis spectrum of pristine α-alumina. This removes the sharp alumina absorption peak at 265 nm present in all three support materials.[308] The surface plasmon resonance of the silver particles resulted in a peak at circa 450 nm, shifting to higher wavelengths for larger particles. The exact peak shape and position depending on the size and shape of the silver particles.[212,309,310] We used the peak position as a measure for the average particle size. 3DOM α-alumina itself exhibits a relatively weak scattering peak at 460 nm, but due to the relatively low intensity,[306] we neglect this contribution in the estimation of the silver particle size via UV/Vis.[212]

In the middle frame (B) the SEM image of *AgNP1_1_45* shows bright white, round silver particles deposited on light grey α-alumina. Similar micrographs were used to determine the particle size distribution (from at least 300 particles on 5 different images from a sample) shown in frame C of Figure 4.3. The surface averaged particle size was determined using these observations and reported as the particle size in Table 4.1, this particle size was in good agreement with the average particle size obtained from UV/Vis. The particle size distribution was reasonably narrow. The particle size distributions for the other samples used in this chapter were similar, with a polydispersity index (measure for width of the particle size distribution further described in the Methods section and Chapter 3) ranging from 0.04 to 0.1 for samples with an average silver particle size of 40 nm or higher indicating a narrower particle size distribution than shown in Frame 4.3C. These polydispersity indices for these samples are the same as or lower than the PDI related to Frame 4.3C.

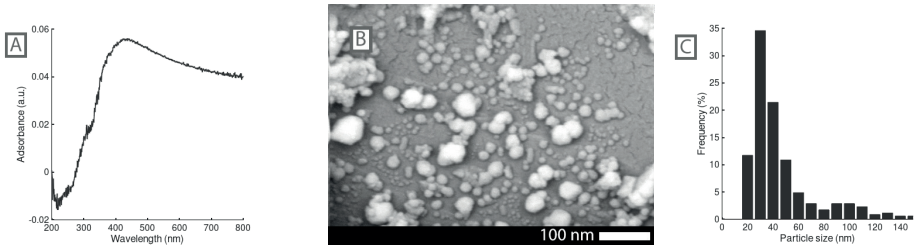

Figure 4.3: UV/Vis spectrum of sample AgNP1_1_45, *showing the surface plasmon resonance of silver particles at circa 450 nm, SEM image of silver (white spheres) particles on 1 m^2 g^{-1} a-alumina (grey areas) and the silver particle size distribution thereof.*

4.3.3 Thermal stability of supported silver particles in oxidative and reducing atmosphere

The average silver particle size of a series of samples was determined before and after heat treatment at different temperatures. Due to the relatively large size of the silver crystallites, an accurate determination of the silver crystallite size with XRD is not possible. Therefore, SEM and UV/Vis spectroscopy were used. The position and intensity of the Ag surface plasmon resonance peaks in UV/Vis spectroscopy can be correlated to a surface-averaged silver particle size, while the SEM yields a number-averaged silver particle size which is mathematically converted to a surface-averaged particle size for further comparison. This calculation was based on the full particle size distribution (rather than just the average particle size) and assuming spherical particles. UV/Vis provides quick and straightforward bulk analysis of the average silver particle size in general[212] and a method to determine the average silver particle size in 3DOM materials specifically. Due to the morphology of the 3DOM materials electron microscopy cannot be used, as representative 3DOM particles are too large for transmission electron microscopy without microtomy, and SEM is unable to probe the particles inside the porous material.

Figure 4.4 shows the particle size distributions for *AgNP8_15_40a* obtained from SEM for samples before and after heating to 200 °C or 400 °C in either hydrogen (4.4A) or oxygen atmosphere (4.4B). Frame 4.4C shows the evolution of the average silver particle sizes measured using UV/Vis spectroscopy and SEM. A good agreement between the results of the two characterization techniques is observed. The temperature at which particle growth becomes apparent is circa 100 °C, at lower temperatures the growth does not occur or is limited. A line was added to these datasets to guide the eye.

For the construction of the line-to-guide-the-eye in Frame 4.4C we used an empirical model to adequately describe the data rather than a fundamental physical model and attempt to describe the mechanism. For this, Equation 4.1 was used as it can approach the apparent decrease in growth rate at high temperatures (Frame 4.4C) without adding too much complexity.

$$d_p = \frac{a}{T^3} \exp\left(\frac{-b}{T}\right) \qquad (4.1)$$

The average interparticle distance for the silver particles on the fresh sample (defined as the average distance between the surfaces of two particles) is 115 nm based on the volume-averaged particle size, while it increases to 380 nm in O_2 at 400 °C. This distance is calculated assuming a

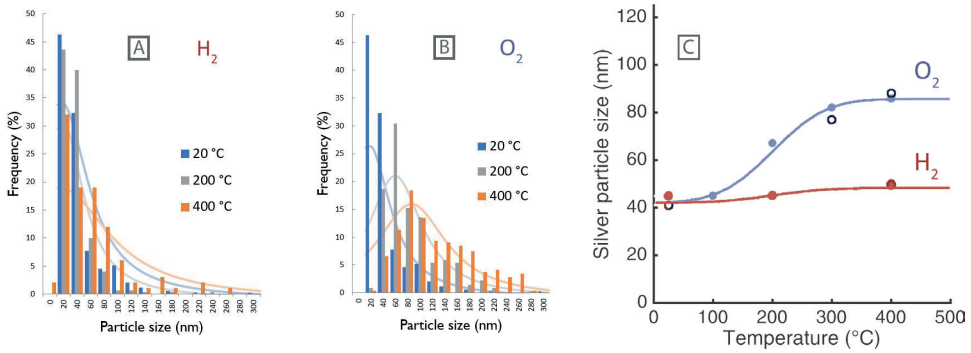

*Figure 4.4: Silver particle size of α-alumina supported samples at different temperatures (lines added to guide the eye). The effect of gas atmosphere for 15 wt% silver on 8 $m^2 g^{-1}$ α-alumina (BASF) (*AgNP8_15_40a*). Average silver particle sizes were determined with SEM (open symbols) and DR UV/Vis spectroscopy (closed symbols).*

uniform distribution of the silver particles over the support surface, and assuming that all silver particles have a size equal to the (surface) averaged particle size obtained with SEM and using the nominal silver weight loading (15 wt%) and the support specific surface area (8 $m^2 g^{-1}$). This distance is the average net distance a mobile species needs to diffuse to facilitate growth. However, considering a polydisperse particle size distribution and a non-ideal distribution of these particles over the support material, in the first stage growth can occur also at smaller net distances, while during growth the interparticle distances increases. The average interparticle distance between silver particles supported on a catalyst body is a valuable tool to compare particle growth rates over similar samples and to estimate the order of magnitude thereof.

The silver particles are expected to be metallic under these conditions, as is confirmed by XRD on similar samples (see chapter 2).[212] This is true for samples before heat treatment and for samples heat-treated under reducing and oxidizing atmospheres related to the low stability of silver oxide. Please note that both silver (I) oxide and silver (I,III) oxide decompose at low temperatures *i.e.* decomposition starts around 200 °C,[311] and between 100 and 200 °C respectively. Small particles of silver oxide[144,312] or surface oxides[131,313] may still be formed and be stable up to higher temperatures, but the bulk particles will be largely metallic for the duration of the experiment.

As both the particle size distribution (Frame 4.4A) and the size evolution (Frame 4.4C) show, almost no particle growth of the silver nanoparticles was observed in a hydrogen atmosphere, while a clear particle growth was observed in oxygen from about 100 °C onwards. The lack of growth of supported nanoparticle in reducing atmospheres compared to oxidizing atmospheres is more often observed [271,279,282,292] and means that for metal mobility oxidized metal species are necessary. The most obvious conclusion is that the observed silver particle growth is dominated by Ostwald ripening in which the mobile species consist of cationic silver species. However, the formation of silver oxide species on the alumina support might also facilitate spreading of the silver particles.[314] Deformation and spreading of the silver over the support might allow the silver particles to come in contact with each other and coalesce without the need to diffuse over appreciable distances. For example, a particle with a contact angle of 90° has a diameter more than twice as small as a particle with the same volume but a contact angle of 45° and 4.3 times as small as a particle with a contact angle of 25°).

In a hydrogen atmosphere no oxidized species are formed and the growth of silver particles most likely occurs via particle diffusion and coalescence. As shown in Figure 4.4C, these conditions do not lead to significant particle growth, which might be explained by the fact that the silver particles are too large to diffuse over large distances. For example, as shown by Harris[282], Chu *et al.* and Wynblatt,[281] particles of 20 nm or more, can typically be considered immobile even at elevated temperatures, while small particles showed significant mobility.[10,18] Harris shows this for platinum particles supported on transitional aluminas at 600 °C, which differs significantly from the silver on α-alumina samples in this chapter. Silver has a significantly lower melting point than platinum and is (therefore) significantly more mobile. We estimated the particle growth relative to the platinum samples discussed by Harris. According to their paper, the diffusion coefficient of the metal particles decays exponentially with the size of the mobile species (in this case silver particles of circa 40 nm), while, for a random walk, we can approximate the diffusion rate scales with the root of the temperature (if we equate the diffusion as thermal energy being converted to kinetic energy). At the same time, the Tamman temperature is defined as the temperature at which bulk diffusion becomes apparent.[296] This means the mobility of the particle is becoming significant at this temperature.[295] The Tamman temperature for silver and platinum are 260 and 605 °C respectively,[315] therefore the diffusion coefficient can be considered to be in the same order of magnitude for silver at 260 °C as platinum at 600 °C for particles with the same size and on the same type of support. Given that the α-alumina support is relatively inert,[167,184] the diffusion of either material on α-alumina is expected to be slower than on transitional aluminas. Besides this, the average particle size for *AgNP8_15_40a* and *AgNP8_15_40b* is 40 nm, eight times larger than the particle size described by Harris (as diffusion scales with volume, not the diameter of the particle, $\frac{V_{40\,nm}}{V_{40\,nm}} = \left(\frac{d_{40\,nm}}{d_{40\,nm}}\right)^3$). We believe it is therefore safe to consider that the particle diffusion is within the same order of magnitude as the particle diffusion observed by Harris. Hence silver particles of several tens of nanometers can be considered immobile; a distance travelled by 20 nm particles during the course of a 1 hour experiment due to particle diffusion according to Harris would be approximately the size of their own diameter, which would not be sufficient to exceed the observed interparticle distances and facilitate significant growth in our samples. Without any other mechanism in place, just diffusion of metallic silver particles followed by coalescence is therefore unlikely to lead to significant particle growth for the samples and temperatures described in this chapter.

Since the growth of silver particles under oxidative atmosphere primarily relevant for the epoxidation reactions discussed in this thesis, further analysis is performed under oxygen atmosphere. Average silver particle sizes obtained by SEM are omitted from the further figures for clarity.

4.3.4 Effect of initial silver particle size on the thermal stability of supported silver particles

In Frame 4.5A, the evolution of the silver particle size for samples with different initial silver particle sizes is shown. The metal loading is the same for all samples (15 wt%) as well as the support specific surface area (20 $m^2\ g^{-1}$) and morphology. Lines are added to guide the eye. Growth started between 100 and 200 °C while the particle size at 400 °C is roughly 40-50 nm larger than the initial particle size. For none of the samples in this chapter, any growth is observed at 100 °C, suggesting an onset temperature rather than a smooth exponential increase

which may be related to the formation of mobile species required for particle growth.

In Frame 4.5B the evolution of the particle size from the left frame is shown as an Arrhenius plot of the logarithm of the average particle volume versus inverse temperature. The lines were fitted excluding the data points obtained at room temperature as these deviated significantly from lines through other datapoints. This is again an indication of the presence of an onset temperature. The apparent activation energy for particle growth above 100 ˚C is very similar for all samples (15.7, 15.1 and 13.7 kJ/mol for *AgNP8_15_20, AgNP8_15_40,* and *AgNP8_15_60* respectively). The low activation energy for particle growth for all investigated particle sizes means that the growth is barely temperature activated.

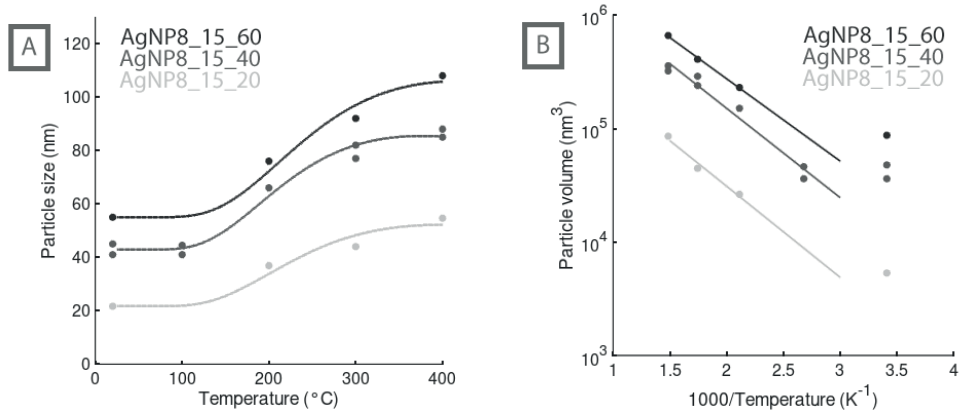

*Figure 4.5: The effect of initial silver particle size for 15 wt% silver on 8 m^2 g^{-1} α-alumina (BASF) supports. This shows the silver particle size of a-alumina supported samples (*AgNP8_15_20*, *AgNP8_15_40*, and* AgNP8_15_60*) at different temperatures (lines added to guide the eye). A duplo measurement of* AgNP8_15_40 *is included to show reproducibility (A). Arrhenius-type plot of the same data sets with calculated particle volume based on the observed diameter (B). Average silver particle sizes were determined with SEM and DR UV/Vis spectroscopy, average silver particle sizes obtained by UV/Vis spectroscopy are omitted for clarity.*

A slight decrease in particle growth with increasing initial particle size can be seen in Figure 4.5 can be the particle size, but this is not a large contributor in the size range discussed in this chapter. Such a particle size dependence could be explained due to a loss of metal surface area, decreasing the probability of both formation and decomposition of mobile species.[284,290] However, regardless of initial particle size, all three catalysts show a similar absolute increase in particle size, *i.e.* from 40 to 50 nm for initial sizes of 20 to 60 nm respectively. This justifies that we neglected the effects of the initial silver particle size on the growth rate in the further discussion of the samples presented in this chapter.

Due to the exponential dependence of the particle growth rate on the temperature and the low activation energy, some particle growth is expected to have occurred at 100 °C. However, all the samples in this chapter are exposed to at least 215 °C during their synthesis procedure, which may have caused the least stable particles, which would facilitate growth at low temperatures i.e. < 100 °C, to have already sintered during the sample preparation. For the samples prepared in

hydrogen atmosphere this does not have to be the case, but for these samples (*AgNP1_1_45* and *AgNP8_15_20*) insufficient data (a single data point shown in Frame 4.7A) at these low temperatures was collected to make this differentiation.

Concluding, an oxidizing atmosphere is required for particle growth, which shows that cationic silver species are crucial in inducing mobility in the system. It is known from literature that cationic silver species readily spread on oxidic supports.[185,316–318] It might be that these oxidic silver species are the mobile species responsible for Ostwald ripening. In this case the rate limiting factor for particle growth might be the formation on and/or escape of the mobile species from the silver particle surface, the decomposition of the mobile species upon meeting a (larger) silver particle or the diffusion rate over the support. In the first two cases the interparticle distance is not expected to have a large influence on stability, while in the latter case it should play an important role. If silver oxide facilitates the spreading of silver nanoparticles over the support, and hence induces particle growth by spreading and coalescence, the interparticle distance is expected to have a large influence on particle growth. Hence the influence of support morphology and interparticle distances will be discussed in more detail in the next paragraph.

4.3.5 Effect of the support

Figure 4.6 shows the effect of the support specific surface area on the thermal stability for a series of samples with the same Ag weight loading. The samples shown in this figure are supported on four different supports, with two commercial supports (1 and 8 $m^2 g^{-1}$) and two high surface α-aluminas. The average interparticle distance is 33 and 175 nm for the 1 and 8 $m^2 g^{-1}$ commercial α-aluminas respectively and 355 nm for both high surface area materials. Of the two high surface α-alumina materials shown, the first is a 3DOM α-alumina, and the second the crushed equivalent of the same 3DOM material. This was crushed after impregnation and calcination to remove the ordered structure of the material, and hence the well-defined 100 nm windows that could be obstacles for silver particle movement, while the surface area did not significantly change. Note that the y-axis in Figure 4.6 is extended to go up to 250 nm to be able to visualize the average silver particle size of 15 wt% Ag on 1 $m^2 g^{-1}$ α-alumina (*AgNP1_15_60*) after heating to 400 °C. There is a clear trend of increased Ag particle growth with lower support surface area/smaller interparticle distance; the high surface area 3DOM alumina supported samples clearly show the highest thermal stability.

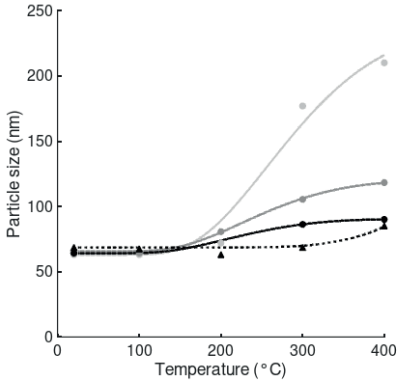

Figure 4.6: The effect of support specific surface area for all 15 wt% silver on a-alumina supports. This shows the silver particle size of a-alumina supported samples at different temperatures (lines added to guide the eye)

for samples supported on 1 m^2 g^{-1} a-alumina (Sigma-Aldrich, light grey), 8 m^2 g^{-1} a-alumina (BASF, dark grey) and 3DOM (black), and for crushed 3DOM samples (respectively AgNP1_15_60*,* AgNP8_15_60*,* Ag3DOM_15_60 *and* Ag3DOM_15_60_crushed *(triangles and dashed line)). Average silver particle sizes were determined with SEM and DR UV/Vis spectroscopy, but average silver particle sizes obtained by UV/Vis spectroscopy for* AgNP1_15_60 *and* AgNP8_15_60 *and obtained by SEM for* Ag3DOM_15_60 *and* Ag3DOM_15_60_crushed *are omitted for clarity.*

From these results it cannot directly be derived whether it is the nature of the support surface, or the interparticle distance (which differs an order of magnitude between the lowest and highest surface area materials (33 versus 355 nm)) that causes these striking differences in stability. The different morphologies and/or chemical nature of the surface of the different support materials could have an influence, although this is unlikely as all three materials are α-alumina,[292,300,319]. Nevertheless to exclude this explanation, another series of test was performed (Frame 4.7A) for three samples with similar initial particle size (45 nm), silver surface density (50 at_{Ag} nm^{-2}) and average interparticle distance (230 nm) on three different support materials (PDI of *AgNP1_1_45* and *AgNP8_5_45* are 0.05 and 0.06 respectively. For *Ag3DOM_15_45* the average silver particle size could only be determined with UV/Vis and no PDI could be derived). These samples, therefore, differ primarily in their support morphology such as shown in the SEM imaging in Figure 4.1, but all have the same interparticle distances.

The size of the silver particles (<80 nm) is smaller than the window size of 3DOM (100 nm) for the samples in Frame 4.7A, so the support morphology is not expected to directly influence the thermal stability. In the frame on the right, the initial average silver particle size is slightly larger than the windows of the 3DOM morphology. This was achieved by increasing the silver weight loading to 15 wt% on 3DOM α-alumina. Also, in that case, the silver surface density (125 at_{Ag} nm^{-2}) and average interparticle distance (640 nm) are similar for both samples. The increase of the weight loading is required to obtain large silver particles with relatively short interparticle distances. In all cases, no significant differences are observed in the particle growth on the different types of support materials, as long as the interparticle distances (Ag particle size and surface density of silver) are similar. As was also seen in Figures 4.4-4.6, there appears to be an onset temperature. The onset temperature of the particle growth for particles with an initial particle size of 135 nm is a bit higher than for the other samples with smaller initial particle sizes (20 – 60 nm). This is not unexpected, as 135 nm particles are much more stable than nanoparticles, and approximate macroscopic silver properties.

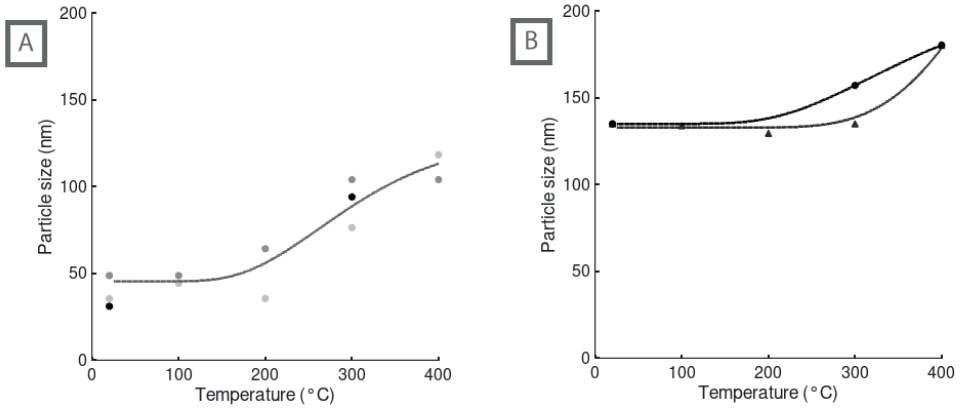

*Figure 4.7: Silver particle size of 3DOM (*Ag3DOM_15_45, *black), 8 $m^2 g^{-1}$ a-alumina (AgNP8_5_45, dark grey) and 1 $m^2 g^{-1}$ a-alumina (AgNP1_1_45, light grey) supported samples with a constant surface loading of 50 silver atoms per nm^2 (A) and silver particle size on 3DOM (circles) and crushed 3DOM (triangles) samples with a constant surface loading of 125 silver atoms per nm^2 (B) at different temperatures measured with DR UV/Vis spectroscopy. Lines added to guide the eye.*

The similar thermal stability both for the samples in Frame 4.7A as for the samples in the Frame 4.7B means that the diffusion of the mobile species over the support surface does not differ significantly over the different materials in this size range. This implies that the surface characteristics of the three support materials are comparable enough that differences in particle growth due to support characteristics can be neglected. It is remarkably that there is very little influence of the support on the thermal stability of the silver nanoparticles if all samples have the same interparticle distance, but that on the other hand the interparticle distance has a large influence on stability. This means that if the particle growth is primarily governed by the Ostwald ripening mechanism, the diffusion of the mobile species must be the rate limiting factor. This is rare for Ostwald ripening,[154,284,320,321] considering that the mobile species would be a cationic species, which are generally very mobile compared to metal particles.. Also, α-alumina has a low number of hydroxyl species and other surface defects, decreasing the sticking probability of the mobile species, what would be expected to relate to a high rather than a low diffusion rate. Therefore, it is more likely that instead the formation of oxidized silver species facilitates wetting of the support with the silver particles. As stated before, such a mechanism would only lead to appreciable silver particle growth for relatively short interparticle distances. Upon particle growth, at higher temperatures the interparticle distance increases due to the decrease of the number of particles, and hence growth due to silver particle coalescence slows down. This might result in Ostwald ripening becoming the dominant mechanism above a certain temperature, where this is not the case at the start of particle growth, when the interparticle distance is sufficiently small.

4.4 Conclusion

The thermal stability of silver particles supported on α-alumina depends on the gas atmosphere, with particle growth being pronounced in oxidizing atmospheres while in hydrogen atmosphere almost no increase in the average silver particle size was observed. In oxygen atmosphere, the interparticle distance had a strong influence on particle growth. For instance, an order of magnitude smaller interparticle distance (33 vs 355 nm) led to 60 nm silver particles growing

to much larger size (200 vs 80 nm at 400 °C). These effects were shown using samples with different silver particle sizes supported on three different kinds of supports (and a crushed version of one of these support materials). For a given silver weight loading and size, much more stable samples are obtained on supports with higher specific surface areas. The cage-like morphology of the 3DOM support material did not significantly influence the particle growth when the particles were small or when the particle size was similar compared to the pore size of the support material.

Based on these observations, it is clear that upon heating in oxidizing atmosphere, cationic silver species are formed, present on the support surface, and that these play an important role. They are expected to facilitate the spreading of silver over the support, and hence at short interparticle distances the spreading and subsequent coalescence of silver particles might dominate particle growth. Upon coalescence, the interparticle distance increases, hence growth following this mechanism is expected to gradually slow down. For long interparticle distances Ostwald ripening is dominant, in which cationic silver complexes are assumed to be the mobile species. Both mechanisms are suppressed in hydrogen, which does not allow the formation of oxidized silver species.

The high surface area of the 3DOM support material (and hence large interparticle distances) provides an excellent strategy to prevent particle growth. These types of materials can, therefore, be interesting to increase the stability of supported transition metal catalysts against deactivation by particle growth, for instance for the epoxidation of ethylene, for which the industrial catalyst is α-alumina supported silver particles with sizes similar to or larger than the particles described in this chapter.

4.5 Acknowledgments

This research was funded by NWO Vici project 16.130.344. Jochem Wijten and Marjan Versluijs-Helder are aknowledged for SEM imaging. Peter Lipman of Chemical Reactor Engineering, Eindhoven University of Technology for performing mercury intrusion experiments.

Support effects in silver catalyzed ethylene epoxidation

This chapter is based on: Catalysis Today, 338, pp. 31-39, 2019.

5

Abstract

In the epoxidation of ethylene, catalyzed by supported silver particles, the support plays not only a beneficial role, but can also negatively impact the selectivity to ethylene oxide. Especially high surface area supports, and supports containing acid groups, seem detrimental for the selectivity, which is attributed to secondary reactions on the support surface. We prepared Ag nanoparticles on supports with a wide range of specific surface areas and different chemical nature, such as commercial α-alumina and the 3DOM α-alumina described in chapter 3, but with similar Ag metal loading and particle size, using the method described in chapter 2. Indeed, a strong dependence of selectivity on both the specific surface area, and the chemical nature of the oxide support was found, with α-Al_2O_3 giving much more selective catalysts than SiO_2. Furthermore, the conversion was an important factor in determining the selectivity, while on the other hand the support had no influence at all on the ethylene conversion. We described our experimental selectivities with a reaction model that used the rate constant for the secondary reaction of oxidation of ethylene oxide to carbon dioxide and water as the only variable parameter. The model was able to adequately describe the experimental results. It gave insight into the dependence of selectivity on conversion, how the secondary reaction depended on the chemical nature of the support, and how its rate scaled linearly with the support's specific surface area. Building on this insight we modified a SiO_2 support to passivate its OH-groups, which indeed yielded a 94% decrease in the rate of the secondary reaction, performing even better than α-Al_2O_3 with similar specific surface area would. We have shown that the selectivity towards ethylene oxide is dependent on a metal specific, intrinsic selectivity, and the decrease in selectivity with conversion to be support dependent. This decrease is caused by the isomerization of ethylene oxide, which is found to be first order in ethylene oxide and the active sites on the catalyst support.

5.1 Introduction

In the epoxidation of ethylene selectivity is key, therefore it is interesting to investigate the reaction paths to ethylene epoxide, the desired product, and CO_2 formation, the unwanted side-product. In 1945 Twigg was the first to propose isomerisation of ethylene oxide to a short lived intermediate, which he proposed was acetaldehyde formed by isomerization of ethylene oxide.[322] Lee *et al.* showed for a wide range of metal oxide support materials that the support material catalysed the ring opening of ethylene oxide to form acetaldehyde [196]. However, since acetaldehyde is rarely found under reaction conditions, it is thought that acetaldehyde is rapidly further oxidized to CO_2 in the presence of silver [125,177,274]. This led to a proposed scheme for the silver catalyzed ethylene epoxidation as displayed in Figure 5.1.[323]

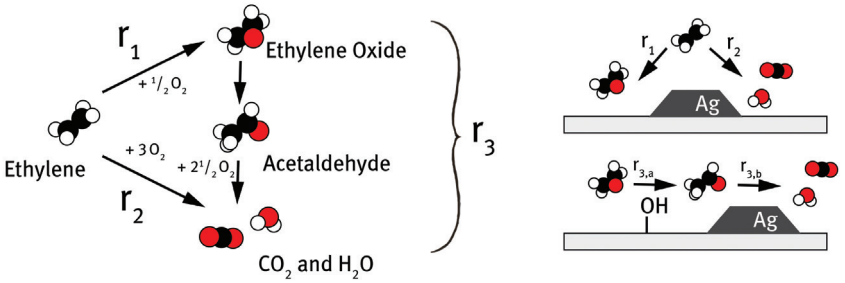

Figure 5.1: Proposed reaction scheme for ethylene oxidation over supported silver catalysts comprising several reaction steps. In first instance the ethylene is either selectively oxidized to ethylene oxide, or fully oxidized. The ethylene oxide formed can be recovered as a product but can also undergo consecutive oxidation via a two step-reaction: first the isomerization of ethylene oxide to acetaldehyde over the support and then the oxidation of acetaldehyde to water and carbon dioxide over silver.

Selective oxidation of ethylene to ethylene oxide (r_1) competes with full oxidation to CO_2 and H_2O (r_2). Full oxidation is thermodynamically more favorable than selective oxidation (-1323 kJ mol^{-1} compared to -106.7 kJ mol^{-1} respectively).[55] The ethylene oxide that is formed can also undergo oxidation (r_3); it is believed that isomerization to acetaldehyde ($r_{3,a}$) is followed by fast further oxidation ($r_{3,b}$). While reactions r_1, r_2 and $r_{3,b}$ are believed to be catalyzed by the metal particle, the isomerization of acetaldehyde is believed to occur on the catalyst support. A common strategy to limit side reactions on the support is minimizing the support specific surface area [177]. Yong, Kennedy and Cant showed a low selectivity towards ethylene oxide for high surface area supports such as titania and γ-alumina and a high selectivity over catalysts supported on low surface area materials.[324] They also reported an influence of the chemical nature of the support. Different rates of ethylene oxide isomerization for α-alumina and for silica supported catalysts were found.[324] This is in agreement with the results from Lee *et al.* who reported increased rates of ethylene oxide isomerization over acidic supports, with silica and α-alumina yielding higher selectivities and the α-alumina catalyst outperforming the silica supported catalyst.[196]

Apart from limiting the support surface area, and choosing a favourable support chemistry, such as done in catalysts described in chapter 2, another strategy is to tune the surface properties of a given support. Industrial catalysts contain caesium, which passivates acidic surface groups and limits the isomerization of ethylene oxide to acetaldehyde [17,22,25, 23] During preparation of the

catalyst, caesium is co-impregnated with silver, and is therefore not only present on the support surface, but also decorates the silver surface. [55,77,78] Özbek and van Santen showed that caesium also influences the reactivity of the active metal surface, as higher caesium concentration leads to lower overall conversion. [75,84,196,325,326] Although caesium generally improves the selectivity, in high concentrations it can even lead to lower overall selectivies, probably because caesium introduces oxygen vacancies on the silver surface, which are known to be active sites for full combustion.[81,84] It is clear that if one wants to study intrinsic support effects, promotors such as caesium should rather be avoided.

An open question that is seldomly addressed in academic open literature is the strong dependence of selectivity on conversion, the exact nature of this dependence and how it can be described.[71,212,327] Industrial sources report a linear decrease of selectivity with increasing conversion, based on empirical observations, without offering insight into the origin of this relationship.[328–331] It was proposed that the isomerization of ethylene oxide would be a first order reaction in ethylene oxide and dependent on the support [274,323,332]. The isomerization rate of ethylene oxide in the absence of ethylene was determined, but either only on bare support materials or with catalysts prepared using a variety of preparation methods, with a wide range of silver particle sizes and in the presence of (potential) promotors.[132,177,196,274,275,323,324,332]

To address this important question, we set out to show the effect of the support properties and understand the empirical correlation between conversion and selectivity, by carefully excluding effects due to differences in particle size, metal loading or the presence of promotors. To this aim we prepared series of catalysts on supports with different specific surface areas and surface groups, but having similar silver particle size and weight loading, and being prepared using the same metal precursor. For this, we use the procedure more extensively described in chapter 2, and both commercial support materials and the high surface area α-alumina described in chapter 3. The catalytic performance was described using a kinetic model, enabling us to quantify the impact of the support material on the selectivity, and understanding the correlation between conversion and selectivity in the ethylene epoxidation reaction.[328,332] An experiment in which silanol surface groups were blocked by organic capping agents demonstrated the strength of this approach to limit the secondary reactions and increased the overall selectivity of the reaction.

5.2 Methods

5.2.1 Catalyst preparation

A selection of fumed silica supports was obtained from Safic-Alcan Necarbo, specifically Aerosil OX-50, Aerosil 200, Aerosil 300, Aerosil 380, Aerosil R812 and Aerosil R972 (all produced by Evonik). These materials primarily differ by their specific surface area, except the latter two which are silylated versions of Aerosil 300 and Aerosil 150 respectively. A hydrophilic equivalent of Aerosil R812 was obtained after heat treatment of this material in a flow of oxygen (GHSV = 2000 hr^{-1}) at 400 °C for 2 hours to remove the organic capping agents. The hydrophilic analogue is expected to be equivalent to Aerosil 300. Quartz was supplied by Sigma Aldrich (≥99.995% trace metals basis). 1 $m^2 g^{-1}$ and 8 $m^2 g^{-1}$ α-alumina were obtained from Sigma-Aldrich (1 $m^2 g^{-1}$; 0.006 $cm^3 g^{-1}$; -100 mesh, Sigma Aldrich) and BASF (8 $m^2 g^{-1}$; pore volume 0.02 $cm^3 g^{-1}$, AL4196E, BASF) respectively. All support materials were pressed and sieved into a 38-90 μm sieve fraction prior to impregnation.

20 m^2 g^{-1} α-alumina was prepared using a procedure described before.[306] In a typical synthesis 1.5 g of PMMA colloidal crystal powder made by emulsion polymerization of methyl methacrylate (MMA, 99%, ≤30 ppm 4-methoxyphenol inhibitor, Sigma-Aldrich) was placed in a Buchner funnel and drop-wise wetted with approximately 3 mL solution of 1M aluminum nitrate nonahydrate in demineralized water/methanol (1:1 volume ratio) and soaked for 2 minutes. Thereafter the excess solution was removed by applying vacuum for 20 minutes resulting in a dry powder. The powder was wetted with ammonia/methanol (1:1 volume ratio) after which the excess solution is removed via vacuum suction and the sample was dried for 20 minutes. These steps were repeated three times before drying the powder overnight at room temperature. The dried powder was calcined at 1150°C under a nitrogen flow with a gas hourly weight velocity (GHWV of at least 20 $L g_{powder}^{-1}$ hr^{-1} for 6 hours after a 5°C min^{-1} heating ramp followed by a second calcination in a flow of oxygen with a GHWV of at least 20 L g_{powder}^{-1} hr^{-1} at 1150 °C for 6 hours after a 5°C min^{-1} heating ramp.

All catalysts were prepared by incipient wetness impregnation. Support materials were dried for 24 hours at 120 °C in a static oven in air. This was sufficient to remove adsorbed water from the macroporous pores of the alumina and from hydrophobic silica materials. For the hydrophilic silica some water was retained in the sample.

Table 1: Properties of catalysts used to estimate the dispersion of silver, per gram of silver or the density of silver particles on the surface in particles μm^{-2}

	SSA	Silver dispersion	Particle size	Particle volume	Particle footprint	Particle mass	Particle surface density
Sample	$m_{support}^2$ $g_{support}^{-1}$	$m_{support}^2$ g_{Ag}^{-1}	nm	nm^3 $particle^{-1}$	nm^2 $particle^{-1}$	g_{Ag} $particle^{-1}$	particles μm^{-2}
Al_2O_3_1	1	5.7	70	89797	3848	9.42E-15	18.7
Al_2O_3_8	8	45.3	75	110446	4418	1.16E-14	1.90
Al_2O_3_20	20	113.3	80	134041	5027	1.41E-14	0.63
SiO_2_0.1	1	5.7	110	348455	9503	3.66E-14	4.83
SiO_2_50	50	283.3	65	71897	3318	7.54E-15	0.47
SiO_2_200	200	1133.3	40	16755	1257	1.76E-15	0.50
SiO_2_380	315	1785.0	35	11225	962	1.18E-15	0.48
$MeSiO_2$_110	100	566.7	70	89797	3848	9.42E-15	0.19
$MeSiO_2$_260	225	1275.0	80	134041	5027	1.41E-14	0.06
$MeSiO_2$_260-ht	280	1586.7	80	134041	5027	1.41E-14	0.04

Silver oxalate was prepared by adding a 20 mL, 12 M aqueous solution of silver nitrate (99+%, Sigma-Aldrich) to a 40 mL, 12 M aqueous solution of oxalate dihydrate (99.5%, Merck) at 60 °C and filtrating and washing the precipitate with miliQ water.[200–202,212] A solution of 0.82 mmol g^{-1} freshly prepared $Ag_2C_2O_4$ in a mixture of ethylene diamine (en) and water (0.73 g/g milliQ/(en), or 1:4:16 mol ratio $Ag_2C_2O_4$: en : H_2O) was used to impregnate the support materials. In the case of hydrophobic supports a mixture of ethylene diamine, water and ethanol was used in a

volumetric ratio of 20 : 55 : 25 (en : water : ethanol) to ensure wetting of the support. The volume of solution added corresponded to the total pore volume as obtained from nitrogen physisorption. During impregnation, the solution was added dropwise to the dry support material which was continuously mixed to ensure a homogenous distribution of the silver salt over the support. The impregnated material was put in an oven at 60 °C in static air for 12 hours to dry. After 5, 10 and 30 minutes the material was thoroughly mixed to limit macroscopic inhomogeneities.[12]

The dry grains were heated in a U-shaped reactor to decompose the silver salt, forming a catalyst with 15 wt% silver and an average particle size of 60 nm. In typical heat treatment, 200 mg of sample was heated with a 5 °C min^{-1} ramp to a temperature between 215 and 300 °C in an oxygen or nitrogen atmosphere with a gas hourly weight velocity of 120 L g^{-1} hr^{-1} in order to obtain the desired particle size.[212] All catalysts had a nominal weight loading of 15 wt% of silver, but due to the different support specific surface area the silver surface density (Ag $m_{upports}^{-2}$) differs greatly between the catalysts, an estimation of the silver surface density is given in Table 5.1.

5.2.2 Characterization

Nitrogen physisorption isotherms for all support materials were measured at −196 °C on a Micromeritics TriStar 3000 apparatus. The specific surface area of the support was calculated by fitting experimental data with the BET equation ($0.05 < p/p^0 < 0.25$). BJH pore size distributions were obtained from the corresponding adsorption isotherm, with the total pore volume at a relative pressure of 0.995. For the high surface area α-alumina mercury porosimetry was performed using Micromeritics AutoPore IV 9500 to probe the large pores of the material. Pore volume data was calculated over the range 0.0007 – 227.5270 MPa. The contact angle between the support materials and the mercury was assumed to be 130° and the mercury surface tension and density 0.485 N m^{-1} and 13.5335 g mL^{-1}, respectively.

The size and spatial distribution of the obtained silver particles were measured using scanning electron microscopy (SEM). The images were obtained using a FEI XL30 FEG SEM. The images were processed using iTEM Soft Imaging System software.[204] Diffuse-Reflectance UV/Vis spectra of the supported silver catalysts were measured using a Varian CARY 500 Scan UV/Vis-NIR spectrophotometer with an integrating sphere. In a typical analysis, 30 mg of analyte was diluted with 600 mg pristine α-Al_2O_3 (1 m^2 g^{-1}, -100 mesh, Sigma Aldrich) and ground to a fine powder before taking a spectrum in the 1000 – 200 nm range. A background measurement of pristine α-Al_2O_3 was taken and subtracted from the obtained spectrum. Crystal phase analysis was performed with a Bruker D8 Phaser diffractometer (X-Ray Diffraction, Bruker D8 Phaser diffractometer equipped with a Co Kα source (λ = 0.1789 nm) using an angle range from 20° to 90° in 2θ and comparing XRD patterns with the PDF-4+ 2016 database.

The weight loss due to burning of the organic capping agents from the hydrophobic silicas was analyzed using a Perkin Elmer Pyris 1 TGA under a 10 mL min^{-1} flow of 20% oxygen in nitrogen. For these experiments the temperature was increased from 50 °C to 900 °C with a ramp of 5 °C min^{-1}. The decomposition products were analyzed using a Pfeiffer Vacuum OmniStar mass spectrometer.

5.2.3 Catalytic testing

In a typical catalysis experiment, 50 to 150 mg of catalyst grains (38-90 μm) was loaded in a

quartz reactor between two layers of quartz wool. To activate the catalyst, the sample was heated to 180°C in a flow of 16.5 mL min^{-1} of 8.5% oxygen and 30% ethylene in helium. The gas hourly weight velocity (GHWV) per gram of silver was varied over the 25 – 160 L g_{Ag}^{-1} hr^{-1} range in order to obtain ethylene conversions in the range of 0 to 10 % (after a stable conversion was obtained), and thus operate in differential conditions. The reaction products were characterized using online gas chromatography. The outlet gases of the reaction were analyzed every 15 min by an online Compact GC (Interscience) equipped with a Porabond Q column and a Molsieve 5Å column in two separate channels, both with a thermal conductivity detector. Conversion data were calculated from data retrieved after steady state was reached, which was typically after 8 hours.

5.2.4 Kinetic model describing selectivity trends

The overall reaction was modelled based on the reaction scheme presented in Figure 5.1. A primary selectivity is determined by the ratio between two parallel paths for the oxidation of ethylene: selective oxidation forming the desired product ethylene oxide (r_1) and full oxidation to form carbon dioxide and water (r_2). The ethylene oxide can either be retrieved, or oxidized further in the reactor (r_3) via the isomerization to acetaldehyde [322,332]. For the oxidation reactions r_1, r_2, that are assumed to occur over the silver nanoparticles, quite some information is available in literature.

Regarding r_1, the partial oxidation of ethylene to ethylene oxide, the reaction is taken to be first order in ethylene, which is a logical assumption, but also experimentally reported by Campbell *et al.* for experimental conditions similar to ours [333]. The reaction order in oxygen is taken as 0.5, being in the range of -0.5 to 1.5 as reported by Stegelmann *et al.* [62]. Furthermore both reaction orders are in line with the results of Linic and Barteau.[122]

For the full combustion of ethylene (r_2) a reaction order in oxygen in the -1 to 1 range, and typically close to zero, is reported by several different authors.[62,207,334] This zeroth order in oxygen might appear at first sight surprising, given the consumption of oxygen in this reaction. However, it is the combination of both a negative and a positive dependence on the oxygen partial pressure. The positive order stems from the consumption of oxygen in the reaction, but it is balanced by the fact that a more oxidized silver surface favors selective oxidation instead of full combustion [84]. Stegelmann *et al.* observed the ethylene reaction order in r_2 lower than the ethylene order in r_1 and is taken by us as $^1/_2$.[62]

Because both the r_2 and r_3 yield carbon dioxide and water at equal stoichiometry, it is not straightforward to derive the individual values from the overall catalytic data. Deconvolution of these rate constants was performed by extrapolating the obtained catalytic data of all measured catalysts to a conversion of 0.04% ethylene. At such low conversion, the ethylene oxide partial pressures is close to zero, and isomerization of this component, and hence r_3, can be neglected. The resulting selectivities are therefore governed by the ratio between r_1 and r_2. Hence the rates for r_1 and r_2 , and the corresponding rate constants k_1 and k_2, were calculated from the ratio r_1/r_2 and the overall reactant conversion rate (r_1+r_2) at the extrapolated conversion of 0.04%.

Using the obtained rate constants k_1 and k_2 and the experimental feed concentration as the initial conditions, the rates and partial pressures of each component were calculated differentially over the catalyst bed. In each step the result of the previous calculation was used, with initially values

defined by the feed composition. The conversion and selectivity were calculated for each step based on the calculated partial pressures at increasing catalyst bed lengths. A comparison of the calculated selectivities and the real experimental selectivities in the ethylene conversion range of 0 to 10 % allowed to derive the rate r_3 and corresponding rate constant k_3 for the isomerization of ethylene oxide to acetaldehyde, which was the sole fitting parameter. This value for k_3 for each individual catalyst. rate was obtained by a sum of least squares fit. The secondary reaction as represented by r_3 and k_3 is the process that determines the dependence of overall selectivity on support properties, and the correlation between conversion and selectivity, and is hence the main topic of this study.

5.3 Results

5.3.1 Catalyst preparation and characterization

The X-ray diffraction of representative support materials in the figure below shows sharp peaks for the diffractograms of the crystalline α-alumina and quartz materials in frames A-C. The peaks positions from the α-alumina samples shown in frames A and B are nearly identical, except for a shoulder at low diffraction angles for the 20 $m^2 g^{-1}$ α-alumina. Frame D shows a single, very broad peak without other features for an Aerosil 200. The diffractograms of other Aerosil samples are equivalent.

The crystalline nature of the α-alumina and quartz samples result in sharp peaks shown in frames A-C, with the peak positions corresponding to the peak positions obtained from the PDF-4+ database. Further analysis of the support materials, such as nitrogen physisorption and mercury porosimetry were used to confirm the specifications provided by the supplier and included in table 5.1 and 5.2 (discussed later in the chapter).

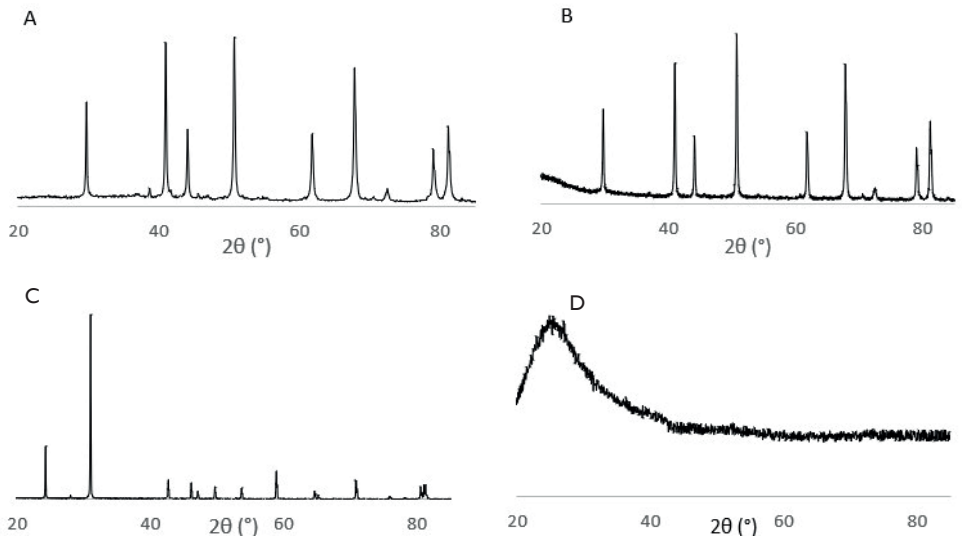

Figure 5.2: XRD diffractograms of 1 and 20 $m^2 g^{-1}$ a-alumina (frame A and B), quartz (frame C) and Aerosil-200 (frame D)

Catalysts in this chapter are coded via the method of Support_surface area, *i.e.* Al_2O_3*_1* is a

sample of α-alumina of 1 m^2 g^{-1} impregnated with silver and *SiO_2_380* is a sample of fumed silica of 380 m^2 g^{-1} impregnated with silver. In Figure 5.3 typical Scanning Electron Microscopy (SEM) images of a low surface area α-alumina and a low surface area fumed silica supported silver catalysts are shown. The support material is visible as a grey material, dotted with bright white silver metal particles. The *Al_2O_3_1* catalyst in the left image is supported on large jagged chunks of non-porous material. The silica support (middle frame) has a fine structure and appears to have smaller silver particles than the α-alumina supported catalyst. The histogram (obtained from measuring at least 300 particles) in the right frame shows that the average particle size is only slightly different (surface area corrected average particle size of 70 nm for *Al_2O_3_1* compared to 60 nm for *SiO_2_50*), while the size distribution (fitted as a log-normal distribution) is significantly broader on the former, with some particles with sizes of 100-150 nm being present. The apparent difference between the silver particle sizes in the left and middle frame is due to these large particles being more noticeable.

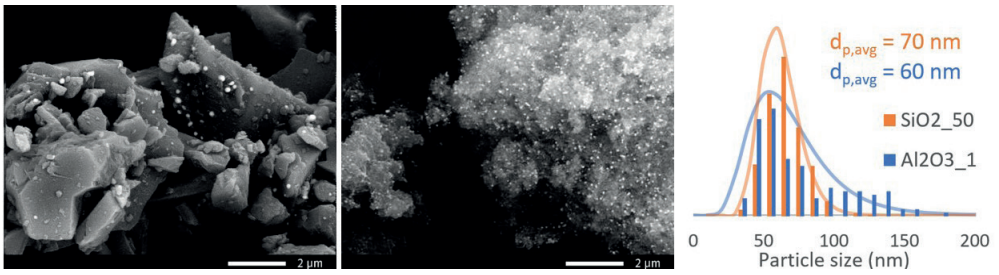

Figure 5.3: Electron microscopy images of silver on an α-Al_2O_3 support with a support specific surface area of 1 m^2 g^{-1} (Al_2O_3_1, left), silver on a fumed silica support with a support specific surface area of 50 m^2 g^{-1} (SiO_2_50, middle) and histogram of the diameter of the silver particles on both catalysts. These histograms are obtained from measuring at least 300 particles and are subsequently normalized to accurately compare the distributions.

The large crystallites, in the case of the α-alumina support, can be explained by the preparation method of the support materials, as they are produced at high temperatures to crystallize to the most thermally stable α-alumina phase (at least 1000 °C before α-alumina is formed), causing a collapse of most of the material porosity and condensing surface groups.[178,245,296] The silica support is prepared by sintering small silica spheres (5 - 50 nm in diameter) into an agglomerate which has no defined shape and exhibits interparticle nanoporosity.[164] The temperature at which this flame hydrolysis is performed determines the support specific surface area, but does not reach the temperatures needed to crystallize the silica.[164] XRD (see Figure 5.1) confirms the highly crystalline nature of the α-alumina and the amorphous nature of the fumed silica.

An overview of the main characteristics of the silver catalysts and the different support materials used, is given in Table 5.2. The α-alumina and quartz support materials exhibit low specific surface areas and therefore a low amount of surface hydroxyl species per gram of material. The α-alumina supports have surface areas ranging from 1 to 20 m^2 g^{-1}, with the highest specific surface area belonging to a non-commercial ordered macroporous α-alumina that was made in-house [306]. Quartz has a support specific surface area of 0.1 m^2 g^{-1} as specified by the supplier. Due to the low surface area this value could not be reliably verified due to the measurement error of nitrogen physisorption. The fumed silica materials have surface areas ranging from 50 to 380 m^2 g^{-1}. Note the low specific surface area of the silylated supports compared to the hydrophilic counterparts

(entries *SiO_2_300*, *$MeSiO_2$_260* and *$MeSiO_2$_260-ht*). These are expected to have similar specific surface areas since the hydrophobic silica (support used in sample *$MeSiO_2$_260*) is obtained via silylation of the hydrophilic silica (a 300 $m^2 g^{-1}$ Aerosil) and *$MeSiO_2$_260-ht* is prepared by a heat treatment of *$MeSiO_2$_260*. The slight gain in specific surface area after converting hydrophobic (*$MeSiO_2$_260*) into hydrophilic (*$MeSiO_2$_260-ht*) silica suggests that for the hydrophobic silica the organic species are blocking part of the pores.

Table 5.2: Catalysts with support characteristics and average metal particle sizes

	Support material		Specific surface area support (m^2g^{-1})		Density of hydroxyl species (OH nm^{-2})	Ag particle size (nm)	
Catalyst	Brand name	Type	Provided by supplier	Nitrogen physisorption		TEM/SEM ± sigma	UV/Vis (SPR Peak position)‡
Al_2O_3_1	N/A	α-alumina	1	<5	6[170,171]	71 ± 25	70 (457)
Al_2O_3_8	AL4196E	α-alumina	8	n.d.	6[170,171]	77 ± 22	72 (463)
Al_2O_3_20	N/A	α-alumina	N/A	20*	n.d.	n.d.	80 (480)
SiO_2_0.1	N/A	Quartz	0.1	<1	<3[335–337]	110 ± 70	108 (503)
SiO_2_50	Aerosil OX50	Fumed silica	50	46	3[164]	60 ± 15	70 (455)
SiO_2_200	Aerosil 200	Fumed silica	200	196	3[164]	42 ± 9	41 (401)
SiO_2_380	Aerosil 380	Fumed silica	380	315	3[164]	34 ± 11	41 (400)
$MeSiO_2$_110	Aerosil R972	Hydrophobic fumed silica	110	97	0.71[338]	68 ± 33	71 (435)
$MeSiO_2$_260	Aerosil R812	Hydrophobic fumed silica	260	225	0.44[339]	79 ± 39	77 (485)
$MeSiO_2$_260-ht	N/A	Heat treated Hydrophobic fumed silica	N/A	278	n.d.	n.d.	77 (485)

‡ Peak maximum of surface plasmon resonance peak in diffuse reflectance UV/Vis spectroscopy
** Support specific surface area as determined by mercury intrusion*

The density of hydroxyl species is slightly higher for the alumina than for the silica supports in table 5.2, while the differences between the crystalline and amorphous silica materials are small.[170,340] It must be said that the determination of the exact number of surface species is difficult for materials with such low specific surface area and can differ significantly based on the preparation procedure.[170] It is expected that the density of these species is lower on crystalline surface as the more reactive species are condensed. [170,340] When the amorphous silica materials are silylated in order to block the surface hydroxyl species (*$MeSiO_2$_110* and *$MeSiO_2$_260*), a sharp decrease in the density of hydroxyl species is observed (compared untreated to Aerosil material). This significant drop in hydroxyl density is expected because these species have reacted with the silylating agent, resulting in inert siloxy groups. The catalyst supported on quartz (*SiO_2_0.1*) does differ in chemical nature from the rest of the silica samples but acts as a low surface silica which

can be compared with the low surface area α-alumina catalysts.

The catalysts tabulated in table 5.2 have a wide range of support specific surface area (0.1 – 380 nm^2), while the metal weight loading and silver particle sizes are very similar. This is achieved by carefully adjusting the heat treatment conditions during catalyst preparation, as was more extensively discussed in a previous publication.[212] In previous studies large variations in support properties were always accompanied by different particle sizes. In our case we have been able to tune the particle size to a limited range for which we reported earlier that variations within this particle size range are not expected to significantly affect the selectivity.[212] This allows to attribute observed differences in catalytic results as discussed in the next section solely to the differences in chemical nature and specific surface area of the support material.

5.3.2 Catalysis

The temperature dependent catalytic performance of two catalysts (*Al_2O_3_1* and *SiO_2_200*) is shown in Figure 5.4. We selected these two examples as the specific support surface and nature of these two catalysts differ greatly. The oxidation of ethylene starts around 170 °C with similar activity over the whole temperature range for these two catalysts (left frame Figure 5.4). In the middle frame, the selectivities are plotted versus the reaction temperature. Selectivities toward ethylene oxide range from 40 to 75 % for the α-alumina supported catalyst. For the silica supported catalyst the selectivies are clearly lower, ranging from 20 to 50%. In the right frame of Figure 5.4, the Arrhenius plots show the activation energy for the epoxidation reaction for both catalysts, based on the yield of ethylene oxide. The apparent activation energies for ethylene oxide formation of 74 and 67 kJ mol^{-1} for catalysts supported on silica and alumina respectively are well in line with the activation energies reported in literature, which range from 50 to 80 kJ mol^{-1}.[62,97,331,341]

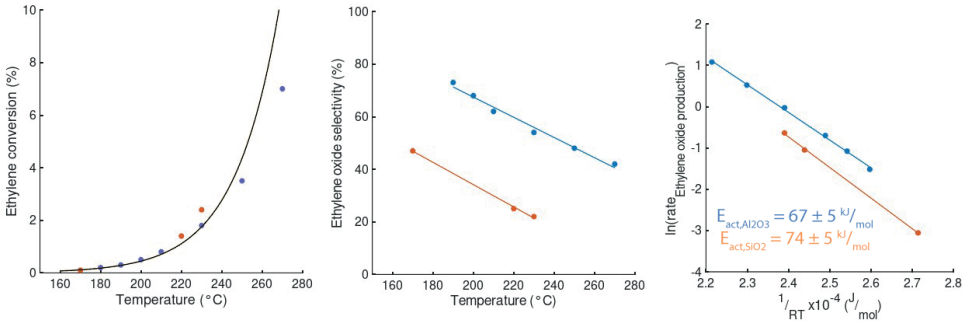

Figure 5.4: Conversion (left), selectivity (middle) and Arrhenius plots (right) for the formation of ethylene oxide of Ag_Al_2O_3_1 *(blue) and* Ag_SiO_2_200 *(orange) measured at a GHWV of 43 L g_{Ag}^{-1} hr^{-1} at atmospheric pressure. Lines added to guide the eye.*

The remarkably similar conversions over the entire temperature range in the left frame of Figure 5.4 strongly suggests that neither the nature of the support nor the silver surface density (Ag $m_{support}^{-2}$) influence the activity of the catalyst. The very similar activation energies observed on the two totally different supports as represented in the right frame of Figure 5.4 imply that the same is true for the rate r_1; and since the overall ethylene conversions are nearly identical, this also applies to r_2. First of all, this shows the accuracy and reproducibility of the measurements.

The same metal precursors and solvents were used in the preparation of all catalysts. The results validate our starting point that our preparation method leads to Ag nanoparticles that are very similar in properties, despite being prepared on very different supports in terms of chemistry and surface area. Furthermore, it validates the assumption that the oxidation reaction of ethylene occurs solely on the silver particles, and that the primary selectivity (which fraction of ethylene is converted to the desired product, and which fraction is combusted) is independent of the support used.

The overall selectivity in the middle frame shows a very different picture, with a much higher selectivities for the low surface area α-alumina than for the high surface area silica supported catalyst. This confirms earlier reports of support-dependence of the selectivity and is attributed to a secondary selectivity loss mechanism via subsequent oxidation of the formed ethylene oxide. It is likely that the isomerization of ethylene oxide ($r_{3,a}$) is catalyzed by surface groups of the support. The subsequent oxidation of acetaldehyde ($r_{3,b}$) is assumed to occur on the silver particles rather than on the support surface, and hence is expected to occur with a similar rate for all catalysts. The decreasing selectivity with increasing conversion, as shown in the middle frame, has been reported before,[306,329] stating a linear or first order correlation.[274,329,332,342] However, no chemical or physical explanation for this relation has been given. In the following section we try to describe and understand the dependence of selectivity on support properties and conversion. For a direct comparison of the selectivity, catalytic performance should be compared at similar conversion instead of at different temperatures, to exclude the contribution of differences in activation energies due to the different temperatures. Hence, all further measurements discussed in this chapter are obtained at a constant temperature of 180 °C, and desired conversions were obtained by changing the gas hourly weight velocity (GHWV) rather than the temperature.

5.3.3 Influence of the conversion on the selectivity

In Figure 5.5, the selectivity to ethylene epoxide as a function of ethylene conversion is shown for different types of catalysts. Only results up to 10% ethylene conversion are displayed, as for higher conversions mass transfer limitations start to play a major role. This cut-off point was determined using the Mears criterion,[214] which exceeds 0.15 for conversions higher than 7.5%, meaning external mass transfer limitations can not be neglected. Calculations of the expected oxygen partial pressure also show a depletion of oxygen somewhere between 8 and 9% ethylene conversion *i.e.* corresponding to an oxygen conversion of 100% or more.[345] The materials with the lowest support specific surface area for each support type produce the highest selectivity towards ethylene oxide for a given conversion. Striking is that, although the selectivities vary widely, at the lowest possible conversions measured all selectivities converge to a similar value (around 76%). This implies a metal specific, intrinsic primary selectivity, which is independent on the type and the specific surface area of the support, and hence determined solely by the silver metal.

Another general observation is that the low surface area alumina-supported catalysts exhibit significantly higher selectivities than the catalyst with the highest support specific surface area, *SiO_2_380* (left frame of Figure 5.5, in red). Also, within the family of alumina-supported catalysts, there is a clear correlation with specific surface area, with decreasing selectivity with larger surface area. This trend of decreasing selectivity with increasing surface area also holds for all the hydrophilic silica supported samples (right frame).

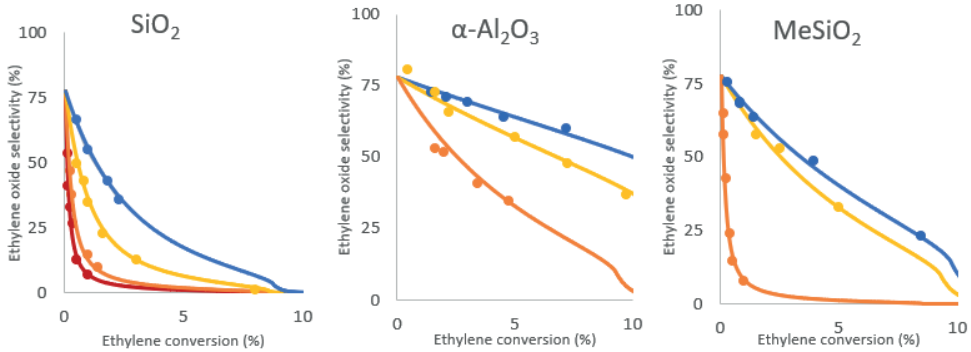

Figure 5.5: Catalytic performance over a 0 – 10 % range of ethylene conversions for silica supported (left), a-alumina supported (middle) catalysts showing a support specific surface area and conversion dependent selectivity. The catalysts supported on hydrophobic silica, including the heat treated $MeSiO_2$*–260-ht (orange) are shown in the right frame. The samples are color-coded in each frame with the lowest surface area sample represented in blue, then yellow, orange and red for the highest surface area catalyst. Markers correspond to averaged conversion and selectivity obtained after at least 2 hours of steady state operation after setting the GHWV. All data is obtained at an operating temperature of 180 °C. Different conversion were obtained over a range of 25-160 hr^{-1} GHWV. Drawn lines correspond to first order fit of catalytic data using the method described.*

It has been reported before that the selectivity of this process generally decreases with increasing conversion, but there are no earlier reports on the exact dependence. Based on empirical correlations for low-surface area alumina-supported catalysts, such as *Al_2O_3–1* in middle frame of Figure 5.5 (in blue), a linear dependence is assumed, without a theoretical framework to explain this linearity. However, from our results it is clear there is no simple linear correlation, but that in fact the correlation is more complicated. Considering the overall reaction steps describe earlier in this work, it can be expected that the selectivity is inversely dependent on the ethylene oxide partial pressure. As with increasing ethylene oxide partial pressure, the rate r_3 increases. While this trend is well accepted and provides a satisfactory qualitative description of the dependencies of the selectivity with conversion and support specific surface area, the mechanism of this secondary reaction is not extensively studied and a linear decay with conversion is often presumed. In the following section we will discuss a precise model to describe the catalytic data, and the dependence of selectivity on conversion and support properties, allowing more insight in the underlying mechanisms and providing a quantitative description of the rate of the secondary reaction.

5.3.4 Quantitative description and understanding of the selectivity trends

Our model to describe the experimental results consists of two parallel and one consecutive reaction (with rates r_1, r_2 and r_3 respectively) and is given in Equations 5.1-5.4. In these equations the partial pressures of the relevant compounds ethylene, oxygen, ethylene oxide and acetaldehyde are represented as $p_{C_2H_4}$, p_{O_2}, p_{EO} and p_{AA} respectively. The rationale for the reaction orders in r_1 and r_2 is explained in the experimental section. The primary selectivity is determined by the balance between the two possibilities for the oxidation of ethylene: selective oxidation forming the desired product ethylene oxide (r_1) and full oxidation to form carbon dioxide and water (r_2). The ethylene oxide product can either be retrieved or oxidized further in the reactor (r_3). This secondary reaction involves isomerisation of ethylene oxide to acetaldehyde ($r_{3,a}$) and subsequent full oxidation of the isomer, yielding carbon dioxide and water ($r_{3,b}$). Isomerisation to acetaldehyde is considered the

rate limiting step,[125,177,274] hence the rate of $r_{3,b}$ is considered to be infinitely fast, and the overall reaction rate r_3 can be taken as equal to $r_{3,a}$, and is modelled as a first order rate equation. The rates of the three reactions r_1, r_2 and $r_{3,a}$, were obtained from fitting the experimental data.

$$r_1 = k_1 p_{C_2H_4} p_{O_2}^{1/2} \quad (5.1)$$
$$r_2 = k_2 p_{C_2H_4}^{1/2} \quad (5.2)$$
$$r_{3,a} = k_{3,a} p_{EO} \quad (5.3a)$$
$$r_{3,b} = k_{3,b} p_{O_2}^{n} p_{AA}^{m} \quad (5.3b)$$
$$\text{if } r_{3,a} >> r_{3,b}$$
$$r_3 \approx k_3 p_{EO} \quad (5.4)$$

We considered the experimentally obtained selectivities as a function of conversion for all catalysts presented in Table 5.2. The drawn lines in Figure 5.5 represent the calculated selectivities versus conversion for a selection of these catalysts. Our experimental results clearly showed that at very low ethylene conversions (and hence negligible ethylene oxide concentrations) results for all our supported silver catalysts converge to the same selectivity of 76%. This is in line with earlier reports that at constant conversion there is no intrinsic effect of particle size on selectivity.[212] From this value, which represents the metal specific selectivity, the ratio between r_1 and r_2, and hence k_1 and k_2 was derived. The average value of the k_1/k_2 values derived from the extrapolation of all individual catalysts in the dataset was used as a fitting constraint for the rate constants of the r_1 and r_2 reactions for all samples.

We took a fixed value for the orders of reactions r_1 and r_2, but in fact the variation in oxygen partial pressure does influence the reaction order of both oxygen and ethylene in the r_1 and r_2 reactions.[62,101,122,333] To justify our simplification, we performed a robustness test in which the same calculations were performed with oxygen reaction orders over the ranges mentioned in literature (-0.5 to 1.5 in oxygen and 1 in ethylene for r_1 and -1 to 1 in oxygen and 0 in ethylene for r_2).[62,84,122,333]. The reaction orders in r_1 and r_2 did not significantly influence the shape of the fitted curve but did change the absolute value of k_3. This did not influence the capability of the model to fit the data, as the relative values did not change. The higher reaction orders in oxygen (above 0 and 0.5 for r_1 and r_2 respectively) could not adequately describe the experimental data. These observations support our hypothesis that the orders in both oxygen and ethylene in r_1 and r_2 are not determining factors in our assessment of the role of the support on the r_3-reaction. Moreover, at industrially relevant and non-mass transfer limited conversions, the partial pressures of oxygen and ethylene do not significantly change and therefore only play an indirect role.

It is clear from Figure 5.5 that our model is capable of adequately describing the overall decreasing selectivity with increasing conversion. Also, the absolute selectivities calculated using our model correlate well with the measured values for all catalysts. As the rate orders in r_1 and r_2 did not have a large influence on these data, it can be concluded that the good correlation between the measurement and the calculated data is primarily determined by the r_3 reaction, the isomerization of ethylene oxide. From the decrease in selectivity with increasing conversion, for each catalyst a value for k_3, was derived, which depended on the nature and surface area of the support and is discussed in detail in the following section. The strong dependence on the support led to the conclusion that the rate limiting step for the oxidation of ethylene oxide, the isomerization of ethylene oxide to acetaldehyde, occurs over the catalyst support, rather than on the metal surface

as is an often proposed theory.[62,188,274] As stated, before at low ethylene conversions the support has no influence on selectivity, hence selective (r_1) and full oxidation of ethylene (r_2) can therefore be assumed to solely occur on the surface of the metal particle.

As an illustration of how well the model is able to describe the experimental selectivities, it is interesting to have a close look, at the sharp drop in selectivity for the *Al_2O_3_20* sample in Figure 5.5 at a conversion of circa 9%, which is correctly predicted with our model. As the unselective reactions r_2 and r_3 consume more oxygen than the selective reaction (r_1), the atmosphere is deprived of oxygen at low selectivities and high conversions. In the case of *Al_2O_3_20*, the resulting oxygen partial pressure is very low (<0.0034 atm compared to 0.085 atm in the feed, which corresponds to an oxygen conversion of 96 %). This drop is correctly described in our model by the positive reaction order in oxygen for the selective r_1 reaction while the reaction order in oxygen for full oxidation r_2 reaction is zero. These orders reflect the fact that a more oxidized silver surface favors the selective oxidation, and hence at these very low oxygen contents the full oxidation reactions are more dominant.[79,84] As the reaction follows the Mars-Van Krevelen type mechanism, these low oxygen contents are insufficient to reoxidize the surface. At the sites where these "oxygen vacancies" exist, the underlying silver is exposed which acts as an active site for the unselective r_2 reaction, the reduced rate of reoxidation causes a sharp drop in the selectivity towards ethylene oxide.[195]

5.3.5 Influence of the nature and specific surface area of the support

The data in Figure 5.5 clearly show that the specific surface area of the support has a strong influence on the selectivity, but also the chemical nature of the support seems to play a role. To unravel these two factors, the values for k_3 obtained from all catalysts mentioned in Table 5.2 (catalytic data in Figure 5.5) were plotted versus the specific surface of the support materials (Figure 5.6). To minimize the error originating from slight differences in overall activity, the obtained k_3 values were divided by the corresponding value for k_1 obtained from the fit. A high value for k_3 corresponds to a low selectivity while a low value corresponds to a very selective catalyst.

The three α-alumina supported catalysts are plotted in blue. These catalysts have a low support specific surface and low values for k_3/k_1 (hence high selectivities). The silica supported samples are depicted in orange, these catalysts have a wide range of support specific surface areas and values for k_3/k_1. The silica-supported catalyst with the lowest support specific surface area, the quartz supported *SiO_2_0.1*, is an outlier with a higher k_3/k_1 ratio than expected. We tentatively explain this by a relatively large error in the exact value for the specific surface area value (provided by supplier). The open symbols correspond to the catalysts supported on surface-treated silica with intermediate to high SSA, but low values for k_3/k_1. *$MeSiO_2$_260-ht* is depicted as the open square, with k_3/k_1 in line with the untreated silica. For both the alumina and silica supported catalysts, the data were accurately described with a linear relation between the rate constant and specific surface area of the support. The slope depends strongly on the type of material, with a larger slope for the silica than for the alumina-supported and hydrophilic silica catalysts.

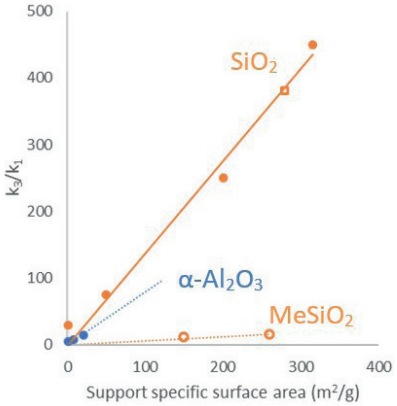

Figure 5.6: k_3/k_1 obtained from fitting catalytic data of supported silver catalysts grouped by support material (α-alumina in blue and silica in orange) versus support specific surface area. Open symbols corresponding to silylated silica with the heat-treated sample (alkyl surface groups removed again) indicated by a square. Trendlines are added to guide the eye, these lines are forced through the origin and the dashed lines are extrapolated to more clearly indicate the differences in the slope of the different families.

Figure 5.6 shows that the rate constant of isomerization is proportional to the specific surface area, but only for a given support. Deviations from the linear regression are small and can be ascribed to the experimental error in the fit by the model. However, a non-zero rate of isomerization in the absence of support material could also be considered. Possibly due to some minor isomerization occurring over the metal particle.[62,188,274] This is an interesting topic for future investigations, but not considered further in this work. Mind that the rate constant of the isomerization of the product ethylene oxide to acetaldehyde, k_3, is not a true rate constant of an elementary reaction. Assuming that within a set of materials, the surface density of the active surface groups can be considered constant [164], this linear relation suggests that the reaction can be considered as a first order reaction in the concentration of active surface species. Figure 5.6 also shows that the slope is higher for silica than α-alumina. However, this cannot be explained just based on the surface concentration of hydroxyl species on each material (see Table 5.2). [170,171,184,335–339] This suggests that the hydroxyl species on α-alumina are more reactive than the hydroxyl species on silica supports. This provides an explanation for the observations of Lee and Yong, who state that silica support materials are relatively inert,[188,196] and Chongterdtoonskul and Goncharova stating that high surface area of their alumina samples yield overall low selectivities.[157,343]

As the strength and the amount of the active species play a role, the observations of Lee and Yong and Chongterdtoonskul and Goncharova could both be explained by variations of these two parameters in the material. We have tested a set of catalysts on low surface area support with relatively acidic surface species, such as niobia and strontiumtitanate. These types of supports are reported to be very selective by Chongtertoonskul.[343,344] In our case, these catalysts exhibited selectivities towards ethylene oxide similar to a silica catalyst with a specific surface area of 380 $m^2\ g^{-1}$ for the niobia supported catalyst and 70 $m^2\ g^{-1}$ for the strontiumtitanate sample (Figure 5.7), while both have a specific surface area lower than 20 $m^2\ g^{-1}$. This is in accordance to the observations of both Lee and Yong, where acidic support materials exhibit lower selectivities towards ethylene oxide.[196,324] We attribute this to a higher rate of ethylene oxide isomerization over

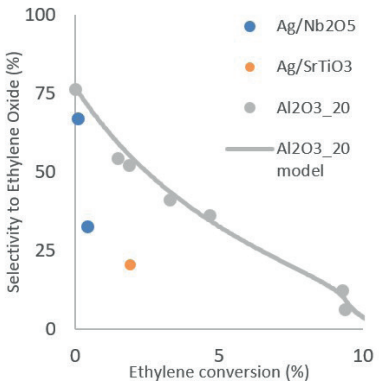

Figure 5.7: Catalytic performance of niobia (blue) and strontiumtitanate (orange) supported silver (15 wt%) catalysts, compared to Al_2O_3_20 sample also shown in Figure 5.5. GHSV = 25 – 160 L g_{Ag}^{-1} hr^{-1} of 30 vol% ethylene and 8.5 vol% oxygen in helium balance at 180 °C and atmospheric pressure.

acidic support species.

A very striking and interesting feature in Figure 5.6 are the low k_3/k_1 values for $MeSiO_2$-110 and $MeSiO_2$-260. While the support specific surface area of these materials is comparable to the other silica supported samples, the selectivity towards ethylene oxide is much higher; the decrease in the k_3/k_1 value is 96 %. This means that the 260 m^2 g^{-1} silica supported catalyst has a similar catalytic performance to a 20 m^2 g^{-1} α-alumina catalyst. In this sample the original silanol groups are blocked by organic species. When these alkyl groups were burned off by heat treatment (square in Figure 5.6), the sample, *$MeSiO_2$-260-ht*, had a k_3/k_1 value similar to a catalyst supported on untreated silica with a similar specific surface area. This clearly shows that the difference in selectivity can be solely attributed to the difference in the support material, in this case the chemical nature of the surface.

5.4 Conclusion

Supported catalysts with silver particle sizes of 40 – 70 nm were prepared on silica and α-alumina supports with varying specific surface areas. The silver weight-based activity of the catalysts was similar for all catalysts. However, the selectivity in the ethylene epoxidation, the most critical factor, depended strongly on the support and on the conversion. Although it was known in the literature that the selectivity decreased with increasing conversion, this effect had not been described in detail. Using a kinetic model, we could accurately describe the catalytic selectivity of our range of supported silver catalysts and conversions. Even seemingly surprising features, such as a sudden drop in selectivity at relatively high conversions due to a low oxygen content, was faithfully modeled. Our data fully supported that the primary selectivity (at very low conversions) is governed by the two alternative reaction paths for the ethylene reactant on the silver catalyst surface, while a further loss of selectivity at higher conversions is caused by a secondary reaction involving the support surface, most likely ethylene oxide isomerization to acetaldehyde followed by complete combustion.

Building on the hypothesis of a first order in ethylene oxide for this secondary reaction, the rate constants were shown to be linearly dependent on the support specific surface area but

differed per material type. The presumed active sites for the isomerization reaction are hydroxyl groups, and the proportionality suggests a first order in the hydroxyl species. The difference in rate constant for either silica or α-alumina did not simply scale with the hydroxyl density on these supports, so probably the rate of isomerization does also depend on the specific properties of the surface sites.

We clearly showed that the loss of selectivity with increasing conversion depends directly on the density of active surface groups, and hence specific support surface area. In this chapter, we kept the weight loading similar to the low surface area supported catalysts, but in industry, one would ideally be able to use a high surface area support (and hence silver loading and volume activity) without losing too much selectivity. We showed that passivation of the silanol groups of a high surface area silica support, led to a selective, high surface area catalyst. The selectivity to ethylene oxide for this catalyst supported on modified silica was similar to that of an α-alumina supported catalyst with ten times lower specific surface area. High surface area supports allow to increase the silver weight loading, potentially leading to even higher selectivities as the metal is expected to block reactive hydroxyl species on the surface and to the possibility to load more active catalyst surface per reactor volume. Alternatively, these materials could be used to produce more stable catalysts as the high interparticle distance increases the stability against deactivation due to sintering. This could even be combined with the tentative insights in catalyst stability obtained in chapter 4, in order to further optimize the catalyst stability.

5.5 Acknowledgements
This research was founded by NWO Vici project 16.130.344. Jan-Willem de Rijk, Carlo Buijs (SCR Technical University Eindhoven) and Marlies Coolen-Kuppens (SCR Technical University Eindhoven) are aknowledged for their help on the epoxidation setup and Marjan Versluijs-Helder for SEM and TGA measurements.

Back Matter

References

(1) Centi, G.; Ciambelli, P.; Perathoner, S.; Russo, P. Environmental Catalysis : Trends and Outlook. *Catal. Today* **2002**, *75*, 3–15.

(2) European Union. Directive 2001/100/EC. 2002, pp 32–34.

(3) Hussain, M.; Russo, N.; Saracco, G. NOx Abatement by HC-Assisted SCR over Combustion Synthesized-Supported Ag Catalysts. *Ind. Eng. Chem. Res.* **2012**, *51* (22), 7467–7474.

(4) Santen, R. van. Catalysis in Perspective: Historic Review. *Catal. From Princ. to Appl.* **2012**, 3–19.

(5) Campelo, J. M.; Luna, D.; Luque, R.; Marinas, J. M.; Romero, A. a. Sustainable Preparation of Supported Metal Nanoparticles and Their Applications in Catalysis. *ChemSusChem* **2009**, *2* (1), 18–45.

(6) Boudart, M. Heterogeneous Catalysis by Metals. *J. Mol. Catal.* **1985**, *30* (1–2), 27–38.

(7) van Santen, R.; van Leeuwen, P.; Moulijn, J.; Averill, B. A. Preparation of Catalyst Support Supports, Zeolites and Mesoporous Materials. In *Catalysis: An Integrated Approach*; 1999; pp 433–457.

(8) van Santen, R. A.; van Leeuwen, P. W. N. M.; Moulijn, J. A.; Averill, B. A. Preparation of Supported Catalysts. In *Catalysis: An Integrated Approach*; Elsevier Science, 1999; pp 459–485.

(9) Regalbuto, J. Catalyst Preparation: Science and Engineering By John R. Regalbuto. In *AIChE Journal*; CRC Press, 2006; Vol. 55, p 488.

(10) Deutschmann, O.; Knözinger, H.; Kochloefl, K.; Turek, T. Heterogeneous Catalysis and Solid Catalysts. In *Ullmann's Encyclopedia of Industrial Chemistry*; 2009; pp 1–62.

(11) Taylor, B.; Lauterbach, J.; Delgass, W. N. Gas-Phase Epoxidation of Propylene over Small Gold Ensembles on TS-1. *Appl. Catal. A Gen.* **2005**, *291* (1–2), 188–198.

(12) Plessers, E.; van den Reijen, J. E.; de Jongh, P. E.; de Jong, K. P.; Roeffaers, M. B. J. Origin and Abatement of Heterogeneity at the Support Granule Scale of Silver on Silica Catalysts. *ChemCatChem* **2017**, *9* (24), 4562–4569.

(13) Konuk, K. Asia Minor to the Ionian Revolt. In *The Oxford Handbook of Greek and Roman Coinage*; Oxford University Press, 2012; pp 43–60.

(14) Goldstein, J.; Kestenbaum, D. A Chemist Explains Why Gold Beat Out Lithium, Osmium, Einsteinium ... [Visited 11 March 2018] Https://Www.Npr.Org/, 2010.

(15) Matos, G. R.; Hilliard, H. E.; Brooks, W. E. Silver end-use statistics [Visited 11 March 2018] https://minerals.usgs.gov/minerals/pubs/commodity/silver/.

(16) Matos, G. R.; Amey, E. B.; George, M. W. Gold end-use statistics [Visited 11 March 2018] https://minerals.usgs.gov/minerals/pubs/commodity/gold/.

(17) Matos, G. R.; Edelstein, D. L. Copper end-use statistics [Visited 11 March 2018] https://minerals.usgs.gov/minerals/pubs/commodity/copper/.

(18) World Gold Council. Gold price since december 1978 [Visited 11 March 2018] www.gold.org.

(19) Kitco. Historical London Fix Prices [Visited 11 March 2018] http://www.kitco.com/gold.londonfix.html.

(20) Barbalace, K.; Barbalace, R.; Barbalace, J. Periodic Table [Visited 11 March 2018] https://environmentalchemistry.com/.

(21) Infomine.com. 1 Year Copper Prices and Price Charts [Visited 11 March 2018] http://www.infomine.com/investment/metal-prices/copper/1-year/.
(22) Kramida, A.; Ralchenko, Y.; Reader, J.; (2018), N. A. T. NIST Atomic Spectra Database (ver. 5.5.2) [Visited 12 March 2018] physics.nist.gov/asd.
(23) Engineering ToolBox. Metals and Alloys - Densities [Visited 12 March 2018] www.engineeringtoolbox.com/metal-alloys-densities-d_50.html.
(24) Engineering ToolBox. Metals - Melting Temperatures [Visited 11 March 2018] www.engineeringtoolbox.com/melting-temperature-metals-d_860.html.
(25) Engineering ToolBox. Malleability, Brittlenes and Ductility [Visited 12 March 2018] www.engineeringtoolbox.com/Malleability,-Brittlenes-and-Ductility-d_1851.html.
(26) McNay, D. Consumer Characteristics and Factors Affecting Demand. In *Industry & Trade Summary Precious Metals*; DIANE publishing, 1995; pp 16–21.
(27) Taylor & Francis Group. Non-Silver & Historic Printing Processes [Visited 19 March 2018] http://www.reframingphotography.com/content/non-silver-historic-printing-processes.
(28) White, R. J. An Historical Overview of the Use of Silver in Wound Management. *Br. J. Community Nurs.* **2001**, *6* (Sup1), 3–8.
(29) Lansdown, A. Siver in Healthcare: Antimicrobial Effects and Safety in Use. *Biofunctional Text. Ski.* **2006**, *33*, 17–34.
(30) Bessey, P. Q. Wound Care. In *Total Burn Care*; Elsevier Inc., 2007; pp 127–135.
(31) Elliott, C. The Effects of Silver Dressings on Chronic and Burns Wound Healing. *Br. J. Nurs.* **2010**, *19* (15), S32–S36.
(32) Hadrup, N.; Lam, H. R. Oral Toxicity of Silver Ions, Silver Nanoparticles and Colloidal Silver - A Review. *Regul. Toxicol. Pharmacol.* **2014**, *68* (1), 1–7.
(33) Kanellos, M. No Title https://www.cnet.com/news/nanotechnology-aims-to-cure-smelly-feet/.
(34) Benn, T. M.; Westerhoff, P. Nanoparticle Silver Released into Water from Commercially Available Sock Fabrics. **2008**, 4133–4139.
(35) Haruta, M.; Kobayashi, T.; Sano, H.; Yamada, N. Novel Gold Catalysts for the Oxidation of Carbon Monoxide at a Temperature Far Below 0 °C. *Chem. Lett.* **1987**, *16* (2), 405–408.
(36) van den Berg, R.; Prieto, G.; Korpershoek, G.; van der Wal, L. I.; van Bunningen, A. J.; Lægsgaard-Jørgensen, S.; de Jongh, P. E.; de Jong, K. P. Structure Sensitivity of Cu and CuZn Catalysts Relevant to Industrial Methanol Synthesis. *Nat. Commun.* **2016**, *7*, 13057.
(37) Lok, C.-N.; Ho, C.-M.; Chen, R.; He, Q.-Y.; Yu, W.-Y.; Sun, H.; Tam, P. K.-H.; Chiu, J.-F.; Che, C.-M. Silver Nanoparticles: Partial Oxidation and Antibacterial Activities. *JBIC J. Biol. Inorg. Chem.* **2007**, *12* (4), 527–534.
(38) Olga S. Ivanova; Francis P. Zamborini. Size – Dependent Electrochemical Oxidation of Silver Nanoparticles. *J. Am. Chem. Soc.* **2010**, *132* (1), 70–72.
(39) Han, Y.; Lupitskyy, R.; Chou, T.-M.; Stafford, C. M.; Du, H.; Sukhishvili, S. Effect of Oxidation on Surface-Enhanced Raman Scattering Activity of Silver Nanoparticles: A Quantitative Correlation. *Anal. Chem.* **2011**, *83* (15), 5873–5880.
(40) Liu, X.; Madix, R. J.; Friend, C. M. Unraveling Molecular Transformations on Surfaces: A Critical Comparison of Oxidation Reactions on Coinage Metals. *Chem. Soc. Rev.* **2008**, *37* (10), 2243.
(41) Vinke, P.; van der Poel, W.; van Bekkum, H. On the Oxgen Tolerance of Noble Metal

Catalysts in Liquid Phase Alcohol Oxidations. The Influence of the Support on Catalyst Deactivation. In *Heterogeneous Catalysis and Fine Chemicals II*; Guisnet, M., Barrault, J., Bouchoule, C., Duprez, D., Pérot, G., Maurel, R., Montassier, C., Eds.; Elsevier Science, 1990; pp 390–393.

(42) Li, W. X.; Stampfl, C.; Scheffler, M. Why Is a Noble Metal Catalytically Active? The Role of the O-Ag Interaction in the Function of Silver as an Oxidation Catalyst. *Phys. Rev. Lett.* **2003**, *90* (25), 4.

(43) Luo, S. Application of Gold in the Field of Heterogeneous Catalysis. *arXiv Prepr. arXiv1411.2583* **2014**, 1–11.

(44) Hammond, C.; Forde, M. M.; Ab Rahim, M. H.; Thetford, A.; He, Q.; Jenkins, R. L.; Dimitratos, N.; Lopez-Sanchez, J. A.; Dummer, N. F.; Murphy, D. M.; et al. Direct Catalytic Conversion of Methane to Methanol in an Aqueous Medium by Using Copper-Promoted Fe-ZSM-5. *Angew. Chemie - Int. Ed.* **2012**, *51* (21), 5129–5133.

(45) Smeets, P. J.; Groothaert, M. H.; Schoonheydt, R. A. Cu Based Zeolites: A UV-Vis Study of the Active Site in the Selective Methane Oxidation at Low Temperatures. *Catal. Today* **2005**, *110* (3–4), 303–309.

(46) Twigg, M. V. "Urea-SCR Technology for DeNOx After Treatment of Diesel Exhausts." *Johnson Matthey Technol. Rev.* **2015**, *59* (3), 221–232.

(47) Wen, C.; Yin, A.; Dai, W. L. Recent Advances in Silver-Based Heterogeneous Catalysts for Green Chemistry Processes. *Appl. Catal. B Environ.* **2014**, *160–161* (1), 730–741.

(48) Kondo, M. M.; Jardim, W. F. Photodegradation of Chloroform and Urea Using Ag-Loaded Titanium Dioxide as Catalyst. *Water Res.* **1991**, *25* (7), 823–827.

(49) Linic, S.; Christopher, P.; Ingram, D. B. Plasmonic-Metal Nanostructures for Efficient Conversion of Solar to Chemical Energy. *Nat. Mater.* **2011**, *10* (12), 911–921.

(50) Lim, K. H.; Mohammad, A. B.; Yudanov, I. V.; Neyman, K. M.; Bron, M.; Claus, P.; Rösch, N. Mechanism of Selective Hydrogenation of α,β-Unsaturated Aldehydes on Silver Catalysts: A Density Functional Study. *J. Phys. Chem. C* **2009**, *113* (30), 13231–13240.

(51) Claus, P. Selective Hydrogenation of Alpha,Beta-Unsaturated Aldehydes and Other C = O and C = C Bonds Containing Compounds. *Top. Catal.* **1998**, *5*, 51–62.

(52) Gang, L.; Anderson, B. G.; van Grondelle, J.; van Santen, R. A. Low Temperature Selective Oxidation of Ammonia to Nitrogen on Silver-Based Catalysts. *Appl. Catal. B Environ.* **2003**, *40* (2), 101–110.

(53) Lefferts, L.; van Ommen, J. G.; Ross, J. R. H. The Oxidative Dehydrogenation of Methanol to Formaldehyde over Silver Catalysts in Relation to the Oxygen-Silver Interaction. *Appl. Catal.* **1986**, *23* (2), 385–402.

(54) Su, S. Catalytic Dehydrogenation of Methanol to Formadehyde on Sodium Carbonate. *Chem. Eng. Technol.* **1991**, *17*, 34–40.

(55) Rebsdat, S.; Mayer, D. Ethylene Oxide. In *Ullmann's Encyclopedia of Industrial Chemistry*; Wiley-VCH Verlag GmbH & Co. KGaA: Weinheim, Germany, 2001; pp 547–572.

(56) Brumby, A.; Braumann, P.; Zimmermann, K.; Van Den Broeck, F.; Vandevelde, T.; Goia, D.; Renner, H.; Schlamp, G.; Zimmermann, K.; Weise, W.; et al. Silver, Silver Compounds, and Silver Alloys. In *Ullmann's Encyclopedia of Industrial Chemistry*; Wiley-VCH Verlag GmbH & Co. KGaA: Weinheim, Germany, 2008; pp 1–79.

(57) Millar, G. J.; Collins, M. Industrial Production of Formaldehyde Using Polycrystalline Silver Catalyst. *Ind. Eng. Chem. Res.* **2017**, *56* (33), 9247–9265.

(58) Reuss, G.; Disteldorf, W.; Gamer, A. O.; Hilt, A. Formaldehyde. In *Ullmann's Encyclopedia of Industrial Chemistry*; Wiley-VCH Verlag GmbH & Co. KGaA: Weinheim, Germany, 2000; Vol. 15, pp 735–768.
(59) Research In China. Global and China Ethylene Oxide (EO) Industry Report, 2017-2021. 2017, pp 1–137.
(60) Kestenbaum, H.; Lange de Oliveira, A.; Schmidt, W.; Schüth, F.; Ehrfeld, W.; Gebauer, K.; Löwe, H.; Richter, T.; Lebiedz, D.; Untiedt, I.; et al. Silver-Catalyzed Oxidation of Ethylene to Ethylene Oxide in a Microreaction System. *Ind. Eng. Chem. Res.* **2002**, *41* (4), 710–719.
(61) Lou, H. H.; Chandrasekaran, J.; Smith, R. A. Large-Scale Dynamic Simulation for Security Assessment of an Ethylene Oxide Manufacturing Process. *Comput. Chem. Eng.* **2006**, *30* (6–7), 1102–1118.
(62) Stegelmann, C.; Schiødt, N. C.; Campbell, C. T.; Stoltze, P. Microkinetic Modeling of Ethylene Oxidation over Silver. *J. Catal.* **2004**, *221* (2), 630–649.
(63) Kursawe, A. Partial Oxidation of Ethene to Ethylene Oxide in Microchannel Reactors, 2009.
(64) Khan, F. Risk-Based Maintenance of Ethylene Oxide Production Facilities. *J. Hazard. Mater.* **2004**, *108* (3), 147–159.
(65) Steenland, K.; Stayner, L.; Greife, A.; Halperin, W.; Hayes, R.; Hornung, R.; Nowlin, S. Mortality among Workers Exposed to Ethylene Oxide. *N. Engl. J. Med.* **1991**, *324* (20), 1402–1407.
(66) OSHA. What is ethylene oxide? [Visited 21 December 2017] https://www.osha.gov/OshDoc/data_General_Facts/ethylene-oxide-factsheet.pdf (accessed Dec 22, 2017).
(67) Zomerdijk, J. C.; Hall, M. W. Technology for the Manufacture of Ethylene Oxide. *Catal. Rev.* **1981**, *23* (1–2), 163–185.
(68) Mendes, G. C. C.; Brandão, T. R. S.; Silva, C. L. M. Ethylene Oxide Sterilization of Medical Devices: A Review. *Am. J. Infect. Control* **2007**, *35* (9), 574–581.
(69) Wurtz, A. Ueber Das Aethylenoxyd. *Ann. der Chemie und Pharm.* **1859**, *110* (1), 125–128.
(70) McClellan, P. P. Manufacture and Uses of Ethylene Oxide and Ethylene Glycol. *Ind. Eng. Chem.* **1950**, *42* (12), 2402–2407.
(71) LeFort, T. E. Process for the Production of Ethylene Oxide. US 1998878 A, 1935.
(72) Evans, W. E.; Chipman, P. I. Process for Operating the Epoxidation of Ethylene. US 6717011 B2, 2004.
(73) Verykios, X.; Stein, F. P.; Coughlin, R. W. Influence of Metal Crystallite Size and Morphology on Selectivity and Activity of Ethylene Oxidation Catalyzed by Supported Silver. *J. Catal.* **1980**, *66* (2), 368–382.
(74) Lui, A. C.; Soo, H. Rhenium Promoted (Silver) Epoxidation Catalysts and Methods of Making and Using Them. US8546294 B2, 2013.
(75) Carvalho, M. C. N. A.; Perez, C. A.; Simão, R. A.; Passos, F. B.; Schmal, M. The Promoting Effect of Cesium on Structure and Morphology of Silver Catalysts. *An. Acad. Bras. Cienc.* **2004**, *76* (1), 19–27.
(76) Rocha, T. C. R.; Hävecker, M.; Knop-Gericke, A.; Schlögl, R. Promoters in Heterogeneous Catalysis: The Role of Cl on Ethylene Epoxidation over Ag. *J. Catal.* **2014**, *312*, 12–16.
(77) Lauritzen, A. M. Ethylene Oxide Catayst and Process for Preparing the Catalyst. US4761394, 1988.

(78) Nielsen, R. P.; La Rochelle, J. H. Catalyst for Production of Ethylene Oxide. US3962136, 1976.
(79) Van Santen, R. A.; Kuipers, H. P. C. E. The Mechanism of Ethylene Epoxidation. In *Advances in Catalysis*; 1987; Vol. 35, pp 265–321.
(80) Geenen, P. V.; Boss, H. J.; Pott, G. T. A Study of the Vapor-Phase Epoxidation of Propylene and Ethylene on Silver and Silver-Gold Alloy Catalysts. *J. Catal.* **1982**, *77* (2), 499–510.
(81) Ozbek, M. O.; Onal, I.; Van Santen, R. A. Ethylene Epoxidation Catalyzed by Chlorine-Promoted Silver Oxide. *J. Phys. Condens. Matter* **2011**, *23* (40), 404202–404209.
(82) van Maaren, W.; Schrauwen, F. J. M. Process and Apparatus for the Production of Ethylene Oxide. US2013/0072700A1, 2013.
(83) Coward, H. F.; Jones, G. W. *Limits of Flammability of Gasses and Vapors*; 1952.
(84) Özbek, M. O.; van Santen, R. A. The Mechanism of Ethylene Epoxidation Catalysis. *Catal. Letters* **2013**, *143* (2), 131–141.
(85) Orzechowski, A.; MacCormack, K. E. The Silver Catalyzed Oxidation of Ethylene: I. Slow Processes on the Catalyst Surface. *Can. J. Chem.* **1954**, *32* (4), 388–398.
(86) West, T. J.; West, J. P. Silver Surface Catalysts and Process of Producing Same. US2463228, 1949.
(87) Dellamorte, J. C.; Lauterbach, J.; Barteau, M. A. Palladium-Silver Bimetallic Catalysts with Improved Activity and Selectivity for Ethylene Epoxidation. *Appl. Catal. A Gen.* **2011**, *391* (1–2), 281–288.
(88) Dellamorte, J. C.; Lauterbach, J.; Barteau, M. a. Rhenium Promotion of Ag and Cu–Ag Bimetallic Catalysts for Ethylene Epoxidation. *Catal. Today* **2007**, *120* (2), 182–185.
(89) Jankowiak, J.; Barteau, M. Ethylene Epoxidation over Silver and Copper–Silver Bimetallic Catalysts: II. Cs and Cl Promotion. *J. Catal.* **2005**, *236* (2), 379–386.
(90) Nakatsuji, H.; Hu, Z.; Nakai, H. Theoretical Studies on the Catalytic Activity of Ag Surface for the Oxidation of Olefins. *Int. J. Quantum Chem.* **1997**, *65*, 839–855.
(91) Jankowiak, J. T.; Barteau, M. A. Ethylene Epoxidation over Silver and Copper–Silver Bimetallic Catalysts: I. Kinetics and Selectivity. *J. Catal.* **2005**, *236* (2), 366–378.
(92) Nguyen, N. L.; De Gironcoli, S.; Piccinin, S. Ag-Cu Catalysts for Ethylene Epoxidation: Selectivity and Activity Descriptors. *J. Chem. Phys.* **2013**, *138* (18).
(93) Piccinin, S.; Zafeiratos, S.; Stampfl, C.; Hansen, T. W.; Hävecker, M.; Teschner, D.; Bukhtiyarov, V. I.; Girgsdies, F.; Knop-Gericke, A.; Schlögl, R.; et al. Alloy Catalyst in a Reactive Environment: The Example of Ag-Cu Particles for Ethylene Epoxidation. *Phys. Rev. Lett.* **2010**, *104* (3), 1–4.
(94) Lei, Y.; Mehmood, F.; Lee, S.; Greeley, J.; Lee, B.; Seifert, S.; Winans, R. E.; Elam, J. W.; Meyer, R. J.; Redfern, P. C.; et al. Increased Silver Activity for Direct Propylene Epoxidation via Subnanometer Size Effects. *Science (80-.).* **2010**, *328* (5975), 224–228.
(95) Kulkarni, A.; Bedolla-Pantoja, M.; Singh, S.; Lobo, R. F.; Mavrikakis, M.; Barteau, M. A. Reactions of Propylene Oxide on Supported Silver Catalysts: Insights into Pathways Limiting Epoxidation Selectivity. *Top. Catal.* **2012**, *55* (1–2), 3–12.
(96) Gash, V. W. Procss for the Liquid Phase Direct Oxidation of Olefins to Olefin Oxides, 1962.
(97) Sachtler, W. M. H.; Backx, C.; Van Santen, R. A. On the Mechanism of Ethylene Epoxidation. *Catal. Rev.* **1981**, *23* (1–2), 127–149.
(98) Cheng, S.; Clearfield, A. Oxidation of Ethylene Catalyzed by Silver Supported on

Zirconium Phosphate: Particle Size and Support Effect. *J. Catal.* **1985**, *94* (2), 455–467.
(99) Che, M.; Bennett, C. O. The Influence of Particle Size on the Catalytic Properties of Supported Metals. In *Advances in Catalysis*; 1989; Vol. 36, pp 55–172.
(100) Shriver, D. F.; Atkins, P. W. Trends in Chemical Properties. In *Inorganic Chemistry, fourth edition*; 2006; pp 443–444.
(101) Baxter, R. J.; Hu, P. Insight into Why the Langmuir-Hinshelwood Mechanism Is Generally Preferred. *J. Chem. Phys.* **2002**, *116* (11), 4379–4381.
(102) Chorkendorff, I.; Niemandsverdriet, J. W. Kinetics. In *Concepts of Modern Catalysis And Kinetics*; 2006; pp 21–78.
(103) van Santen, R. A.; van Leeuwen, P. W. N. M.; Moulijn, J. A.; Averill, B. A. Chemical Kinetics of Catalyzed Reactions. In *Catalysis: An Integrated Approach*; Elsevier Science, 1999; pp 81–105.
(104) Bartholomew, C. H. Mechanisms of Catalyst Deactivation. *Appl. Catal. A Gen.* **2001**, *212* (1–2), 17–60.
(105) Mars, P.; van Krevelen, D. W. Oxidations Carried out by Means of Vanadium Oxide Catalysts. *Chem. Eng. Sci.* **1954**, *3*, 41–59.
(106) Chorkendorff, I.; Niemandsverdriet, J. W. Petrochemistry: Reactions of Small Olefins, Student Edition. In *Concepts of Modern Catalysis And Kinetics*; 2006; pp 370–376.
(107) van Santen, R. A.; van Leeuwen, P. W. N. M.; Moulijn, J. A.; B.A., A. Heterogeneous Catalysis. In *Catalysis: An Integrated Approach*; Elsevier Science, 1999; pp 209–287.
(108) Aho, A.; Eränen, K.; Lemus-Yegres, L. J.; Voss, B.; Gabrielsson, A.; Salmi, T.; Murzin, D. Y. Ethylene Epoxidation over Supported Silver Catalysts - Influence of Catalyst Pretreatment on Conversion and Selectivity. *J. Chem. Technol. Biotechnol.* **2018**, *93* (6), 1549–1557.
(109) Chan, M. S. C.; Marek, E.; Scott, S. A.; Dennis, J. S. Chemical Looping Epoxidation. *J. Catal.* **2018**, *359*, 1–7.
(110) Van Santen, R. A.; Kuipers, H. P. C. E. The Mechanism of Ethylene Epoxidation. In *Advances in Catalysis*; 1987; Vol. 23, pp 265–321.
(111) Christopher, P.; Linic, S. Engineering Selectivity in Heterogeneous Catalysis: Ag Nanowires as Selective Ethylene Epoxidation Catalysts. *J. Am. Chem. Soc.* **2008**, *130* (34), 11264–11265.
(112) Verykios, X. E.; Stein, F. P.; Coughlin, R. W. Oxidation of Ethylene over Silver: Adsorption, Kinetics, Catalyst. *Catal. Rev.* **1980**, *22* (2), 197–234.
(113) Christopher, P.; Linic, S. Shape- and Size-Specific Chemistry of Ag Nanostructures in Catalytic Ethylene Epoxidation. *ChemCatChem* **2010**, *2* (1), 78–83.
(114) Bertole, C. J.; Mims, C. a. Dynamic Isotope Tracing: Role of Subsurface Oxygen in Ethylene Expoxidation on Silver. *J. Catal.* **1999**, *184*, 224.
(115) Bukhtiyarov, V. I.; Kaichev, V. V. The Combined Application of XPS and TPD to Study of Oxygen Adsorption on Graphite-Supported Silver Clusters. *J. Mol. Catal. A Chem.* **2000**, *158* (1), 167–172.
(116) Kilty, P. A.; Sachtler, W. M. H. The Mechanism of the Selective Oxidation of Ethylene To Ethylene. *Catal. Rev. Sci. Eng.* **1974**, *10* (September 2012), 1–16.
(117) Carter, E. A.; Goddard, W. A. The Surface Atomic Oxyradical Mechanism for Ag-Catalyzed Olefin Epoxidation. *J. Catal.* **1988**, *112* (1), 80–92.
(118) Grant, R. B.; Lambert, R. M. Basic Studies of the Oxygen Surface Chemistry of Silver: Chemisorbed Atomic and Molecular Species on Pure Ag(111). *Surf. Sci.* **1984**, *146* (1),

256–268.
(119) Grant, R. B.; Lambert, R. M. A Single Crystal Study of the Silver-Catalysed Selective Oxidation and Total Oxidation of Ethylene. *J. Catal.* **1985**, *92* (2), 364–375.
(120) Rigas, N. C.; Svoboda, G. D.; Gleaves, J. T. Activation of Silver Powder for Ethylene Epoxidation at Vacuum and Atmospheric Pressures. In *Catalytic Selective Oxidation*; 1993; pp 183–203.
(121) Bernardo, C. G. P. M.; Gomes, J. A. N. F. The Adsorption of Ethylene on the (110) Surfaces of Copper, Silver and Platinum: A DFT Study. *J. Mol. Struct. THEOCHEM* **2002**, *582* (1–3), 159–169.
(122) Linic, S.; Barteau, M. A. Construction of a Reaction Coordinate and a Microkinetic Model for Ethylene Epoxidation on Silver from DFT Calculations and Surface Science Experiments. *J. Catal.* **2003**, *214* (2), 200–212.
(123) Linic, S.; Barteau, M. A. Formation of a Stable Surface Oxametallacycle That Produces Ethylene Oxide. *J. Am. Chem. Soc.* **2002**, *124* (2), 310–317.
(124) Linic, S.; Medlin, J. W.; Barteau, M. A. Synthesis of Oxametallacycles from 2-Iodoethanol on Ag(111) and the Structure Dependence of Their Reactivity. *Langmuir* **2002**, *18* (13), 5197–5204.
(125) Ozbek, M. O.; Onal, I.; van Santen, R. A. Why Silver Is the Unique Catalyst for Ethylene Epoxidation. *J. Catal.* **2011**, *284* (2), 230–235.
(126) Zhu, L.; Zhang, W.; Zhu, J.; Cheng, D. Mechanistic Insight into the Facet-Dependent Selectivity of Ethylene Epoxidation on Ag Nanocatalysts. *Appl. Catal. A Gen.* **2017**, *538*, 27–36.
(127) da Silva, A. G. M.; Rodrigues, T. S.; Wang, J.; Yamada, L. K.; Alves, T. V.; Ornellas, F. R.; Ando, R. A.; Camargo, P. H. C. The Fault in Their Shapes: Investigating the Surface-Plasmon-Resonance-Mediated Catalytic Activities of Silver Quasi-Spheres, Cubes, Triangular Prisms, and Wires. *Langmuir* **2015**, *31* (37), 10272–10278.
(128) Jones, G. S.; Mavrikakis, M.; Barteau, M. A.; Vohs, J. M. First Synthesis, Experimental and Theoretical Vibrational Spectra of an Oxametallacycle on a Metal Surface. *J. Am. Chem. Soc.* **1998**, *120* (13), 3196–3204.
(129) Wu, G.; Stacchiola, D.; Collins, M.; Tysoe, W. T. The Adsorption and Reaction of Acetaldehyde on Clean Ag (111). *Surf. Rev. Lett.* **2000**, *07* (03), 271–275.
(130) Akella, L. M.; Lee, H. H. Selectivity Characterization of Ethylene Oxidation Reactions: Oxygen Chemisorption. *J. Catal.* **1984**, *86* (2), 465–472.
(131) Ozbek, M. O.; Onal, I.; Van Santen, R. A. Effect of Surface and Oxygen Coverage on Ethylene Epoxidation. *Top. Catal.* **2012**, *55* (11–13), 710–717.
(132) Lee, J. K.; Verykios, X. E.; Pitchai, R. Support and Crystallite Size Effects in Ethylene Oxidation Catalysis. *Appl. Catal.* **1989**, *50* (1), 171–188.
(133) Bukhtiyarov, V. I.; Prosvirin, I. P.; Kvon, R. I.; Goncharova, S. N.; Bal'zhinimaev, B. S. XPS Study of the Size Effect in Ethene Epoxidation on Supported Silver Catalysts. *J. Chem. Soc. Faraday Trans.* **1997**, *93* (13), 2323–2329.
(134) Sorokin, A. M.; Prosvirin, I. P.; Demidov, D. V.; Bukhtiyarov, V. I. Size Effect in Ethylene Oxidation over Silver Nanoparticles Supported on HOPG. In *Procedings of the International Conference Nanomaterials: Applications and Properties*; 2013; Vol. 2.
(135) Verykios, X. .; Stein, F. P.; Coughlin, R. W. Influence of Metal Cyrstallite Size and Morphology on Selectivity and Activiy of Ethylene Oxidation Catalyzed by Supported Silver. *J. Catal.* **1980**, *66*, 368–382.

(136) Bukhtiyarov, V. I.; Carley, A. F.; Dollard, L. A.; Roberts, M. W. XPS Study of Oxygen Adsorption on Supported Silver : Effect of Particle Size. *Surf. Sci.* **1997**, *381*, L605–L608.
(137) Van Santen, R. A. Complementary Structure Sensitive and Insensitive Catalytic Relationships. *Acc. Chem. Res.* **2009**, *42* (1), 57–66.
(138) den Breejen, J. P.; Radstake, P. B.; Bezemer, G. L.; Bitter, J. H.; Frøseth, V.; Holmen, A.; de Jong, K. P. On the Origin of the Cobalt Particle Size Effects in Fischer−Tropsch Catalysis. *J. Am. Chem. Soc.* **2009**, *131* (20), 7197–7203.
(139) Bezemer, G. L.; Bitter, J. H.; Kuipers, H. P. C. E.; Oosterbeek, H.; Holewijn, J. E.; Xu, X.; Kapteijn, F.; van Dillen, A. J.; de Jong, K. P. Cobalt Particle Size Effects in the Fischer−Tropsch Reaction Studied with Carbon Nanofiber Supported Catalysts. *J. Am. Chem. Soc.* **2006**, *128* (12), 3956–3964.
(140) Coq, B.; Figueras, F. Structure–Activity Relationships in Catalysis by Metals: Some Aspects of Particle Size, Bimetallic and Supports Effects. *Coord. Chem. Rev.* **1998**, *178–180*, 1753–1783.
(141) Van Hardeveld, R.; Hartog, F. The Statistics of Surface Atoms and Surface Sites on Metal Crystals. *Surf. Sci.* **1969**, *15* (2), 189–230.
(142) Somorjai, G. A.; Carrazza, J. Structure Sensitivity of Catalytic Reactions. *Ind. Eng. Chem. Fundam.* **1986**, *25* (1), 63–69.
(143) Torres, D.; Lopez, N.; Illas, F.; Lambert, R. M. Why Copper Is Intrinsically More Selective than Silver in Alkene Epoxidation: Ethylene Oxidation on Cu(111) versus Ag(111). *J. Am. Chem. Soc.* **2005**, *127* (31), 10774–10775.
(144) Lu, J.; Bravo-Suárez, J. J.; Takahashi, A.; Haruta, M.; Oyama, S. T. In Situ UV-Vis Studies of the Effect of Particle Size on the Epoxidation of Ethylene and Propylene on Supported Silver Catalysts with Molecular Oxygen. *J. Catal.* **2005**, *232* (1), 85–95.
(145) Bond, G. C. The Origins of Particle Size Effects in Heterogeneous Catalysis. *Surf. Sci.* **1985**, *156* (PART 2), 966–981.
(146) van Helden, P.; Ciobîcă, I. M.; Coetzer, R. L. J. The Size-Dependent Site Composition of FCC Cobalt Nanocrystals. *Catal. Today* **2016**, *261*, 48–59.
(147) Sajkowski, D. J.; Boudart, M. Structure Sensitivity of the Catalytic Oxidation of Ethene by Silver. *Catal. Rev.* **1987**, *29* (4), 325–360.
(148) van Lent, R.; Auras, S. V.; Cao, K.; Walsh, A. J.; Gleeson, M. A.; Juurlink, L. B. F. Site-Specific Reactivity of Molecules with Surface Defects-the Case of H2 Dissociation on Pt. *Science (80-.).* **2019**, *363* (January), 155–157.
(149) Bedford, N.; Dablemont, C.; Viau, G.; Chupas, P.; Petkov, V. 3-D Structure of Nanosized Catalysts by High-Energy X-Ray Diffraction and Reverse Monte Carlo Simulations: Study of Ru. *J. Phys. Chem. C* **2007**, *111* (49), 18214–18219.
(150) Quek, X.-Y.; Pestman, R.; van Santen, R. A.; Hensen, E. J. M. Structure Sensitivity in the Ruthenium Nanoparticle Catalyzed Aqueous-Phase Fischer–Tropsch Reaction. *Catal. Sci. Technol.* **2014**, *4* (10), 3510–3523.
(151) Vilé, G.; Baudouin, D.; Remediakis, I. N.; Copéret, C.; Lõpez, N.; Pérez-Ramírez, J. Silver Nanoparticles for Olefin Production: New Insights into the Mechanistic Description of Propyne Hydrogenation. *ChemCatChem* **2013**, *5* (12), 3750–3759.
(152) Mavrikakis, M.; Stoltze, P.; Nørskov, J. K. Making Gold Less Noble. *Catal. Letters* **2000**, *64* (2–4), 101–106.
(153) Barmparis, G. D.; Lodziana, Z.; Lopez, N.; Remediakis, I. N. Nanoparticle Shapes by

Using Wulff Constructions and First-Principles Calculations. *J. Nanotechnol.* **2015**, *6*, 361–368.

(154) Parker, S. C.; Campbell, C. T. Reactivity and Sintering Kinetics of Au / TiO 2 (110) Model Catalysts : Particle Size Effects. **2007**, *44* (June), 3–13.

(155) Lee, W.; Cem Akatay, M.; Stach, E. A.; Ribeiro, F. H.; Nicholas Delgass, W. Reproducible Preparation of Au/TS-1 with High Reaction Rate for Gas Phase Epoxidation of Propylene. *J. Catal.* **2012**, *287*, 178–189.

(156) Sietsma, J. R. A.; Meeldijk, J. D.; den Breejen, J. P.; Versluijs-Helder, M.; van Dillen, A. J.; de Jongh, P. E.; de Jong, K. P. The Preparation of Supported NiO and Co3O4 Nanoparticles by the Nitric Oxide Controlled Thermal Decomposition of Nitrates. *Angew. Chemie* **2007**, *119* (24), 4631–4633.

(157) Goncharova, S. N.; Paukshtis, E. A.; Bal'zhinimaev, B. S. Size Effects in Ethylene Oxidation on Silver Catalysts. Influence of Support and Cs Promoter. *Appl. Catal. A Gen.* **1995**, *126* (1), 67–84.

(158) Jiang, J.; Xu, T.; Li, Y.; Lei, X.; Zhang, H.; Evans, D. G.; Sun, X.; Duan, X. A Deep Investigation of the Thermal Decomposition Process of Supported Silver Catalysts. *Bull. Korean Chem. Soc.* **2014**, *35* (6), 1832–1836.

(159) Van den Hoek, P. J.; Baerends, E. J.; Van Santen, R. a. Ethylene Epoxidation on Silver(110): The Role of Subsurface Oxygen. *J. Phys. Chem.* **1989**, *93* (17), 6469–6475.

(160) Argyle, M.; Bartholomew, C. Heterogeneous Catalyst Deactivation and Regeneration: A Review. *Catalysts* **2015**, *5* (1), 145–269.

(161) Julkapli, N. M.; Bagheri, S. Graphene Supported Heterogeneous Catalysts: An Overview. *Int. J. Hydrogen Energy* **2015**, *40* (2), 948–979.

(162) van Santen, R. A.; van Leeuwen, P. W. N. M.; Moulijn, J. A.; Averill, B. A. Preparation of Catalyst Supports, Zeolites and Mesoporous Materials. In *Catalysis: An Integrated Approach*; Elsevier Science, 1999; pp 433–458.

(163) Giraldo, L. F.; López, B. L.; Pérez, L.; Urrego, S.; Sierra, L.; Mesa, M. Mesoporous Silica Applications. *Macromol. Symp.* **2007**, *258*, 129–141.

(164) Evonik. *Aerosil - Fumed Silica: Technical Overview*; 2015.

(165) Digne, M.; Sautet, P.; Raybaud, P.; Euzen, P.; Toulhoat, H. Hydroxyl Groups on γ-Alumina Surfaces: A DFT Study. *J. Catal.* **2002**, *211* (1), 1–5.

(166) Zamora, M.; Cordoba, A. A Study of Surface Hydroxyl Groups on .Gamma.-Alumina. *J. Phys. Chem.* **1978**, *82* (5), 584–588.

(167) Busca, G. The Surface of Transitional Aluminas: A Critical Review. *Catal. Today* **2014**, *226*, 2–13.

(168) Lefèvre, G.; Duc, M.; Lepeut, P.; Caplain, R.; Fédoroff, M. Hydration of γ-Alumina in Water and Its Effects on Surface Reactivity. *Langmuir* **2002**, *18* (20), 7530–7537.

(169) McHale, J. M.; Auroux, A.; Perrotta, A. J.; Navrotsky, A. Surface Energies and Thermodynamic Phase Stability in Nanocrystalline Aluminas. *Science (80-.).* **1997**, *277* (5327), 788–789.

(170) Nguefack, M.; Popa, A. F.; Rossignol, S.; Kappenstein, C. Preparation of Alumina through a Sol–Gel Process. Synthesis, Characterization, Thermal Evolution and Model of Intermediate Boehmite. *Phys. Chem. Chem. Phys.* **2003**, *5* (19), 4279–4289.

(171) Smit, W.; Holten, C. L. M. Zeta-Potential and Radiotracer Adsorption Measurements on EFG α-Al2O3 Single Crystals in NaBr Solutions. *J. Colloid Interface Sci.* **1980**, *78* (1), 1–14.

(172) Pines, H.; Haag, W. O. Alumina: Catalyst and Support. I. Alumina, Its Intrinsic Acidity and Catalytic Activity 1. *J. Am. Chem. Soc.* **1960**, *82* (10), 2471–2483.
(173) Donoeva, B.; Masoud, N.; De Jongh, P. E. Carbon Support Surface Effects in the Gold-Catalyzed Oxidation of 5-Hydroxymethylfurfural. *ACS Catal.* **2017**, *7* (7), 4581–4591.
(174) Coq, B.; Dutartre, R.; Figueras, F.; Tazi, T. Particle Size, Precursor, and Support Effects in the Hydrogenolysis of Alkanes over Supported Rhodium Catalysts. *J. Catal.* **1990**, *122* (2), 438–447.
(175) Huber, G. W.; Guymon, C. G.; Conrad, T. L.; Stephenson, B. C.; Bartholomew, C. H. Hydrothermal Stability of Co / SiO2 Fischer-Tropsch Synthesis Catalysts. In *Catalyst Deactivation 2001*; Elsevier Masson SAS, 2001; Vol. 139, pp 423–430.
(176) Spencer, M. S. Models of Strong Metal-Support Interaction (SMSI) in Pt on TiOp Catalysts. **1985**, *223*, 216–223.
(177) Mao, C.-F.; Albert Vannice, M. High Surface Area α-Aluminas III. Oxidation of Ethylene, Ethylene Oxide, and Acetaldehyde over Silver Dispersed on High Surface Area α-Alumina. *Appl. Catal. A Gen.* **1995**, *122* (1), 61–76.
(178) Murrell, L. L.; Grenoble, D. C.; DeLuca, J. P. Process for Preparing Ultra-Stable, High Surface Area Alpha-Alumina. US4169883, 1976.
(179) Kelly, A. C.; Alto, P.; Ducote, H. J.; Saratoga; Barsotti, L. R. Method for Preparing an Alpha Alumina Catalyst Support. **1968**, 1–7.
(180) Linic, S.; Christopher, P. Epoxidation Catalyst and Process. US7820840B2, 2010.
(181) Monsanto Chemicals. Improvements in or Relating to Process of Making Ethylene Oxide, and the Improved Catalysts Suitable for Use in Said Process. GB627987A, 1946.
(182) Wattimena, F. Silver Catalyst. US3563914, 1971.
(183) Łodziana, Z.; Nørskov, J. K.; Stoltze, P. The Stability of the Hydroxylated (0001) Surface of α-Al[Sub 2]O[Sub 3]. *J. Chem. Phys.* **2003**, *118* (24), 11179.
(184) Rojluechai, S.; Chavadej, S.; Schwank, J. W.; Meeyoo, V. Catalytic Activity of Ethylene Oxidation over Au, Ag and Au-Ag Catalysts: Support Effect. *Catal. Commun.* **2007**, *8* (1), 57–64.
(185) Petitto, C.; Delahay, G. A New Way for Silver Alumina Catalyst Preparation. *Catal. Letters* **2012**, *142* (4), 433–438.
(186) Raharjo, P.; Ishizaki, C.; Ishizaki, K. Surface Hydration States of High Purity .ALPHA.-Al2O3 Powders. *J. Ceram. Soc. Japan* **2000**, *108* (1257), 449–455.
(187) Van Santen, R. A. *Modern Heterogeneous Catalysis: An Introduction*; Wiley-VCH Verlag GmbH & Co. KGaA, 2017.
(188) Yong, Y. S.; Kennedy, E. M.; Cant, N. W. Oxide Catalysed Reactions of Ethylene Oxide under Conditions Relevant to Ethylene Epoxidation over Supported Silver. *Appl. Catal.* **1991**, *76* (1), 31–48.
(189) Wu, J. C.; Harriott, P. The Effect of Crystallite Size on the Activity and Selectivity of Silver Catalysts. *J. Catal.* **1975**, *39* (3), 395–402.
(190) Campbell, C. T. The Selective Epoxidation of Ethylene Catalyzed by Ag (111): A Comparison with Ag (110). *J. Catal.* **1985**, *444*, 436–444.
(191) Campbell, C. T. Surface Science Study of Selective Ethylene Epoxidation Catalyzed by the Ag(110) Surface: Structural Sensitivity. *J. Vac. Sci. Technol. A Vacuum, Surfaces, Film.* **1984**, *2* (2), 1024–1027.
(192) Mastikhin, V. M.; Goncharova, S. N.; Tapilin, V. M.; Terskikh, V. V.; Balzhinimaev, B. S. Effect of Particle Size upon Catalytic and Electronic Properties of Supported Ag

Catalysts: Combined Catalytic, 109Ag NMR and Quantum Chemistry Studies. *J. Mol. Catal. A Chem.* **1995**, *96* (2), 175–179.
(193) Bukhtiyarov, V. I.; Havecker, M.; Kaichev, V. V; Knop-Gericke, A.; Mayer, R. W.; Schlogl, R. Atomic Oxygen Species on Silver: Photoelectron Spectroscopy and x-Ray Absorption Studies. *Phys. Rev. B* **2003**, *67* (23), 235422.
(194) Kim, S.-G.; Seo, Y.-G.; Cho, Y.-J.; Shin, J.-S.; Gil, S.-C.; Lee, W.-M. Optimization of Emulsion Polymerization for Submicron-Sized Polymer Colloids towards Tunable Synthetic Opals. *Bull. Korean Chem. Soc.* **2010**, *31* (7), 1891–1896.
(195) Özbek, M. O.; Önal, I.; van Santen, R. A. Ethylene Epoxidation Catalyzed by Silver Oxide. *ChemCatChem* **2011**, *3* (1), 150–153.
(196) Lee, J. K.; Verykios, X. E.; Pitchai, R. Support Participation in Chemistry of Ethylene Oxidation on Silver Catalysts. *Appl. Catal.* **1988**, *44* (C), 223–237.
(197) Casavola, M.; Hermannsdörfer, J.; de Jonge, N.; Dugulan, A. I.; de Jong, K. P. Fabrication of Fischer-Tropsch Catalysts by Deposition of Iron Nanocrystals on Carbon Nanotubes. *Adv. Funct. Mater.* **2015**, *25* (33), 5309–5319.
(198) Toupance, T.; Kermarec, M.; Louis, C. Metal Particle Size in Silica-Supported Copper Catalysts. Influence of the Conditions of Preparation and of Thermal Pretreatments. *J. Phys. Chem. B* **2000**, *104* (5), 965–972.
(199) Munnik, P.; Wolters, M.; Gabrielsson, A.; Pollington, S. D.; Headdock, G.; Bitter, J. H.; De Jongh, P. E.; De Jong, K. P. Copper Nitrate Redispersion to Arrive at Highly Active Silica-Supported Copper Catalysts. *J. Phys. Chem. C* **2011**, *115* (30), 14698–14706.
(200) Pourmortazavi, S. M.; Hajimirsadeghi, S. S.; Kohsari, I.; Fareghi Alamdari, R.; Rahimi-Nasrabadi, M. Determination of the Optimal Conditions for Synthesis of Silver Oxalate Nanorods. *Chem. Eng. Technol.* **2008**, *31* (10), 1532–1535.
(201) Boldyrev, V. V. Thermal Decomposition of Silver Oxalate. *Thermochim. Acta* **2002**, *388* (1–2), 63–90.
(202) Fiorucci, A. R.; Saran, L. M.; Cavalheiro, É. T. G.; Neves, E. A. Thermal Stability and Bonding in the Silver Complexes of Ethylenediaminetetraacetic Acid. *Thermochim. Acta* **2000**, *356* (1–2), 71–78.
(203) Plessers, E.; Stassen, I.; Sree, S. P.; Janssen, K. P. F.; Yuan, H.; Martens, J.; Hofkens, J.; De Vos, D.; Roeffaers, M. B. J. Resolving Interparticle Heterogeneities in Composition and Hydrogenation Performance between Individual Supported Silver on Silica Catalysts. *ACS Catal.* **2015**, *5* (11), 6690–6695.
(204) Hoekstra, J.; Beale, A. M.; Soulimani, F.; Versluijs-Helder, M.; Geus, J. W.; Jenneskens, L. W. Shell Decoration of Hydrothermally Obtained Colloidal Carbon Spheres with Base Metal Nanoparticles. *New J. Chem.* **2015**, *39* (8), 6593–6601.
(205) Mock, J. J.; Barbic, M.; Smith, D. R.; Schultz, D. A.; Schultz, S. Shape Effects in Plasmon Resonance of Individual Colloidal Silver Nanoparticles. *J. Chem. Phys.* **2002**, *116* (15), 6755–6759.
(206) Nijhuis, T. A. *Towards a New Propene Epoxidation Process*; 1997.
(207) Harriott, P. The Oxidation of Ethylene Using Silver on Different Supports. *J. Catal.* **1971**, *21* (1), 56–65.
(208) Amendola, V.; Bakr, O. M.; Stellacci, F. A Study of the Surface Plasmon Resonance of Silver Nanoparticles by the Discrete Dipole Approximation Method: Effect of Shape, Size, Structure, and Assembly. *Plasmonics* **2010**, *5* (1), 85–97.
(209) Liebsch, A. Surface-Plasmon Dispersion and Size Dependence of Mie Resonance:

Silver versus Simple Metals. *Phys. Rev. B* **1993**, *48* (15), 11317–11328.
(210) Leiga, A. G. Decomposition of Silver Oxalate. I. Microscopic Observations of Partially Decomposed Crystals. *J. Phys. Chem.* **1966**, *70* (10), 3254–3259.
(211) Macdonald, J. Y. Thermal Decomposition of Silver Oxalate. *Nature* **1936**, *137* (3456), 152–153.
(212) van den Reijen, J. E.; Kanungo, S.; Welling, T. A. J.; Versluijs-Helder, M.; Nijhuis, T. A.; de Jong, K. P.; de Jongh, P. E. Preparation and Particle Size Effects of Ag/a-Al2O3 Catalysts for Ethylene Epoxidation. *J. Catal.* **2017**, *356*, 65–74.
(213) Wichner, N. M.; Beckers, J.; Rothenberg, G.; Koller, H. Preventing Sintering of Au and Ag Nanoparticles in Silica-Based Hybrid Gels Using Phenyl Spacer Groups. *J. Mater. Chem.* **2010**, *20* (19), 3840–3847.
(214) Fogler, H. S. *Elements of Chemical Reaction Engineering*, 3rd ed.; Amundson, N. R., Ed.; Prentice Hall International, 1999.
(215) Cundy, C. S.; Cox, P. A. The Hydrothermal Synthesis of Zeolites: History and Development from the Earliest Days to the Present Time. *Chem. Rev.* **2003**, *103* (3), 663–701.
(216) Kresge, C. T.; Leonowicz, M. E.; Roth, W. J.; Vartuli, J. C.; Beck, J. S. Ordered Mesoporous Molecular Sieves Synthesized by a Liquid-Crystal Template Mechanism. *Nature* **1992**, *359* (6397), 710–712.
(217) Zhao, D.; Huo, Q.; Feng, J.; Chmelka, B. F.; Stucky, G. D. Nonionic Triblock and Star Diblock Copolymer and Oligomeric Surfactant Syntheses of Highly Ordered, Hydrothermally Stable, Mesoporous Silica Structures. *J. Am. Chem. Soc.* **1998**, *120* (24), 6024–6036.
(218) Zhao, D.; Wan, Y.; Zhou, W. Synthesis Approach of Mesoporous Molecular Sieves. In *Ordered Mesoporous Materials*; Wiley-VCH Verlag GmbH & Co. KGaA, 2013; pp 5–54.
(219) Tang, F.; Li, L.; Chen, D. Mesoporous Silica Nanoparticles: Synthesis, Biocompatibility and Drug Delivery. *Adv. Mater.* **2012**, *24* (12), 1504–1534.
(220) Gallis, K. W.; Araujo, J. T.; Duff, K. J.; Moore, J. G.; Landry, C. C. The Use of Mesoporous Silica in Liquid Chromatography. *Adv. Mater.* **1999**, *11* (17), 1452–1455.
(221) Davis, M. E. Ordered Porous Materials for Emerging Applications. *Nature* **2002**, *417* (6891), 813–821.
(222) Maschmeyer, T.; Rey, F.; Sankar, G.; Thomas, J. M. Heterogeneous Catalysts Obtained by Grafting Metallocene Complexes onto Mesoporous Silica. *Nature*, 1995, *378*, 159–162.
(223) Prieto, G.; Shakeri, M.; de Jong, K. P.; de Jongh, P. E. Quantitative Relationship between Support Porosity and the Stability of Pore-Confined Metal Nanoparticles Studied on CuZnO/SiO2 Methanol Synthesis Catalysts. *ACS Nano* **2014**, *8* (3), 2522–2531.
(224) Prieto, G.; Meeldijk, J. D.; de Jong, K. P.; de Jongh, P. E. Interplay between Pore Size and Nanoparticle Spatial Distribution: Consequences for the Stability of CuZn/SiO2 Methanol Synthesis Catalysts. *J. Catal.* **2013**, *303*, 31–40.
(225) Ravikovitch, P. I.; Neimark, A. V. Characterization of Nanoporous Materials. *Colloids Surfaces A Physicochem. Eng. Asp.* **2001**, *187–188*, 11–21.
(226) Cychosz, K.; Guo, X.; Fan, W.; Cimino, R. Characterization of the Pore Structure of Three-Dimensionally Ordered Mesoporous Carbons Using High Resolution Gas Sorption. *Langmuir* **2012**, *28* (34), 12647–12654.
(227) Zhao, D.; Wan, Y.; Zhou, W. Mechanisms for Formation of Mesoporous Materials. In

Ordered Mesoporous Materials; 2013; pp 55–116.
(228) Yang, P.; Zhao, D.; Margolese, D. Block Copolymer Templating Syntheses of Mesoporous Metal Oxides with Large Ordering Lengths and Semicrystalline Framework. *Chem. Mater.* **1999**, No. 21, 2813–2826.
(229) Laine, R. M.; Marchal, J. C.; Sun, H. P.; Pan, X. Q. Nano-α-Al2O3 by Liquid-Feed Flame Spray Pyrolysis. *Nat. Mater.* **2006**, *5* (9), 710–712.
(230) Lefebvre, L. P.; Banhart, J.; Dunand, D. C. Porous Metals and Metallic Foams: Current Status and Recent Developments. *Adv. Eng. Mater.* **2008**, *10* (9), 775–787.
(231) Abdullah, M.; Iskandar, F.; Shibamoto, S.; Ogi, T.; Okuyama, K. Preparation of Oxide Particles with Ordered Macropores by Colloidal Templating and Spray Pyrolysis. *Acta Mater.* **2004**, *52* (17), 5151–5156.
(232) Nishihara, H.; Kyotani, T. Templated Nanocarbons for Energy Storage. *Adv. Mater.* **2012**, *24* (33), 4473–4498.
(233) Petkovich, N. D.; Stein, A. Controlling Macro- and Mesostructures with Hierarchical Porosity through Combined Hard and Soft Templating. *Chem. Soc. Rev.* **2013**, *42* (9), 3721–3739.
(234) Velev, O. D.; Jede, T. A.; Lobo, R. F.; Lenhoff, A. M. Porous Silica via Colloidal Crystallization. *Nature* **1997**, *389* (6650), 447–448.
(235) Stein, A. Sphere Templating Methods for Periodic Porous Solids. *Microporous Mesoporous Mater.* **2001**, *44–45*, 227–239.
(236) Stein, A.; Schroden, R. C. Colloidal Crystal Templating of Three-Dimensionally Ordered Macroporous Solids: Materials for Photonics and Beyond. *Curr. Opin. Solid State Mater. Sci.* **2001**, *5* (6), 553–564.
(237) Chen, X.; Li, Z.; Ye, J.; Zou, Z. Forced Impregnation Approach to Fabrication of Large-Area, Three-Dimensionally Ordered Macroporous Metal Oxides. *Chem. Mater.* **2010**, *22* (12), 3583–3585.
(238) Yi, G. R.; Moon, J. H.; Yang, S. M. Ordered Macroporous Particles by Colloidal Templating. *Chem. Mater.* **2001**, *13* (8), 2613–2618.
(239) Yan, H.; Blanford, C. F.; Holland, B. T.; Smyrl, W. H.; Stein, A. General Synthesis of Periodic Macroporous Solids by Templated Salt Precipitation and Chemical Conversion. *Chem. Mater.* **2000**, *12* (4), 1134–1141.
(240) Rudisill, S. G.; Wang, Z.; Stein, A. Maintaining the Structure of Templated Porous Materials for Reactive and High-Temperature Applications. *Langmuir* **2012**, *28* (19), 7310–7324.
(241) Mitsuhata, M.; Watanabe, F.; Kumazawa, T. Silver Catalyst for Production of Ethylene Oxide. US4,368,144, 1983.
(242) Sadakane, M.; Horiuchi, T.; Kato, N.; Takahashi, C.; Ueda, W. Facile Preparation of Three-Dimensionally Ordered Macroporous Alumina, Iron Oxide, Chromium Oxide, Manganese Oxide, and Their Mixed-Metal Oxides with High Porosity. *Chem. Mater.* **2007**, *19* (23), 5779–5785.
(243) Pattison, J. N. Low Surface Area Alpha Alumina Catalyst Support for the Selective Hydrogenation of Hydrocarbons. US3068303, 1962.
(244) Li, J. G.; Sun, X. Synthesis and Sintering Behavior of a Nanocrystalline α-Alumina Powder. *Acta Mater.* **2000**, *48* (12), 3103–3112.
(245) Martín-Ruiz, M. M.; Pérez-Maqueda, L. A.; Cordero, T.; Balek, V.; Subrt, J.; Murafa, N.; Pascual-Cosp, J. High Surface Area α-Alumina Preparation by Using Urban Waste.

Ceram. Int. **2009**, *35* (6), 2111–2117.
(246) Furlan, K. P.; Pasquarelli, R. M.; Krekeler, T.; Ritter, M.; Zierold, R.; Nielsch, K.; Schneider, G. A.; Janssen, R. Highly Porous α-Al2O3 Ceramics Obtained by Sintering Atomic Layer Deposited Inverse Opals. *Ceram. Int.* **2017**, *43* (14), 11260–11264.
(247) Pérez, L. L.; Zarubina, V.; Heeres, H. J.; Melián-Cabrera, I. Condensation-Enhanced Self-Assembly as a Route to High Surface Area α-Aluminas. *Chem. Mater.* **2013**, *25* (20), 3971–3978.
(248) Sokolov, S.; Bell, D.; Stein, A. Preparation and Characterization of Macroporous α-Alumina. *J. Am. Ceram. Soc.* **2003**, *86* (9), 1481–1486.
(249) Schroden, R. C.; Al-daous, M.; Blanford, C. F.; Stein, A. Optical Properties of Inverse Opal Photonic Crystals. *Chem. Mater.* **2002**, *14*, 3305–3315.
(250) Zou, D.; Ma, S.; Guan, R.; Park, M.; Sun, L.; Aklonis, J. J.; Salovey, R. Model Filled Polymers. V. Synthesis of Crosslinked Monodisperse Polymethacrylate Beads. *J. Polym. Sci. Part A Polym. Chem.* **1992**, *30* (1), 137–144.
(251) Holland, B.; Blanford, C.; Stein, A. Synthesis of Macroporous Minerals with Highly Ordered Three-Dimensional Arrays of Spheroidal Voids. *Science (80-.).* **1998**, *281* (5376), 538–540.
(252) Scherrer, P. Bestimmung Der Inneren Struktur Und Der Größe von Kolloidteilchen Mittels Röntgenstrahlen. In *Kolloidchemie Ein Lehrbuch*; Springer Berlin Heidelberg: Berlin, Heidelberg, 1912; pp 387–409.
(253) Langford, J. I.; Wilson, A. J. C. Scherrer after Sixty Years: A Survey and Some New Results in the Determination of Crystallite Size. *J. Appl. Crystallogr.* **1978**, *11* (2), 102–113.
(254) Wefers, K.; Misra, C. *Oxides and Hydroxides of Aluminum*; Alcoa Technical Paper No 19, 1987.
(255) Mbese, J. Z.; Ajibade, P. A. Preparation and Characterization of ZnS, CdS and HgS/Poly(Methyl Methacrylate) Nanocomposites. *Polymers (Basel).* **2014**, *6* (9), 2332–2344.
(256) Han, D.; Li, X.; Zhang, L.; Wang, Y.; Yan, Z.; Liu, S. Hierarchically Ordered Meso/Macroporous γ-Alumina for Enhanced Hydrodesulfurization Performance. *Microporous Mesoporous Mater.* **2012**, *158*, 1–6.
(257) van Santen, R. A.; van Leeuwen, P. W. N. M.; Moulijn, J. A.; Averil, B. A. *Catalysis: An Integrated Approach*; Elsevier Science, 1999.
(258) Souza Santos, P.; Souza Santos, H.; Toledo, S. P. Standard Transition Aluminas. Electron Microscopy Studies. *Mater. Res.* **2000**, *3* (4), 104–114.
(259) Román, R.; Hernández, M. T.; Ibarra, A.; Vila, R.; Mollá, J.; Martín, P.; González, M. The Effect of Carbon Additives on the Dielectric Behaviour of Alumina Ceramics. *Acta Mater.* **2006**, *54* (10), 2777–2782.
(260) Besler, R.; Rossetti Da Silva, M.; Do Rosario, J. J.; Dosta, M.; Heinrich, S.; Janssen, R. Sintering Simulation of Periodic Macro Porous Alumina. *J. Am. Ceram. Soc.* **2015**, *98* (11), 3496–3502.
(261) Lange, F. F. Densification of Powder Compacts: An Unfinished Story. *J. Eur. Ceram. Soc.* **2008**, *28* (7), 1509–1516.
(262) Palmer, J. E.; Thompson, C. V.; Smith, H. I. Grain Growth and Grain Size Distributions in Thin Germanium Films. *J. Appl. Phys.* **1987**, *62* (6), 2492–2497.
(263) Assaker, K.; Carteret, C.; Durand, P.; Aranda, L.; St??b??, M. J.; Blin, J. L. Hydrothermal Stability of Ordered Surfactant-Templated Titania. *J. Phys. Chem. C* **2013**, *117* (32),

16500–16508.
(264) Blanford, C. F.; Schroden, R. C.; Al-Daous, M.; Stein, A. Tuning Solvent-Dependent Color Changes of Three-Dimensionally Ordered Macroporous (3DOM) Materials Through Compositional and Geometric Modifications. *Adv. Mater.* **2001**, *13* (1), 26–29.
(265) Zouboulis, E. S.; Grimsditch, M. Refractive Index and Elastic Properties of Single-crystal Corundum (A-Al2O3) up to 2100 K. *J. Appl. Phys.* **1991**, *70* (2), 772–776.
(266) Zhang, R.; Elzatahry, A. a.; Al-Deyab, S. S.; Zhao, D. Mesoporous Titania: From Synthesis to Application. *Nano Today* **2012**, *7* (4), 344–366.
(267) Deshpande, A. S.; Shchukin, D. G.; Ustinovich, E.; Antonietti, M.; Caruso, R. a. Titania and Mixed Titania/Aluminum, Gallium, or Indium Oxide Spheres: Sol-Gel/Template Synthesis and Photocatalytic Properties. *Adv. Funct. Mater.* **2005**, *15* (2), 239–245.
(268) Erekson, E. J.; Bartholomrw, C. H. Sulfur Poisoning of Nickel Methanation Catalysts. *Appl. Catal.* **1983**, *5* (3), 323–336.
(269) Kern, C.; Jess, A. Regeneration of Coked Catalysts - Modelling and Verification of Coke Burn-off in Single Particles and Fixed Bed Reactors. *Chem. Eng. Sci.* **2005**, *60* (15), 4249–4264.
(270) Meisenheimer, R. G. A Mechanism for the Deactivation of Trace Catalysts Metal Contaminants on Cracking. *J. Catal.* **1962**, *1*, 356–362.
(271) Shen, W. M.; Dumesic, J. A.; Hill, C. G. Criteria for Stable Ni Particle Size under Methanation Reaction Conditions: Nickel Transport and Particle Size Growth via Nickel Carbonyl. *J. Catal.* **1981**, *68* (1), 152–165.
(272) Soler-Illia, G. J. D. a a; Sanchez, C.; Lebeau, B.; Patarin, J. Chemical Strategies to Design Textured Materials: From Microporous and Mesoporous Oxides to Nanonetworks and Hierarchical Structures. *Chem. Rev.* **2002**, *102* (11), 4093–4138.
(273) Boskovic, G.; Dropka, N.; Wolf, D.; Brückner, A.; Baerns, M. Deactivation Kinetics of Ag/Al2O3 Catalyst for Ethylene Epoxidation. *J. Catal.* **2004**, *226* (2), 334–342.
(274) Bernardini, O. O.; Cherniak, E. A. Heterogeneous Isomerization of Ethylene Oxide to Acetaldehyde. *Can. J. Chem.* **1972**, *51*, 1371–1377.
(275) Hui-Xing, Y.; Hua, C.; De-Gang, H. The Rate Constant Determination for The Isomerization of Ethylene Oxide to Acetaldehyde by Chemical Shock Tube. *Acta Chim. Sin.* **1989**, No. 47, 941–946.
(276) Monnier, J. R.; Stavinoha, J. L.; Minga, R. L. Stability and Distribution of Cesium in Cs-Promoted Silver Catalysts Used for Butadiene Epoxidation. *J. Catal.* **2004**, *226* (2), 401–409.
(277) Van Hoof, A. J. F.; Filot, I. A. W.; Friedrich, H.; Hensen, E. J. M. Reversible Restructuring of Silver Particles during Ethylene Epoxidation. *ACS Catal.* **2018**, *8*, 11794–11800.
(278) Petit, P.; Salem, D.; He, M.; Paillet, M.; Parret, R.; Sauvajol, J.-L.; Zahab, A. Study of the Thermal Stability of Supported Catalytic Nanoparticles for the Growth of Single-Walled Carbon Nanotubes with Narrow Diameter Distribution by Chemical Vapor Deposition of Methane. *J. Phys. Chem. C* **2012**, *116* (45), 24123–24129.
(279) Datye, A. K.; Xu, Q.; Kharas, K. C.; Mccarty, J. M. Particle Size Distributions in Heterogeneous Catalysts : What Do They Tell Us about the Sintering Mechanism ? **2006**, *111*, 59–67.
(280) Zhou, X. G.; Yuan, W. K. Modeling Silver Catalyst Sintering and Epoxidation Selectivity Evolution in Ethylene Oxidation. *Chem. Eng. Sci.* **2004**, *59* (8–9), 1723–1731.

(281) Wynblatt, P.; Gjostein, N. A. Supported Metal Crystallites. *Prog. Solid State Chem.* **1975**, *9* (C), 21–58.
(282) Harris, P. J. F. Growth and Structure of Supported Metal Catalyst Particles. *Int. Mater. Rev.* **1995**, *40* (3), 97–115.
(283) Prieto, G.; Zečević, J.; Friedrich, H.; de Jong, K. P.; de Jongh, P. E. Towards Stable Catalysts by Controlling Collective Properties of Supported Metal Nanoparticles. *Nat. Mater.* **2012**, *12* (1), 34–39.
(284) Hansen, T. W.; DeLaRiva, A. T.; Challa, S. R.; Datye, A. K. Sintering of Catalytic Nanoparticles: Particle Migration or Ostwald Ripening? *Acc. Chem. Res.* **2013**, *46* (8), 1720–1730.
(285) Pompe, C. E.; van Uunen, D. L.; van der Wal, L. I.; van der Hoeven, J. E. S.; de Jong, K. P.; de Jongh, P. E. Stability of Mesocellular Foam Supported Copper Catalysts for Methanol Synthesis. *Catal. Today* **2019**, No. July 2018, 1–11.
(286) Li, T.; Zhou, W.; Wang, J.; Qu, Y.; Tian, C.; Pan, K.; Tian, G.; Fu, H. Confinement Effect on Ag Clusters in the Channels of Well-Ordered Mesoporous TiO 2 and Their Enhanced Photocatalytic Performance. *ChemCatChem* **2013**, *5* (6), 1354–1358.
(287) Chen, T.; Lei, Y.; Yang, Q.; Wu, Y. Stable and Accessible Metal Catalysts Confined by Mesoporous Carbon Structures Derived from Multicomponent Colloidal Spheres. *J. Mater. Chem. A* **2017**, *5* (7), 3136–3139.
(288) López, F.; Mascareñas, J. L.; Sousa-Castillo, A.; Correa-Duarte, M. A.; Destito, P.; Couceiro, J. R. Hollow Nanoreactors for Pd-Catalyzed Suzuki–Miyaura Coupling and O -Propargyl Cleavage Reactions in Bio-Relevant Aqueous Media . *Chem. Sci.* **2018**, 2598–2603.
(289) Lifshitz, I. M.; Slyozov, V. V. The Kinetics of Precipitation from Supersaturated Solid Solutions. *J. Phys. Chem. Solids* **1961**, *19* (1–2), 35–50.
(290) Marqusee, J. A.; Ross, J. Theory of Ostwald Ripening: Competitive Growth and Its Dependence on Volume Fraction. *J. Chem. Phys.* **1984**, *80* (1), 536–543.
(291) Van Den Berg, R.; Parmentier, T. E.; Elkjær, C. F.; Gommes, C. J.; Sehested, J.; Helveg, S.; De Jongh, P. E.; De Jong, K. P. Support Functionalization To Retard Ostwald Ripening in Copper Methanol Synthesis Catalysts. *ACS Catal.* **2015**, *5* (7), 4439–4448.
(292) Masoud, N.; Delannoy, L.; Schaink, H.; van der Eerden, A.; de Rijk, J. W.; Silva, T. A. G.; Banerjee, D.; Meeldijk, J. D.; de Jong, K. P.; Louis, C.; et al. Superior Stability of Au/SiO 2 Compared to Au/TiO 2 Catalysts for the Selective Hydrogenation of Butadiene. *ACS Catal.* **2017**, *7* (9), 5594–5603.
(293) Masoud, N. Thermal Stability of Oxide-Supported Au Nanoparticles. In *The Stability of Supported Gold Catalysts*; pp 65–77.
(294) Gong, J.; Ma, H.; Li, D.; Zeng, L.; Wang, X.; Li, X.; Assabumrungrat, S. Ceria-Promoted Ni/SBA-15 Catalysts for Ethanol Steam Reforming with Enhanced Activity and Resistance to Deactivation. *Appl. Catal. B Environ.* **2015**, *176–177*, 532–541.
(295) Bartholomew, C. H. Sintering Kinetics of Supported Metals: New Perspectives from a Unifying GPLE Treatment. *Appl. Catal. A, Gen.* **1993**, *107* (1), 1–57.
(296) Trimm, D. L. Thermal Stability of Catalyst Supports. In *Catalyst Deactivation*; 1991; pp 29–51.
(297) Meirer, F.; Kalirai, S.; Morris, D.; Soparawalla, S.; Liu, Y.; Mesu, G.; Andrews, J. C.; Weckhuysen, B. M. Life and Death of a Single Catalytic Cracking Particle. *Sci. Adv.* **2015**, *1* (3), e1400199.

(298) Hoof, A. J. F. Van; Hermans, E. A. R.; Bavel, A. P. Van; Friedrich, H.; Hensen, E. J. M. Structure Sensitivity of Silver-Catalyzed Ethylene Epoxidation. **2019**.
(299) Yang, H.; Deng, J.; Liu, Y.; Xie, S.; Xu, P.; Dai, H. Pt/Co3O4/3DOM Al2O3: Highly Effective Catalysts for Toluene Combustion. *Chinese J. Catal.* **2016**, *37* (6), 934–946.
(300) Campbell, C. T. The Effect of Size-Dependent Nanoparticle Energetics on Catalyst Sintering. *Science (80-.).* **2002**, *298* (5594), 811–814.
(301) Flynn, P.; Wanke, S. E. Experimental Studies of Sintering of Supported Platinum Catalysts. *J. Catal.* **1975**, *37* (3), 432–448.
(302) Arnal, P. M.; Comotti, M.; Schüth, F. High-Temperature-Stable Catalysts by Hollow Sphere Encapsulation. *Angew. Chemie Int. Ed.* **2006**, *45* (48), 8224–8227.
(303) Cao, A.; Veser, G. Exceptional High-Temperature Stability through Distillation-like Self-Stabilization in Bimetallic Nanoparticles. *Nat. Mater.* **2010**, *9* (1), 75–81.
(304) Xiong, H.; Lin, S.; Goetze, J.; Pletcher, P.; Guo, H.; Kovarik, L.; Artyushkova, K.; Weckhuysen, B. M.; Datye, A. K. Thermally Stable and Regenerable Platinum-Tin Clusters for Propane Dehydrogenation Prepared by Atom Trapping on Ceria. *Angew. Chemie Int. Ed.* **2017**, *56* (31), 8986–8991.
(305) Ward, E. P. W.; Yates, T. J. V; Fernández, J.-J.; Vaughan, D. E. W.; Midgley, P. A. Three-Dimensional Nanoparticle Distribution and Local Curvature of Heterogeneous Catalysts Revealed by Electron Tomography. *J. Phys. Chem. C* **2007**, *111* (31), 11501–11505.
(306) van den Reijen, J. E.; Keijzer, P. H.; de Jongh, P. E. Pore Structure Stabilization during the Preparation of Single Phase Ordered Macroporous α-Alumina. *Materialia* **2018**, *4*, 423–430.
(307) Miranda, M. A. R.; Sasaki, J. M. The Limit of Application of the Scherrer Equation. *Acta Crystallogr. Sect. A Found. Adv.* **2018**, *74* (1), 54–65.
(308) Prashanth, P. A.; Raveendra, R. S.; Krishna, R. H.; Ananda, S.; Bhagya, N. P.; Nagabhushana, B. M.; Lingaraju, K.; Naika, H. R. Synthesis , Characterizations , Antibacterial and Photoluminescence Studies of Solution Combustion-Derived Alpha-Al2O3 Nanoparticles. *Integr. Med. Res.* **2015**, *3* (3), 345–351.
(309) Albrecht, W.; van der Hoeven, J. E. S.; Deng, T.-S.; de Jongh, P. E.; van Blaaderen, A. Fully Alloyed Metal Nanorods with Highly Tunable Properties. *Nanoscale* **2017**, *9* (8), 2845–2851.
(310) Duval Malinsky, M.; Kelly, K. L.; Schatz, G. C.; Van Duyne, R. P. Nanosphere Lithography: Effect of Substrate on the Localized Surface Plasmon Resonance Spectrum of Silver Nanoparticles. *J. Phys. Chem. B* **2001**, *105* (12), 2343–2350.
(311) Perry, D. L. No Title. In *Handbook of Inorganic Compounds*; 1995; p 354.
(312) Bukhtiyarov, V.; Prosvirin, I. XPS Study of the Size Effect in Ethene Epoxidation on Supported Silver Catalysts. *J.* … **1997**, *93* (13), 2323–2329.
(313) Linic, S.; Barteau, M. A. Formation of a Stable Surface Oxametallacycle That Produces Ethylene Oxide. *J. Am. Chem. Soc.* **2002**, *124* (2), 310–317.
(314) Phongpreecha, T.; Nicholas, J. D.; Bieler, T. R.; Qi, Y. Computational Design of Metal Oxides to Enhance the Wetting and Adhesion of Silver- Based Brazes on Yttria-Stabilized-Zirconia. *Acta Mater.* **2018**, *152*, 229–238.
(315) Hsi, C. S.; Chen, Y. R.; Hsiang, H. I. Diffusivity of Silver Ions in the Low Temperature Co-Fired Ceramic (LTCC) Substrates. *J. Mater. Sci.* **2011**, *46* (13), 4695–4700.
(316) Dolbak, A. E.; Ol, B. Z. Diffusion of Silver over Atomically Clean Silicon Surfaces.

2013, *116* (6), 952–956.
(317) Balout, H.; Tarrat, N.; Puibasset, J.; Ispas, S.; Bonafos, C.; Benoit, M.; Balout, H.; Tarrat, N.; Benoit, M. Density Functional Theory Study of the Spontaneous Formation of Covalent Bonds at the Silver-Silica Interface in Ag Nanoparticles Embedded in SiO 2 : Implications for Ag + Release. **2019**.
(318) Nason, T. C.; Yang, G. R.; Park, K. H.; Lu, T. M.; Nason, T. C.; Yang, G.; Park, K.; Lu, T. Study of Silver Diffusion into Si (111) and SiO2 at Moderate Temperatures Study of Silver Diffusion into Si (L11) and Si02 at Moderate Temperatures. **2014**, *1392* (111).
(319) Gava, P. Modeling the Catalyst Selectivity in the Ethylene Epoxidation Reaction A First Principles Study. **2007**, No. October, 124.
(320) Ye, R. P.; Lin, L.; Li, Q.; Zhou, Z.; Wang, T.; Russell, C. K.; Adidharma, H.; Xu, Z.; Yao, Y. G.; Fan, M. Recent Progress in Improving the Stability of Copper-Based Catalysts for Hydrogenation of Carbon-Oxygen Bonds. *Catal. Sci. Technol.* **2018**, *8* (14), 3428–3449.
(321) Pompe, C. E.; Slagter, M.; de Jongh, P. E.; de Jong, K. P. Impact of Heterogeneities in Silica-Supported Copper Catalysts on Their Stability for Methanol Synthesis. *J. Catal.* **2018**, *365*, 1–9.
(322) Twigg, G. H. The Mechanism of the Catalytic Oxidation of Ethylene. I. Experiments Using a Flow System. *Proc. R. Soc. A Math. Phys. Eng. Sci.* **1946**, *188* (1012), 92–104.
(323) Bulushev, D. A.; Paukshtis, E. A.; Nogin, Y. N.; Bal, S. Transient Response and Infrared Studies of Ethylene Oxide Reactions on Silver Catalysts and Supports. **1995**, *123*, 301–322.
(324) Yong, Y.; Kennedy, E. M.; Cant, N. W. Oxide Catalysed Reactions of Ethylene Oxide under Conditions Relevant to Ethylene Epoxidation over Supported Silver. **1999**, *76* (1991), 31–48.
(325) Wang, J.; Ellis, P. D. Cesium-Induced Structural Change of Adsorbed Ethylene on Cesium-Promoted Silver Catalyst Studied By13C Solid-State Nuclear Magnetic Resonance. *J. Am. Chem. Soc.* **1991**, *113* (25), 9675–9676.
(326) Linic, S.; Barteau, M. A. On the Mechanism of Cs Promotion in Ethylene Epoxidation on Ag. *J. Am. Chem. Soc.* **2004**, *126* (26), 8086–8087.
(327) Carter, R. M. Process for the Preparation of Ethylene Oxide. US2294383, 1946.
(328) Dettwiler, H. R.; Baiker, A.; Richarz, W. Kinetics of Ethylene Oxidation on a Supported Silver Catalyst. *Helv. Chim. Acta* **1979**, *62* (6), 1689–1700.
(329) Kim, Y. C.; Park, N. C.; Shin, J. S.; Lee, S. R.; Lee, Y. J.; Moon, D. J. Partial Oxidation of Ethylene to Ethylene Oxide over Nanosized Ag/α-Al2O3 Catalysts. *Catal. Today* **2003**, *87* (1–4), 153–162.
(330) Al-Juaied, M. A.; Lafarga, D.; Varma, A. Ethylene Epoxidation in a Catalytic Packed-Bed Membrane Reactor: Experiments and Model. *Chem. Eng. Sci.* **2001**, *56* (2), 395–402.
(331) Lafarga, D.; Al-juaied, M. A.; Bondy, C. M.; Varma, A. Ethylene Epoxidation on Ag-Cs / α-Al2O3 Catalyst : Experimental Results and Strategy for Kinetic Parameter Determination. *Ind. Eng. Chem. Res.* **2000**, *39*, 2148–2156.
(332) Kenson, R. E.; Lapkin, M. Kinetics and Mechanism of Ethylene Oxidation. Reactions of Ethylene and Ethylene Oxide on a Silver Catalyst. *J. Phys. Chem.* **1970**, *74* (7), 1493–1502.
(333) Campbell, C. T.; Paffett, M. T. Model Studies of Ethylene Epoxidation Catalyzed by the Ag(110) Surface. *Surf. Sci.* **1984**, *139* (2–3), 396–416.
(334) Metcalf, P. L.; Harriott, P. Kinetics of Silver-Catalyzed Ethylene Oxidation. *Ind. Eng.*

Chem. Process Des. Dev. **1972**, *11* (4), 478–484.
(335) Grillo, M. E.; Coll, D. S.; Rodríguez, J. Effect of the Environment on the Hydroxyl Density of α-Quartz (111). *Chem. Phys. Lett.* **2012**, *522*, 46–50.
(336) Pimblott, S. M.; Green, N. J. B. Recent Advances in the Kinetics of Radiolytic Processes. In *Research in Chemical Kinetics*; 1993; pp 117–119.
(337) Rodrigues, F. A.; Monteiro, P. J. M.; Sposito, G. Alkali-Silica Reaction the Surface Charge Density of Silica and Its Effect on Expansive Pressure. *Cem. Concr. Res.* **1999**, *29* (4), 527–530.
(338) Valencia, E.; Maldonado, A. Adsorption of Isobutene on Partially Hydrophobized Aerosil. **1990**, *86* (3), 539–543.
(339) Warren, J.; Offenberger, S.; Toghiani, H.; Pittman, C. U.; Lacy, T. E.; Kundu, S. Effect of Temperature on the Shear-Thickening Behavior of Fumed Silica Suspensions. *ACS Appl. Mater. Interfaces* **2015**, *7* (33), 18650–18661.
(340) Berendsen, G. E.; De Galan, L. A Geometrical Model for Chemically Bonded Tms and Pds Phases. *J. Liq. Chromatogr.* **1978**, *1* (4), 403–426.
(341) Borman, P.; Westerterp, K. An Experimental Study of the Kinetics of the Selective Oxidation of Ethene over a Silver on Alpha-Alumina Catalyst. *Ind. Eng. Chem. Res.* **1995**, *34* (1), 49–58.
(342) Palys, M. J.; Ivanov, S. Y.; Ray, A. K. Conceptual Approach in Multi-Objective Optimization of Packed Bed Membrane Reactor for Ethylene Epoxidation Using Real-Coded Non-Dominating Sorting Genetic Algorithm NSGA-II. *Int. J. Chem. React. Eng.* **2017**, *15* (1), aop.
(343) Chongterdtoonskul, A.; Schwank, J. W.; Chavadej, S. Effects of Oxide Supports on Ethylene Epoxidation Activity over Ag-Based Catalysts. *J. Mol. Catal. A Chem.* **2012**, *358*, 58–66.
(344) Chongterdtoonskul, A.; Suttikul, T.; Santikunaporn, M.; Schwank, J. W.; Chavadej, S. Effect of Diluent Gas on Ethylene Epoxidation Activity over Various Ag-Based Catalysts on Selective Oxide Supports. *J. Mol. Catal. A Chem.* **2014**, *386*, 5–13.
(345) van den Reijen, J. E.; Versluis, W. C.; Kanungo, S.; Angelo, M. F.; de Jong, K. P.; de Jongh, P. E. From Qualitative to Quantitative Understanding of Support e Ff Ects on the Selectivity in Silver Catalyzed Ethylene Epoxidation. *Catal. Today* **2019**, *338* (April), 31–39.

6

Summary and Perspectives

Summary
Since the discovery of the silver catalysed direct epoxidation of ethylene, this technology has been applied for over 100 years and extensive research has been performed, improving the process significantly, increasing yields of the industrial heterogeneous catalytic process. The process is applied on a million-ton per annum scale. The typical catalyst is silver supported on α-alumina.

Due to the large scale on which the epoxidation process is applied, small improvements in the performance of the catalyst can potentially lead to large gains in returns. The primary focus for improvements of these catalysts has been focused on increasing the selectivity towards ethylene oxide. Increasing the activity of the catalysts is less important due to the trade-off of the selectivity with increasing conversion. The stability of the catalyst is another important parameter.

This thesis is focused on the preparation and catalytic performance of supported silver catalysts. The catalytic performance of supported silver catalysts decreases with 'time-on-stream'. This decrease in performance is attributed to the increase of the average silver particle size. Increasing the stability of the catalyst can be done by adding promoters and increasing the specific surface area of the support material.

Silver is the active metal in the catalyst and signifies the main costs for the preparation of the supported catalyst, since the concentration of promoters is significantly lower and the support material is relatively cheap. Increasing the complexity and therefore the costs of the support is consequently not detrimental to the overall costs of the catalyst and overall process. Optimizing the performance of the catalyst by designing the support material for high selectivity, activity and stability proves an interesting approach.

When the particle size of silver particles on different support types can be controlled, the effect of particle size can be separated from the effect of the support. In **chapter 2** we discuss the preparation of silver catalysts supported on industrially relevant α-alumina. By varying the gas atmosphere during the decomposition of the silver precursor by heat treatment, the average silver particle size can be tuned to a desired particle size. The catalysts prepared using this method have a weight loading of 15 wt% silver with particle sizes ranging from 20 to 500 nm supported on 8 m^2/g α-alumina. Using this method, the particle size can be tailored independently of the support specific surface area or the weight loading of the active metal. Because only the particle size is variable, the particle size effect under relevant catalytic conditions was explored.

The activity followed a particle size dependent trend where small silver particles exhibit low activities, which increased with increasing particle size up to 50 – 60 nm. From this size on, the activity correlates with the amount of exposed silver available for the reaction. However, we also showed that the selectivity towards ethylene oxide was independent of the particle size. This implies that the particle size effect in the activity, does not correspond to different active sites on small and large particles, but probably to the absence of active sites on smaller particles.

In **chapter 3** the synthesis of an ordered macroporous or 3DOM α-alumina support is discussed. These foam-like structures with pore sizes of circa 200 nm are ideal for facilitating the large

particles required for active ethylene epoxidation catalysts. These materials were obtained by a hard templating method using a polymeric template which is impregnated with an aluminium precursor, which is converted to aluminium hydroxide within the pores of the polymeric template. By increasing the amount of aluminium hydroxide in the pores of the template, a higher yield is obtained and the pore structure of the resulting macroporous material is better maintained. By applying a two-step heat treatment, one in inert atmosphere and one in oxidizing atmosphere, the ordered morphology is even better maintained. In the first heat treatment, the template is pyrolyzed to a carbon film which stabilizes the porous structure at high temperature, which wouldn't be present when a single heat treatment is air was applied. After heat treatment in inert atmosphere, the carbon layer is maintained even at high temperatures, capable of stabilizing the pore structure and even preventing the formation of α-alumina. A second heat treatment in air is required to remove the carbon layer and form the desired α-alumina. The resulting 3DOM α-alumina has maintained the structure imposed by the hard template better than 3DOM α-alumina produced via a single heat treatment step.

The thermal stability of silver supported on ordered macroporous α-alumina was investigated in **chapter 4**. The average silver particle size of α-alumina supported silver increases relatively easily in oxidizing atmosphere, while the particles are quite stable in reducing atmosphere during thermal stability tests. The rate of sintering is less on higher surface area supports, due to a more effective separation of the silver particles. On the high surface area, ordered macroporous support, the silver particles are even less prone to sintering, when the silver particles are larger than the pore windows of the foam-like morphology of the support. The catalytic stability of silver particles during ethylene epoxidation is increased when the particles are supported on the high surface area material, compared to silver particles supported on low surface area α-alumina.

While high support specific surface areas are beneficial for the stability of support particles, the specific surface area of the support material in industrial ethylene epoxidation catalysts is typically very low (<5 m^2/g) to prevent side reactions which are co-catalysed by the support material. This is believed to be due to the isomerization of the desired product, ethylene oxide, to acetaldehyde. In **chapter 5** the detrimental role of the support material on the selectivity towards ethylene oxide was shown. Silver supported on α-alumina and fumed silica supports with different specific surface areas were tested in the ethylene epoxidation reaction. Due to similar silver particle sizes and active metal weight loadings, the intrinsic selectivity over the silver particles is constant. Difference in the selectivity are therefore attributed to secondary reaction occurring over the support surface. The decay of selectivity with increasing conversion was fitted with an exponential decay from a first order rate in ethylene oxide. The resulting rate constant was shown to be linearly dependent on the specific surface area of the support, and the isomerization of ethylene oxide was therefore first order in ethylene oxide and first order in the support surface species. The selectivity is therefore highly dependent on the total amount of surface hydroxyl species as this can vary significantly between different support materials.

Perspectives

By optimizing the average particle size and narrowing the particle size distribution of the silver particle size, the performance of these types of catalysts can be improved, while also reducing the costs of catalyst production. While this holds true for silver catalysed ethylene epoxidation, it is generally applicable for all supported catalysts. The preparation method for supported silver catalysts discussed in this thesis can be extended to other metals and supports.

Within the field of ethylene epoxidation the methods described in this thesis can be applied to achieve catalysts supported on high surface area α-alumina, but with a ratio of silver surface to support surface similar to the low surface area α-alumina supported catalysts. The expected selectivities for such catalysts are similar to their low support surface area counterparts, but with a higher activity per gram of catalyst due to higher weight loading. Due to the support morphology of the high surface area ordered macroporous support, an additional stabilizing effect can be expected.

In this thesis, the nature of the hydroxyl species was not discussed extensively, while these are shown to be influential on the selectivity to ethylene oxide in the epoxidation reaction. These contributions are an interesting subject of further investigation as their reactivity plays a significant role in the overall selectivity observed in the epoxidation reaction. A potential route could be by modifying a carbon support to either introduce or remove surface hydroxyl species without significantly changing the specific surface area of the support.

Combining the methods described in chapter 2, 3 and 5 could lead to active and selective catalysts, which are potentially interesting for industrial applications. However, these catalysts should then be tested in the presence of relevant promotors and under elevated pressure in order to make a fair comparison.

Ordered macroporous alumina provides a relatively high surface area support capable of stabilizing large metal particles against sintering under catalytic reaction conditions. While the increased specific surface area of these support materials can be detrimental to the selectivity of the resulting catalyst, such as is the case in the epoxidation reaction, these high surface area, macroporous α-alumina support materials can be applied in the production other α-alumina supported reactions. Furthermore, other metal oxide three dimensionally ordered macroporous (3DOM) materials can be produced using the same or a similar procedure, widening the field of applications even further. Outside of the field of catalysis these 3DOM materials can prove interesting due to their optical properties, which is highly dependent on the ordering of the structure.

6

Nederlandse samenvatting

Katalyse is voor de meeste mensen een tamelijk onbekend begrip, terwijl het van groot belang is voor het moderne leven. Bijna alle producten waar men vandaag de dag mee in aanraking komt, zijn in meer of mindere mate mogelijk gemaakt door middel van katalyse. Zo wordt er in de petrochemie veel gebruik gemaakt van katalysatoren om ongewenste of minder waardevolle fracties verkregen uit ruwe aardolie om te zetten naar waardevollere producten. Denk hierbij aan zware oliefracties, die kunnen worden omgezet naar brandstoffen of grondstoffen voor de kunstofindustrie. Bij het produceren van de polymeren die uiteindelijk omgezet worden in plastics, wordt ook vaak gebruik gemaakt van een katalysator. De vereiste chemische reacties zijn in afwezigheid van een katalysator moeilijk te controleren waardoor het eindproduct niet aan de gestelde kwaliteitseisen voldoet. Een katalysator is bijvoorbeeld vereist om een stevige autobumper van polypropeen te maken. Daarnaast worden katalysatoren ingezet om afvalstromen, zoals bijvoorbeeld uitlaatgassen van auto's of spoelwater uit de textielindustrie, op te schonen zodat ze veilig terug de omgeving ingevoerd kunnen worden.

Hoewel katalysatoren voor verscheidene toegepasingen wordt gebruikt, en sterk kunnen variëren in hun vorm en voorkomen, is de werking van katalysatoren in veel gevallen gelijk: twee chemicaliën die normaal niet of nauwelijks met elkaar reageren, doen dat wel in het bijzijn van een katalysator. Dit kan komen doordat de kans op een toevallige botsing in de gasfase zeer klein is, terwijl beiden wel adsorberen op het oppervlak van een katalysator, waar de onderlinge afstand veel kleiner is. Het kan ook zijn dat het gewenste product alleen gevormd wordt wanneer deze botsing plaats vindt onder bepaalde bijzondere omstandigheden. Zo kan een katalysator electronen doneren of juist onttrekken aan het reactant molecuul of het molecuul in een bepaalde configuratie brengen. Hierdoor zijn andere delen van het reactant reactief en/of benaderbaar waardoor er mogelijk andere producten gevormd worden dan wanneer dezelfde reactie in een gas- of vloeistoffase had plaats gevonden.

Over het algemeen kunnen katalysatoren worden opgedeeld in drie verschillende categoriën: heterogene, homogene en biokatalysatoren. Een typische katalysator in deze laatste categorie is bijvoorbeeld gist voor het rijzen van brood of het fermenteren van suikers tijdens het brouwen van bier. In dit geval heeft de mens slim gebruik gemaakt van de natuurlijke eigenschap van een schimmel die in staat is suiker te verwerken en daarbij CO_2 en ethanol produceren. In industriële biokatalytische processen is de katalysator altijd een enzym, soms toegepast in zijn opgezuiverde, gedroogde vorm, soms als gehele cel in een waterige omgeving.

Homogene katalyse is het resultaat van de pogingen van de mens om de biokatalyse te benaderen. In beiden gevallen bestaat de katalysator uit een actieve kern, vaak een metaalatoom, gestabiliseerd door organische groepen. Deze organische groepen, vaak liganden genoemd, stabiliseren het actieve centrum en creëren een beperkte ruimte waarin het reactant het actieve centrum kan benaderen. De liganden in homogene katalysatoren zijn minder ingewikkeld dan in een enzym en de functionaliteit is daardoor relatief makkelijk aan te passen aan een specifieke reactie, hoewel de activiteit en selectiviteit over het algemeen niet zo goed zijn als bij de door de natuur gevormde katalysatoren.

Een belangrijk gegeven voor homogene katalyse is dat de katalysator en de reactanten zich in dezelfde fase bevinden; beide zijn meestal opgelost in een vloeistof. Hierdoor is de kans dat

deze in contact komen groot, wat de algehele activiteit van de katalysator bevordert. Dit is ook meteen het belangrijkste onderscheid met heterogene katalysatoren: heterogene katalysatoren bevinden zich in een andere fase dan de reactanten en producten. In de meeste gevallen is de katalysator een vaste stof, terwijl de reactanten gassen en/of vloeistoffen zijn. Het voordeel hiervan is dat de katalysator gemakkelijk gescheiden kan worden van het reactiemengsel en kan worden hergebruikt. Daarnaast zijn heterogene katalysatoren robuuster dan homogene of biokatalysatoren, ze kunnen hierdoor toegepast worden in reacties waar hoge temperaturen en/of drukken vereist zijn.

Net als homogene en biokatalysatoren bestaat de actieve kern van heterogene katalystoren in de meeste gevallen uit een metaal. In dit geval kan het een metaalatoom zijn, maar ook een metaaloxide of metaalzout. Er zijn geen liganden om het actieve centrum te stabiliseren; de atomen zijn vaak geclusterd tot kleine deeltjes (nanodeeltjes) of zelfs tot een poeder. De reactiviteit van het actieve centrum kan niet worden aangepast door het uitwisselen van liganden, de directe omgeving van het actieve centrum bestaat uit een metaaloppervlak en de daarop geadsorbeerde componenten. Deze omgeving kan worden aangepast door bewust componenten aan dit oppervlak toe te voegen. Zo worden (aard)alkalimetaaloxides toegevoegd om de elektronische eigenschappen van de katalysator aan te passen door lading te ontrekken of toe te voegen aan het oppervlak, of kunnen er stoffen op het oppervlak geadsorbeerd worden om de toegang tot het oppervlak te bemoeilijken en zo de selectiviteit aan te passen.

Om de hoeveelheid beschikbaar oppervlak te vergroten hebben kleine deeltjes de voorkeur, maar deze klonteren samen (ook wel sintering genoemd) onder reactieomstandigheden en moeten daarom gestabiliseerd worden. Dit brengt extra kosten en soms ongewenste neveneffecten met zich mee. Als het actieve materiaal goedkoop is, wordt daarom soms gekozen dit materiaal te gebruiken als poreuze korrels. Wanneer de actieve fase duur is, kan ze worden gestabiliseerd door dragermaterialen, zoals metaaloxides of koolstof. Deze materialen zijn relatief goedkoop vergeleken met het actieve materiaal, minder gevoelig voor sintering en kunnen verkregen worden met een hoog specifiek oppervlak (veel vierkante meters per gram materiaal). Hierdoor kunnen de kleine metaaldeeltjes direct op het oppervlak worden gesynthetiseerd, en blijven ze effectief van elkaar gescheiden.

De katalysator die gebruikt wordt voor de productie van etheenoxide is bijzonder: de gemiddelde deeltjesgrootte van het actieve metaal is één à twee ordes groter dan de deeltjes die voor veel andere katalysatoren als optimaal worden gezien en daarbij zijn deze deeltjes aangebracht op een materiaal met laag specifiek oppervlak (α-alumina).

Etheenoxide is een molecuul bestaande uit twee koolstofatomen, vier waterstofatomen en een zuurstofatoom, waarbij de twee koolstofatomen en het zuurstofatoom een driehoek vormen, en dat gebruikt wordt voor de productie van antivries en plastics. Het is een erg reactief molecuul dat verkregen wordt door etheen deels te oxideren, waarbij het risico van verbranding, ofwel volledige oxidatie, groot is. Zilver blijkt een van de weinige metalen te zijn die deze reactie selectief kan katalyseren, maar relatief grote zilverdeeltjes zijn nodig; kleine nanodeeltjes zijn niet actief. De opbrengst van etheenoxide wordt verminderd door de aanwezigheid van een dragermateriaal. Deze materialen hebben groepen op hun oppervlak die in de meeste reactieomstandigheden inert zijn, maar die wel actief genoeg zijn om de gespannen ring van etheenoxide te openen. Een materiaal als α-alumina heeft weinig van dit soort groepen, en om die reden wordt etheenoxide al

meer dan zestig jaar gemaakt met behulp van een zilver op α-alumina katalysator.

De focus van dit proefschrift ligt op de bereiding en het testen van dit soort katalysatoren. In hoofdstuk 2 wordt een methode omschreven om de deeltjesgrootte van zilver te variëren door de gasatmosfeer aan te passen waar de voorloper van de katalysator aan wordt blootgesteld tijdens de bereiding. Met deze methode is het mogelijk zilverdeeltjes van 20 tot 500 nm te verkrijgen, terwijl het specifiek oppervlak en de zilvergewichtsbelading constant wordt gehouden. Met de verkregen katalysatoren is het effect van de verschillende zilverdeeltjesgroottes onderzocht, waarbij kleinere deeltjes minder actief waren, ondanks dat deze deeltjes een hoger zilver oppervlak per gram hebben. Verrassend genoeg bleek de selectiviteit niet afhankelijk te zijn van de deeltjesgrootte.

In hoofdstuk 3 wordt de bereiding van een sponsachtig α-alumina besproken. De zogenoemde 3DOM structuur van dit materiaal bevat poriën die groot genoeg zijn om de zilverdeeltjes te bevatten en waardoor het materiaal een groot specifiek oppervlak heeft. Hierdoor kan de katalysator een hogere gewichtsbelading bevatten bij een gelijke oppervlakte belading (meer zilver per gram bij gelijke hoeveelheid zilver per vierkante meter). Dit 3DOM drager materiaal werd bereid door een hard templating methode. Deze methode kan vergeleken worden met een verlorenwasmethode, zoals gebruikt wordt om mallen voor het gieten van bijvoorbeeld brons: In ons geval bestaat een mal uit precies gestapelde polymeren bollen. In de holtes tussen deze bollen wordt aluminumhydroxide afgezet, wat wordt gedroogd en uitgehard tot α-alumina terwijl het polymeer wordt weggebrand. Door de bestaande procedure voor deze methode aan te passen werd een hogere opbrengst en een materiaal van hogere kwaliteit verkregen. Dit werd bereikt door meer materiaal af te zetten in de holtes tussen de polymeerbollen en door het uitharden van de alumina precursor en het verwijderen van het polymeer in twee verschillende stappen uit te voeren.

De thermische stabiliteit van de zilverdeeltjes op verschillende soorten α-alumina wordt besproken in hoofdstuk 4. Hierbij is ook gekeken naar het effect van de gasatmosfeer, waarbij de zilverdeeltjes beter bestand bleken tegen sinteren in een reducerende atmosfeer; in oxiderende atmosfeer groeiden de deeltjes veel sneller. Daarnaast bleek ook het gebruik van dragers met een hoger specifiek oppervlak de deeltjesgroei te verminderen, doordat de deeltjes een grotere onderlinge afstand hebben op dit soort materialen. Het gebruik van het poreuze materiaal uit hoofdstuk 3 zorgt voor een verdere stabilisatie doordat de kooistructuur de deeltjes gevangen houdt.

Hoewel het verhogen van het oppervlak van de drager een positief effect heeft op de stabiliteit van de katalysator, werkt dit zoals gezegd negatief in op de selectiviteit in de oxidatie reactie. De oppervlaktegroepen van het dragermateriaal zijn actief genoeg om de reactieve etheenoxidering te openen, wat leidt tot het isomeer acetaldehyde. Dit molecuul is tamelijk onstabiel onder de reactieomstandigheden, waardoor het snel volledig verbrandt. In hoofdstuk 5 kijken we naar hoe de drager de selectiviteit beïnvloedt, door zilverdeeltjes met soortgelijke deeltjesgrootte af te zetten op verschillende dragers met sterk verschillend specifiek drageroppervlak. Hierbij wordt naast α-alumina ook silica bestudeerd; dit materiaal kan gemakkelijk verkregen worden met hoge oppervlaktes. Zowel het type drager (silica of alumina) als het specifieke oppervlak blijkt invloed te hebben op de selectiviteit naar etheenoxide. Hierbij neemt de isomerisatiesnelheid lineair toe met het aantal oppervlaktegroepen wat leidt tot een lagere opbrengst van etheenoxide. Dit geeft nieuw inzicht in het mechanisme van etheenepoxidatie.

6

List of publications and presentations

Publications

J.E. van den Reijen, W.C. Versluis, S. Kanungo, M.F. d'Angelo, K.P. de Jong, P.E. de Jongh, From qualitative to quantitative understanding of support effects on the selectivity in silver catalyzed ethylene epoxidation, Catalysis Today, 2019, 10.1016/j.cattod.2019.04.049

J.E. van den Reijen, P.H. Keijzer, P.E. de Jongh, Pore structure stabilization during the preparation of single phase ordered macroporous α-alumina, Materialia, 2018, 423-430, 10.1016/j.mtla.2018.10.016

J.E. van den Reijen, S. Kanungo, T.A.J. Welling, M. Versluijs-Helder, T.A. Nijhuis, K.P. de Jong, P.E. de Jongh, Preparation and particle size effects of $Ag/\alpha\text{-}Al_2O_3$ catalysts for ethylene epoxidation, Journal of Catalysis, 2017, 65-74, 10.1016/j.jcat.2017.10.001

Other publications

J.E.S. van der Hoeven, T.A.J. Welling, T.A.G. Silva, J.E. van den Reijen, C. La Fontaine, X. Carrier, C. Louis, A. van Blaaderen, P.E. de Jongh, In Situ Observation of Atomic Redistribution in Alloying Gold-Silver Nanorods, ACS Nano, 10.1021/acsnano.8b03978

E. Plessers, J.E. van den Reijen, P.E. de Jongh, K.P. de Jong, M.B.J. Roeffaers, Origin and Abatement of Heterogeneity at the Support Granule Scale of Silver on Silica Catalysts, ChemCatChem, 2017, 4562-4569, 10.1002/cctc.201700753

Oral Presentations

J.E. van den Reijen, P.H. Keijzer, W.C. Versluis, S. Kanungo, M.F. Neira d'Angelo, K.P. de Jong, P.E. de Jongh, Support dependent selectivity in ethylene epoxidation catalysts, World Congress on Oxidation Catalysis, Krakau 2017

J.E. van den Reijen, P.H. Keijzer, W.C. Versluis, S. Kanungo, M.F. Neira d'Angelo, K.P. de Jong, P.E. de Jongh, Effect of Support on the Selectivity in the Ag-Catalyzed Oxidation of Ethylene, EuropaCat, Florence 2017

J.E. van den Reijen, P.K. Keijzer, Marjan Versluis, K.P. de Jong, P.E. de Jongh, What determines the selectivity in the Ag-catalyzed epoxidation of Ethylene?, 25th North American Catalysis Society meeting, Denver, 2017

J.E. van den Reijen, S. Kanungo, T.A. Nijhuis, K.P. de Jong, P.E. de Jongh, Particle size effects of $Ag/\alpha\text{-}Al_2O_3$ for ethylene epoxidation, International Congress on Catalysis, Beijing 2016

J.E. van den Reijen, S. Kanungo, T.A. Nijhuis, K.P. de Jong, P.E. de Jongh, Preparation of $Ag/\alpha\text{-}Al_2O_3$ catalysts; Particle size effect of $Ag/\alpha\text{-}Al_2O_3$ for ethylene epoxidation, ACS National Meeting, San Diego 2016

J.E. van den Reijen, P.H. Keijzer, W.C. Versluis, S. Kanungo, M.F. Neira d'Angelo, K.P. de Jong,

P.E. de Jongh, Support surface area dependent selectivity in ethylene epoxidation catalysts, CHAINS, Veldhoven 2016

J.E. van den Reijen, P.H. Keijzer, W.C. Versluis, S. Kanungo, M.F. Neira d'Angelo, K.P. de Jong, P.E. de Jongh, Effect of support specific surface area on the selectivity of silver catalysts in the epoxidation of ethylene, N3C, Noordwijkerhout 2016

Poster Presentations

J.E. van den Reijen, P.H. Keijzer, W.C. Versluis, S. Kanungo, M.F. Neira d'Angelo, K.P. de Jong, P.E. de Jongh, Effect of support specific surface area on the selectivity of silver in the epoxidation of ethylene, N3C, Noordwijkerhout 2017

J.E. van den Reijen, S. Kanungo, T.A. Nijhuis, K.P. de Jong, P.E. de Jongh, Particle size effects of $Ag/\alpha\text{-}Al_2O_3$ for ethylene epoxidation, N3C, Noordwijkerhout 2015

J.E. van den Reijen, K.P. de Jong, P.E. de Jongh, Controlling the silver particle size in $Ag/\alpha\text{-}Al_2O_3$ epoxidation catalysts, CHAINS, Veldhoven 2014

6

Dankwoord

Hoewel mijn naam op de kaft van dit boekje staat, was dit werk nooit afgekomen als ik alles alleen had moeten doen. Allereerst wil ik Petra de Jongh bedanken voor de gelegenheid om mijn onderzoek uit te voeren in haar groep. U stond altijd open voor overleg en u was zelfs tijdens de late avonduren of vakanties bereikbaar. Bedankt voor uw kritische houding, ik heb hier veel van geleerd en ik denk dat de kwaliteit van dit boekje vooral hieraan te danken is.

Toen ik werd aangenomen als promovendus binnen de groep, was dit officieel onder Krijn de Jong, die later mijn tweede promotor werd, maar altijd betrokken is gebleven bij het project. Doordat u een grote bron van kennis bent over mijn onderzoeksonderwerp, waren discussies met u altijd erg inzichtelijk en was er hierna altijd weer genoeg te doen.

Zonder de ondersteuning van het hart van een onderzoeksgroep komt er van onderzoek weinig, dus daarom ook dank naar het secretariaat en de technische staf. Dymph, Iris en Monique bedankt voor jullie hulp bij navigeren van de Utrechtse bureaucratie. Ad^{M}, bedankt voor de hulp wanneer er weer iemand iets kapot of kwijt heeft gemaakt. Ad^{E}, de kritische blik op de veiligheid op het lab, zonder u zou het lab een rotzooi worden en onze BHV groep niet zo goed zijn. Pascal, bedankt voor al jouw hulp met de GC's als ik weer eens een vrijdagmiddagexperiment wilde doen. Bovendien natuurlijk ook bedankt voor je hulp met de bestellingen. Je was altijd bereid nog even snel iets goed te keuren als ik weer eens iets te laat besteld had. Jan Willem en Rien bedankt voor jullie hulp bij de bouw van de epoxidatie setup. Zonder jullie hulp had ik veel minder katalytische data kunnen verzamelen en was dit een erg dun boekje geworden. Oscar, altijd gezellig aanwezig tijdens borrels en bereid om 'even snel' te helpen als er iets gemaakt moet worden, ook al ben je zelf veel te druk. Herrik, Fouad en Marjan bedankt voor de hulp met LabView, infrarood, XRD, TGA en SEM. Ramon, toen ik nog op de groep rond liep was jij officieel geen technician, maar desondanks gedroeg jij je wel zo: altijd behulpzaam en met kennis over praktisch alle apparatuur.

The collaboration with Shamayita Kanungo, Xander Nijhuis and Fernanda Neira d'Angelo was very pleasant and fruitful. Besides a lot of insight in the reaction and several papers, you, and rest of the SCR group in Eindhoven, really helped us with getting our own setup in Utrecht. This collaboration was instrumental for most of the work described in this thesis. De samenwerking met Eva Plessers en Maarten Roeffaers was ook zeer prettig: mooi om katalysatorbereiding eens op een andere schaal te bekijken en ik denk dat het tot een belangrijk inzicht heeft geleid. I was given the opportunity to help out Eric Marceau, Jean-Sebastien and Carmen with their work on the Soleil synchrotron. Even though we made some long days, we also had some good times watching movies and discussing the differences between France and the Netherlands. I also want to thank Juliette Blanchard for her hospitality and her time to teach me about the treatment of silica supports and a lot of other techniques I've used during my PhD.

Tijdens mijn tijd in Utrecht heb ik ook veel hulp gehad van studenten, die een aanzienlijk deel van het onderzoek gedaan hebben. Allereerst Corneel, hoewel de resultaten van jouw bacheloronderzoek niet direct in deze thesis terecht zijn gekomen, vormden ze wel een basis waarop ik een deel van het werk in hoofdstuk 4 heb gebaseerd. Caroline, de resultaten die we hebben verkregen uit jouw brede set katalysatoren waren in eerste instantie voor ons beiden verwarrend, maar uiteindelijk hebben deze geleid tot hoofstuk 5. Mathilde, you continued on the work of Petra Keijzer and provided interesting insight in the thermal deactivation of silver particles under a range of conditions. This added more insight in the stability of the particles on alumina supports, which helped us to finish this paper and chapter 4. Petra, tijdens jouw masteronderzoek ben je in staat geweest een uniek model support materiaal te maken. Jouw interesse in de synthese van

anorganische materialen maakte dat we een goed team vormden, wat denk ik tot mooie resultaten heeft geleid. Nu ben je zelf ondertussen al ver in je eigen promotieonderzoek en heb je het werk op het gebied van zilver overgenomen.

Ik wil ook mijn collega's in Petra's corner en omstreken bedanken. Dit was in al mijn jaren in ICC een gezellige hoek, hoewel er gedurende de jaren al aardig wat gerouleerd is. Although everybody in Petra's corner and the rest of ICC helped make my time in the group enjoyable, I especially need to thank Gang and Peter. We have gotten to know each other quite well, even so well that I can retell half of your stories. Ramon, bedankt dat je altijd in bent voor een speciaal bier(sessie) of een spontane borrel.

Luckily, my time in Utrecht wasn't just work, outside of office hours we often met to play pool or go bowling or basketball during the Debye Sports Days. Daarnaast ook fietsen met collega's om toch nog een beetje sportief te doen en gewoon te kletsen. Some of my colleagues were even brave enough to go on holiday with me. Trips to Istanbul, Madrid, Stavanger and Lisbon. There were even so many trips to go on that I had to skip a couple!

Bedankt aan de brouwers van Tok-Sik en iedereen die ooit mee gebrouwen heeft, bedankt voor het ondersteunen van mijn hobby en de gezellige middagen. Er staan nog genoeg restanten in het hok, dus voel je vrij om langs te komen voor een drankje of voor nog een brouwsessie.

Oude vrienden uit Eindhoven: vijf willekeurige personen, oud-bestuursgenoten van de Chemiewinkel en JAPIE, de Close(d) Harmony en ons kaartclubje, mooi dat we het contact in stand kunnen houden ondanks dat iedereen het drukker heeft. Iedereen van ut twedde van Agathos bedankt voor de afleiding. Wouter, Sjoerd, Davide en Francesco, het afronden van dit boekje gaat bijna even snel als het boeken van een vakantie met ons allen, maar prachtig dat we het toch steeds weer voor elkaar krijgen om elk jaar weer, met zijn allen, op tijd op de plaats van bestemming te komen. Laten we deze traditie nog jaren in ere houden.

Pa en ma bedankt voor jullie steun gedurende de jaren. Eindelijk lijkt het afgerond te zijn, bedankt voor jullie geduld, ook al draaf ik al jaren te ver door als ik over werk praat. Robin en Niels, ik ben blij met onze goede band en de gezellige tijd als we samen zijn. Jan en Mientje, bedankt dat jullie altijd klaar staan voor Kristel, mij en sinds kort onze kleine man.

Kristel, ik ben de afgelopen jaren niet de makkelijkste geweest en ben dat ook niet altijd als ik niet gestresst ben door het afronden van een thesis of werk, dus bedankt dat jij me altijd bent blijven steunen en motiveren. Bovendien ben je ook altijd in voor een biertje en/of een spelletje, en ik ben blij dat ik jou mijn vrouw mag noemen, dat jij mijn punt van rust en mijn steunpilaar bent als ik druk ben.

Owen, vent, mijn maat, hoewel je er pas net bent en weinig mee hebt gekregen van de tijd die ik aan dit boekje heb gespendeerd, toch heb jij zeker een rol gespeeld tijdens de afronding hiervan. Ondertussen ben jij al een flinke kerel geworden en ren jij al enthousiast rond. We laten nu alle stress achter ons en gaan een mooie tijd samen tegemoet.

6

Curriculum Vitae

Jeroen van den Reijen was born on 8 november 1987 in Raamsdonk, the Netherlands. After finishing high school at Dongemond College in Raamsdonksveer he started his bachelor studies in 2006 in Chemistry and Chemical Engineering at Eindhoven Technical University. Following a master focusing on Inorganic Chemistry and Catalysis within the Molecular Engineering master track with a thesis titled The effect of ruthenium particle size and capping agent on the methanation reaction. During his master studies he did an internship at Statoil ASA in Trondheim, Norway. In July 2013 he started his PhD research in the Inorganic Chemistry and Catalysis group under the supervision of prof. dr. Petra de Jongh and prof. dr. ir. Krijn de Jong. This project focused on supported silver catalysts for the epoxidation of ethylene. The most important results of this research are presented in this thesis. The work is conducted in collaboration with BSc and MSc students, colleagues from Utrecht University, Eindhoven University of Technology, Université Pierre et Marie Curie, Université Lille and KU Leuven. Jeroen continued his career as a Technology Development Engineer at Avantium.